Master's Thesis

Peg-In-Hole Task Using Impedance Control For T-Flex Demonstration

N.F.H. Jansen

Faculty Engineering Technology
Department Mechanics of Solids, Surfaces & Systems
Chair Precision Engineering

Examination Committee:

Dr. Ir. W.B.J. Hakvoort
Dr. J. Dasdemir
Dr. I.S.M. Khalil
Ir. B. Gerlagh

UNIVERSITY OF TWENTE.

Peg-In-Hole Task using Impedance Control for T-Flex Demonstration

Master's Thesis

Nathan Jansen

Presented on October 30, 2024

Examination Committee:

Dr. Ir. W.B.J. Hakvoort
Dr. J. Dasdemir
Dr. I.S.M. Khalil
Ir. B. Gerlagh

UNIVERSITY OF TWENTE.

Faculty of Engineering Technology
Department of Mechanics of Solids, Surfaces and Systems
Chair of Precision Engineering

Abbreviations

Abbreviation	Stands For
COR	Coefficient of Restution
DOF	Degree of Freedom
EOM	Equation of Motion
LP	Low-Pass
PE	Precision Engineering
PKM	Parallel Kinematic Manipulator

Notations

Notation	Stands For
$\dot{x}$, $\frac{d}{dt}x$	Time derivative of x
$\boldsymbol{\Psi_A}$	Reference frame A
$\boldsymbol{\Psi_{\hat{A}}}$	Estimate for reference frame A
$\boldsymbol{O_A^B}$	Origin of $\boldsymbol{\Psi_A}$ expressed in $\boldsymbol{\Psi_B}$
$\boldsymbol{O_A}$	Origin of $\boldsymbol{\Psi_A}$ expressed in the global reference frame
$\boldsymbol{R_A^B}$	Rotation matrix mapping points in $\boldsymbol{\Psi_A}$ to $\boldsymbol{\Psi_B}$
$\boldsymbol{R_A}$	Rotation matrix mapping points in $\boldsymbol{\Psi_A}$ to global reference frame
$\boldsymbol{p_p^A}$	Point p expressed in $\boldsymbol{\Psi_A}$
$\boldsymbol{p_p}$	Point p expressed in global reference frame
$\boldsymbol{\hat{p}_p}$	Estimate of $\boldsymbol{p_p}$
$p_{p,x}$	x-component of $\boldsymbol{p_p}$
$\boldsymbol{q_A^B}$	Unit quaternion representing orientation of $\boldsymbol{\Psi_A}$ in $\boldsymbol{\Psi_B}$
$\boldsymbol{q_A}$	Unit quaternion representing orientation of $\boldsymbol{\Psi_A}$ in global reference frame
$q_{A,0}$	Scalar part of unit quaternion $\boldsymbol{q_A}$
$\boldsymbol{\bar{q}_A}$	Vector part of unit quaternion $\boldsymbol{q_A}$
$\boldsymbol{\Upsilon_p} = \begin{bmatrix} \boldsymbol{p_p} \\ \boldsymbol{q_p} \end{bmatrix}$	Pose of $\boldsymbol{\Psi_p}$ expressed in $\boldsymbol{\Psi_G}$, consisting of point $\boldsymbol{p_p}$ and unit quaternion $\boldsymbol{q_p}$
$\boldsymbol{\tilde{x}}$	Skew-symmetric matrix associated with vector $\boldsymbol{x}$

Summary

In the recent past, the Precision Engineering group of the University of Twente developed the T-Flex; a fully flexure-based, six degrees of freedom parallel kinematic manipulator with a large range of motion. The T-Flex is the perfect showpiece to demonstrate the accomplishments of the PE group and the development of flexure-based robotics on fairs and events. To showcase T-Flex's force sensitivity, reproducibility and accelerations through its workspace, a demonstration is developed around the peg-in-hole problem. As part of the setup, a visually attractive peg and hole are designed and manufactured. The demonstration involves inserting the peg and measuring the hole, followed by a dancing motion to show accelerations and the workspace, and finally re-inserting the peg to display reproducibility. To solve the peg-in-hole problem, an impedance control-based strategy without vision or force feedback is developed. The compliance of the controller varies throughout the demonstration. During phases of interaction with the environment, a soft controller is implemented to limit the interaction forces. To increase the bandwidth of the system during the dancing motion and to improve accuracy during the re-insertion, a stiffer controller is implemented. The stiff controller has a bandwidth of 9 Hz and exhibits a maximum steady-state tracking error in the task space of 45 µm when the set of model parameters is well-trained. Further increase of the controller stiffness is limited by destabilization of the first parasitic eigenmode. The hole measurement procedure shows high reproducibility, and the peg-in-hole task is performed successfully during the observed instances.

Contents

1 Introduction

1.1 Background

In the recent past, the Precision Engineering (PE) group of the University of Twente developed the T-Flex [1]; a six degrees of freedom (DOF) parallel kinematic manipulator (PKM) with a large range of motion, shown in Fig. 1. PKMs are renowned for achieving high accelerations and precision due to a low moving mass and high rigidity [2]. Besides that, the T-Flex is fully flexure based. Flexures are ideal for high-precision applications because they allow for high dynamic performance, repeatability and accuracy due to the absence of friction, hysteresis and backlash [3]. However, the flexure's limited range of motion generally constrains the workspace of the flexure-based mechanism. The PE research group developed a set of flexure joints with a large range of motion [4, 5] which facilitate the T-Flex with an unprecedented translational workspace of 5.5 dm^3 [6] at a repeatability of 0.35 µm RMS. Furthermore, the T-Flex allows for accelerations surpassing 10 g. This unique combination of properties makes the T-Flex the perfect showpiece to demonstrate the accomplishments of the PE group and the development of flexure-based robotics on fairs and events.

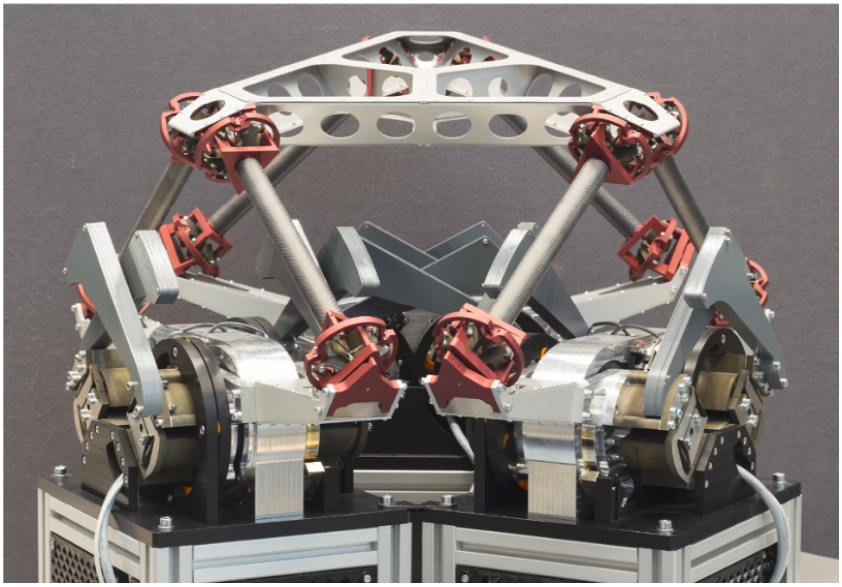

Figure 1: The T-Flex [1].

To show the potential of the T-Flex, previous efforts have been made towards a ball-bouncing demonstration with the T-Flex [7, 8]. From this work, it was concluded that obtaining a working 3D ball-bouncing demonstration still requires substantial effort. In order to have guarantee of a functional and appealing demonstration for the T-Flex by the end of this graduation process, it was decided to first focus on a peg-in-hole demonstration before continuing with the ball-bouncing demonstration.

The peg-in-hole task is a benchmark test in (assembly) robotics [9], and is deemed a suitable basis for showcasing the T-Flex's features. By inserting the peg in the hole, the force-transparency of the T-Flex is exploited. By measuring the hole and re-inserting the peg later, the reproducibility of the T-Flex is displayed - a feature not explicitly exposed in the ball-bouncing demonstration. In between the insertion and re-insertion of the peg, the accelerations through the workspace can be demonstrated by implementing a little "dancing" motion.

Developing the peg-in-hole demonstration required more effort than initially anticipated. As a result, the project scope was shifted to focus solely on completing the peg-in-hole demonstration, rather than developing a peg-in-hole demonstration and continuing with the work on the ball-bouncing demonstration.

1.2 Previous Work

1.2.1 Ball-Bouncing Demonstration

Van der Werff investigated various options for a demonstration to show the potential of the T-Flex [7]. After a comparative ranking, it was decided that a ball-bouncing demonstration offers the most appropriate demonstration of the T-Flex. The ball-bouncing demonstrates the T-Flex's workspace and accelerations, and its force-sensitivity is used to estimate the linear impulse of the ball.

In her efforts towards a ball-bouncing demonstration, Van der Werff developed a working 1-D demonstration. Furthermore, she developed a 2-D bouncing algorithm and proved the feasibility of the 3-D ball-bouncing demonstration. However, the method developed to estimate the linear impulse given to the ball proved to be inaccurate due to the excitation of higher-order dynamics.

O'Sullivan managed to improve this estimate and investigated the options to obtain a better estimate for the coefficient of restitution (COR) of the ball [8]. Obtaining a better estimate for the COR proved challenging, and no straightforward relations were uncovered. Furthermore, the excitation of higher-order dynamics results in vibrations causing the bolts in the joints of the T-Flex to loosen during operation. This, in combination with other pending challenges, means that obtaining a working ball-bouncing demonstration in 3D still requires substantial effort.

1.2.2 Peg-In-Hole Task

The peg-in-hole problem is well-studied in the field of robotics. The peg-in-hole operation forms the basis of many automated assembly operations [9]. Applications in the industry range from mating splined axle assemblies [10] to the joining of electrical connectors [11].

The peg-in-hole problem consists of two components: locating the hole and inserting the peg. Hole localization can be achieved through vision-based systems or searching trajectories [12]. Given that previous work on the T-Flex already supports trajectory-based hole localization, vision-based approaches are not considered to limit the complexity of the system.

Common search trajectories are: spiral trajectories [10, 13–15], concentric circles [10], a random search [14–16], and joining of discretized points in the search area [10, 16]. As will be discussed in section 2.2.3, the search area for the designed setup consists of an annulus. To have a smooth searching trajectory and optimal coverage of the searching area [13], the spiral trajectory is selected to localize the hole.

Following the localization of the hole is the insertion step. Due to the remaining positional uncertainty, interaction between the peg and the hole is inevitable and a form of compliance in the system is required to insert the peg in the hole [12]. This can be achieved through passive compliant mechanisms [12, 15] or by compliant control [12, 13, 15]. To limit system complexity, compliance is introduced in the system through control.

The remaining insertion strategies can be divided into model-based assembly strategies and learning-based strategies [12]. Because the circular peg-in-hole problem is an extensively studied problem, many model-based assembly strategies exist and the learning-based strategies are not further considered.

Model-based assembly strategies use either kinematic data or force and torque data about the interaction between the peg and the hole. Strategies using kinematic data use the concept of attractive region in environment [17]. In this method, the peg and hole are kept under a fixed relative orientation and the peg probes the surface with the hole in it. The forward kinematics of the robot are used to calculate tip positions, resulting in a map where the peg is partially inserted in the hole at the lowest point in the map. Based on the information in the map, sensorless insertion is achieved by generating forces and moments accordingly.

Data regarding the interaction forces between the peg and hole are generally used in two ways. One common approach uses a quasi-static contact model. In this approach, the peg speeds are kept low, and a force/torque sensor is mounted between the peg and the robot. The measured interaction forces are used to apply corrective actions for aligning the peg with the hole [18]. The corrective actions are based on the interaction model of the peg and the hole. Because of the low speeds, this insertion method is relatively slow.

The other approach utilizing interaction forces and moments between the peg and the hole is to make a Force/-Torque (FT) map [19, 20]. In this method, the search area is probed with the peg, while the interaction forces and moments are stored in a map. When the map is complete, an additional model is used to interpret the data and determine the pose of the hole. This approach proves to be sensitive to noise and does not guarantee insertion of the peg in the hole [19, 20].

Recent efforts focus on sensorless methods to insert the peg in the hole [13, 21, 22]. These methods require a structured environment, but omit the need for additional F/T data and are generally faster than the other aforementioned trajectory-based methods. To avoid the need for an extensive contact model, feedback of the F/T data or model to interpret the measurement data, the method developed by H. Park et al. [13] is selected to base the peg-in-hole assembly strategy on and ensure swift insertion.

The original approach by Park et al. is designed to be implemented on an 8-DOF industrial serial manipulator. However, the problem is a 6-DOF problem, the two additional DOFs are not explicitly used. As a result, the approach can be adjusted to be implemented on the T-Flex.

The original approach utilizes a coarse vision system to obtain an initial estimate of the pose of the hole. This estimate is the starting point of the insertion procedure. The forward kinematics of the serial industrial manipulator result in a positional uncertainty of the end-effector of several millimeters. The approach focuses on the insertion of the peg in the face of this positional uncertainty. Since the setup for the demonstration with the T-Flex will not be equipped with a vision system, the search trajectory will be adapted to localize the hole.

In the approach by Park et al., hybrid position/force control is used. In this control framework, the task space is divided into two types of directions: directions where the position is controlled and directions where force is controlled [23]. In the selected peg-in-hole assembly strategy, the force control exerts a downward force perpendicular to the surface with the hole, while the peg is moved parallel to the surface by position control, searching for the hole.

The position control is proportional only and allows for an error in the end-effector position, providing a tuneable compliance of the manipulator. The force control is implemented as a constant feed-forward term. By optimizing the compliance and force control parameters, the peg can be successfully inserted into the hole. Due to the problem-specific tuning of the compliance and force parameters, the implementation is not universally applicable to any peg-in-hole problem. This is not considered to be a problem, since the demonstration setup forms a controlled environment.

1.3 Problem Statement

The goal of this thesis is to develop a peg-in-hole demonstration for the T-Flex, which is suitable to be shown at fairs and events where the PE group is present. The demonstration should highlight the unique combination of features of the T-Flex, being: high precision, accuracy and accelerations, large workspace and force transparency due to absence of internal friction and backlash/play.

The desired sequence of the peg-in-hole demonstration is as follows:

- locate the hole and insert the peg exploiting the force transparency
- determine the pose of the hole
- extract the peg from the hole and perform a little dance to display the workspace and accelerations
- re-insert the peg in the hole exploiting the reproducibility

The required tolerances between the peg and the hole during the re-insertion processes depend on the attainable accuracy of the controller. Therefore, understanding the limitations of the implemented control is essential in determining the minimum clearance required between the peg and the hole.

1.4 Contribution

This thesis contains three contributions:

1. In this thesis, the peg-in-hole assembly strategy by Park et al. [13] is adapted and extended for the demonstration with the T-Flex. The original strategy is designed for an 8-DOF serial manipulator and uses a camera system to obtain an initial estimate of the position of the hole. The implementation is adapted to the 6-DOF T-Flex, and the need for a camera system is omitted by implementing a trajectory-based search for the hole.
2. This thesis shows the efficacy of the proposed method using a hardware implementation on the T-Flex. The limits on the reproducibility of the system in free space are investigated, as well as the peg re-insertion into the hole and the reproducibility of the hole measurement procedure.
3. This thesis illustrates how excellent force transparency from flexure-based design enables effective task execution while interacting with an unknown environment. The force-transparency, precision, accuracy, workspace and accelerations of the T-Flex are displayed, giving a practical representation of the PE group's research focus.

1.5 Report Outline

Chapter 1 is the introductory chapter where the motivation for the presented work is given and an approach for the peg-in-hole problem is selected. In Chapter 2 the various steps of the demonstration are discussed. The mathematical steps involved in determining the trajectory and the pose of the hole are covered, and the control framework is discussed. Chapter 3 concerns the derivation of application-specific control parameters and the design of the peg and hole setup. Chapter 4 covers the experiments conducted to obtain the application-specific parameters, and also includes an experimental validation of the methods presented. In Chapter 5 the conclusions are drawn on the work performed, and Chapter 6 presents recommendations for future work. The appendices provide additional information to substantiate some of the claims presented in the main chapters.

2 Methodology

2.1 Compliance-Based Peg-In-Hole Assembly Strategy Without Force Feedback

To illustrate the idea of the compliance-based peg-in-hole assembly strategy proposed by Park et al. in [13], sections 2.1.1 – 2.1.3 will cover fundamental concepts of the approach, as well as the proposed control law. Starting from section 2.2, the similarities and adaptations for the demonstration with the T-Flex will be discussed.

2.1.1 Peg and Hole contact Modes

During the insertion process, four contact modes between the peg and the hole can be distinguished. The analysis of these four contact modes forms the basis for the insertion procedure and will be covered here briefly. The distinct contact modes consist of: planar contact between the peg and surface, two-point contact between the peg and the hole, three-point contact between the peg and the hole and insertion of the peg in the hole. The four modes are depicted in Fig. 2.

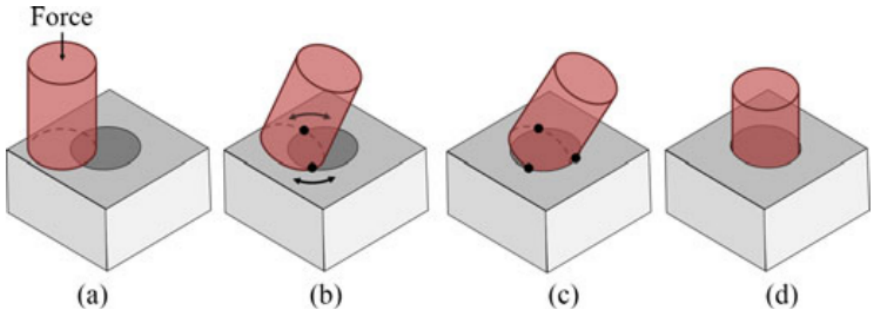

Figure 2: Contact modes in the peg-in-hole problem, retrieved from [13]. (a) Planar contact. (b) Two-point contact. (c) Three-point contact. (d) Insertion.

2.1.2 Assembly Strategy

To insert the peg into the hole, Park et al. divide the task into three actions. During every action a combination of different unit motions is applied to the peg. These four motions are visualized in Fig. 3, and include: pushing, rubbing, wiggling and screwing. The pushing motion is generated by applying a constant downward force in the estimated z-direction of the hole (Fig. 3a). The rubbing motion is produced by generating a spiralling reference trajectory in the estimated xy-plane of the hole (Fig. 3b). The wiggling motion is produced by rotating the reference orientation about the x- and y-axis of the hole (Fig. 3c). And the screwing motion is generated by rotating the reference orientation about the z-axis of the hole (Fig. 3d).

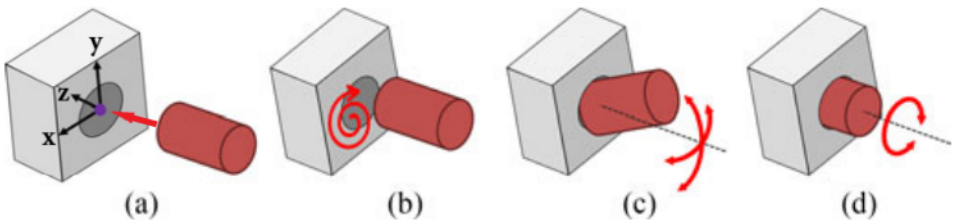

Figure 3: Unit motions for peg-in-hole assembly, retrieved from [13]. (a) Pushing. (b) Rubbing. (c) Wiggling. (d) Screwing.

To guide the robot through the insertion process, the procedure has been divided into actions as shown in Fig. 4: reaching, searching, and inserting. During every action, one or multiple unit motions are combined to proceed with the insertion.

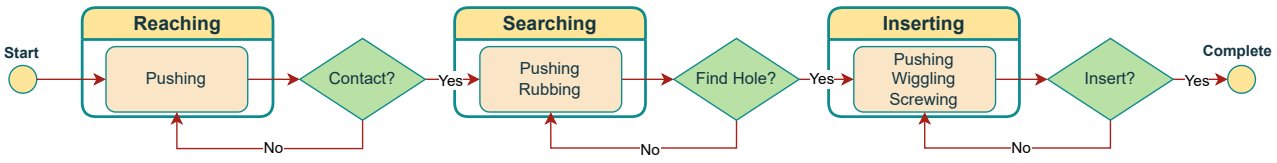

Figure 4: Flowchart of the assembly strategy.

The process starts with reaching: the robot is provided with an approximate pose of the hole, which is provided by the external camera system. The robot reaches for the hole by exerting the pushing motion. At some point, the peg will be blocked by the surface or the hole. If the tip velocity of the peg in z-direction reaches below a certain threshold for a prolonged period ($\|\dot{p}_{p,z}(t)\| < v_{th,reach} \quad \forall \quad t \in [t_i, t_i + \Delta T_{reach}]$), the robot identifies contact and proceeds to the searching state.

In the searching state, pushing and rubbing are combined. This results in the spiral motion as shown in Fig. 3b. The details about the trajectory and control of the robot will be discussed in the methodology. Park et al show that if the pushing force in the z-direction and the radial force resulting from the proportional action in the xy-direction are well matched, the peg will be caught by the hole in the three-point contact state. The tip velocity in the xy-plane is continuously monitored. If the magnitude of this velocity is below a threshold for a prolonged time ($\|\dot{\boldsymbol{p}}_{p,xy}(t)\| < v_{th,search} \quad \forall \quad t \in [t_i, t_i + \Delta T_{search}]$), the robot recognizes that the hole is found.

After the searching state, the robot continues with inserting. During the inserting step, the unit motions of pushing, wiggling and screwing are combined. The wiggling will cause the peg to slip into the hole. After the peg has entered the hole, misalignment can cause the peg to jam in the hole. Applying a screwing motion helps to alleviate vertical friction forces and fully inserts the peg into the hole [24]. When the peg is fully inserted in the hole, the velocity in the z-direction does not change anymore and the robot recognizes that the peg is fully inserted in the hole ($\|\dot{p}_{p,z}(t)\| < v_{th,insert} \quad \forall \quad t \in [t_i, t_i + \Delta T_{insert}]$).

2.1.3 Control for the Strategy

The dynamics of the 8-DOF manipulator in joint space can be described by the follwing equation:

$$M(\boldsymbol{q})\ddot{\boldsymbol{q}} + \boldsymbol{h}(\boldsymbol{q}, \dot{\boldsymbol{q}}) + \boldsymbol{f}(\boldsymbol{q}) + \boldsymbol{\tau}_{fric}(\dot{\boldsymbol{q}}) = \boldsymbol{\tau}_m + \boldsymbol{\tau}_{ext} \tag{1}$$

where $\boldsymbol{q} \in \mathbb{R}^{8\times1}$ denotes a vector in the joint space of the manipulator. $M(\boldsymbol{q}) \in \mathbb{R}^{8\times8}$ is the inertia matrix, $\boldsymbol{h}(\boldsymbol{q}, \dot{\boldsymbol{q}}) \in \mathbb{R}^{8\times1}$ contains the centrifugal and Coriolis terms and $\boldsymbol{f}(\boldsymbol{q}) \in \mathbb{R}^{8\times1}$ contains the gravitational forces. $\boldsymbol{\tau}_{fric}(\dot{\boldsymbol{q}}) \in \mathbb{R}^{8\times1}$ represents the frictional torques in the actuated joints, $\boldsymbol{\tau}_m \in \mathbb{R}^{8\times1}$ are the motor torques and $\boldsymbol{\tau}_{ext} \in \mathbb{R}^{8\times1}$ is the torque in the joints resulting from externally applied forces and moments.

The proposed control law, which considers the pose of the end-effector, gravity compensation, frictional compensation, and damping in joint space, is given by:

$$\boldsymbol{\tau}_m = -D\dot{\boldsymbol{q}} + J^T \begin{bmatrix} \boldsymbol{f}_m \\ \boldsymbol{m}_m \end{bmatrix} + \hat{\boldsymbol{f}}(\boldsymbol{q}) + \hat{\boldsymbol{\tau}}_{fric}(\dot{\boldsymbol{q}}) \tag{2}$$

where $\hat{\boldsymbol{f}}(\boldsymbol{q})$ and $\hat{\boldsymbol{\tau}}_{fric}(\dot{\boldsymbol{q}})$ form estimates of the gravitational and frictional torques. Matrix $D \in \mathbb{R}^{8\times8}$ is a diagonal damping matrix, providing absolute damping based on the joint velocities. The geometric Jacobian matrix $J \in \mathbb{R}^{6\times8}$ maps the joint velocities to end-effector velocities in $\boldsymbol{\Psi}_{\boldsymbol{G}}$. The control wrench $\begin{bmatrix} \boldsymbol{f}_m^T & \boldsymbol{m}_m^T \end{bmatrix}^T \in \mathbb{R}^{6\times1}$ contains the hybrid position/force control action and is discussed below.

In the proposed assembly strategy, the robot is capable of separately generating force and position control along the desired directions. The separation of force and position control is achieved by specifying $\boldsymbol{f}_m$ as:

$$\boldsymbol{f}_m = k_v \boldsymbol{\Omega}(\hat{\boldsymbol{p}}_h - \boldsymbol{p}_p) + \boldsymbol{f}^* \tag{3}$$

The first half of this equation acts as a proportional controller, acting on the error between the estimated position of the hole $\hat{\boldsymbol{p}}_h$ and the position of the peg tip $\boldsymbol{p}_p$ multiplied by a spring constant k_v. Matrix $\boldsymbol{\Omega}$ is a so-called generalized task-specification matrix that is used to separate the position control from the force control [25], and is discussed below. The additional force control input required to generate the unit motions is given by $\boldsymbol{f}^*$.

Matrix $\boldsymbol{\Omega}$ separates the position control from the force control. With the local frames of the peg and the hole specified as in Fig. 5, $\boldsymbol{\Omega}$ is specified as follows:

$$\boldsymbol{\Omega} = \hat{\boldsymbol{R}}_h \boldsymbol{\Sigma} \hat{\boldsymbol{R}}_h^T \tag{4}$$

with $\boldsymbol{\Sigma}$ being a 3-by-3 force specification matrix. This force specification matrix is used to specify the directions in the local hole frame $\hat{\boldsymbol{R}}_h$ along which the proportional position controller should act. For example, if it is desired to have the positional control only acting in the xy-plane of the hole, and not in the z-direction, $\boldsymbol{\Sigma}$ would be specified as:

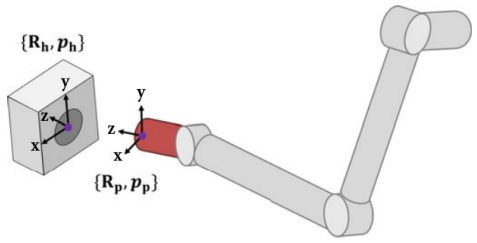

Figure 5: Local frames of peg and hole, adapted from [13].

$$\boldsymbol{\Sigma} = \begin{bmatrix} 1 & 0 & 0 \\ 0 & 1 & 0 \\ 0 & 0 & 0 \end{bmatrix} \tag{5}$$

When $\boldsymbol{\Omega}$ is used to apply position control in the xy-plane, $\boldsymbol{f^*}$ can be used to generate a force control input in the z-direction of the hole. To generate a force f_z that pushes in the z-direction of the hole, $\boldsymbol{f^*}$ can be written as:

$$\boldsymbol{f^*} = \hat{\boldsymbol{R}}_h \begin{bmatrix} 0 \\ 0 \\ f_z \end{bmatrix} \tag{6}$$

The moments $\boldsymbol{m}_m$ in the wrench vector are calculated by:

$$\boldsymbol{m}_m = \boldsymbol{K}_\omega \boldsymbol{E}_r(\boldsymbol{R}^* \hat{\boldsymbol{R}}_h, \boldsymbol{R}_p) \tag{7}$$

where $\boldsymbol{K}_\omega \in \mathbb{R}^{3\times3}$ is a diagonal matrix specifying an orientation control gain along the three axes. $\boldsymbol{R}_p$ is the rotation matrix specifying the orientation of the peg in $\boldsymbol{\Psi_G}$, and $\boldsymbol{R}^*$ is the desired orientation of the peg relative to the hole, expressed in local frame $\boldsymbol{\Psi}_h$ that aligns with the hole. The product $\boldsymbol{R}^* \hat{\boldsymbol{R}}_h$ forms the desired orientation of the peg in $\boldsymbol{\Psi_G}$. $\boldsymbol{E}_r(\boldsymbol{R}^* \hat{\boldsymbol{R}}_h, \boldsymbol{R}_p)$ is a 3-by-1 error vector that represents the error between the orientation of matrices $\boldsymbol{R}^* \hat{\boldsymbol{R}}_h$ and $\boldsymbol{R}_B$ and specifies a metric for a misalignment in the three axes:

$$\boldsymbol{E}_r(\boldsymbol{R_A}, \boldsymbol{R_B}) = [\boldsymbol{R}_{A(:,1)} \times \boldsymbol{R}_{B(:,1)} + \boldsymbol{R}_{A(:,2)} \times \boldsymbol{R}_{B(:,2)} + \boldsymbol{R}_{A(:,3)} \times \boldsymbol{R}_{B(:,3)}] \tag{8}$$

where $\boldsymbol{R}_{A(:,1)}$ specifies the first column of $\boldsymbol{R}_A$, and so on. In Appendix C it is shown that $\boldsymbol{m}_m$ does not scale linearly with the rotational error, but that this is not problematic for sufficiently small rotations that are centered about a neutral position.

2.2 Outline of T-Flex Demonstration

The peg-in-hole demonstration with the T-Flex is divided into six states: reaching, searching, inserting, measuring, dancing and re-inserting. The reaching, searching and inserting states are used to localize the hole and insert the peg similarly to the assembly strategy proposed in [13]. The key differences with the approach presented in [13] will be highlighted in sections 2.2.2, 2.2.3 and 2.2.4 respectively.

In the first four states, the system will be controlled by a soft controller to allow for relatively large pose errors without excessive force generated on the peg. During the demonstrating and re-inserting states a stiffer controller is implemented to improve tracking of the reference. When the demonstration is finished, the position of the hole can be altered to demonstrate that the location of the hole is not pre-determined. Fig. 6 shows the flowchart of the total demonstration, the specific parameters mentioned in the flowchart will be covered later in this chapter.

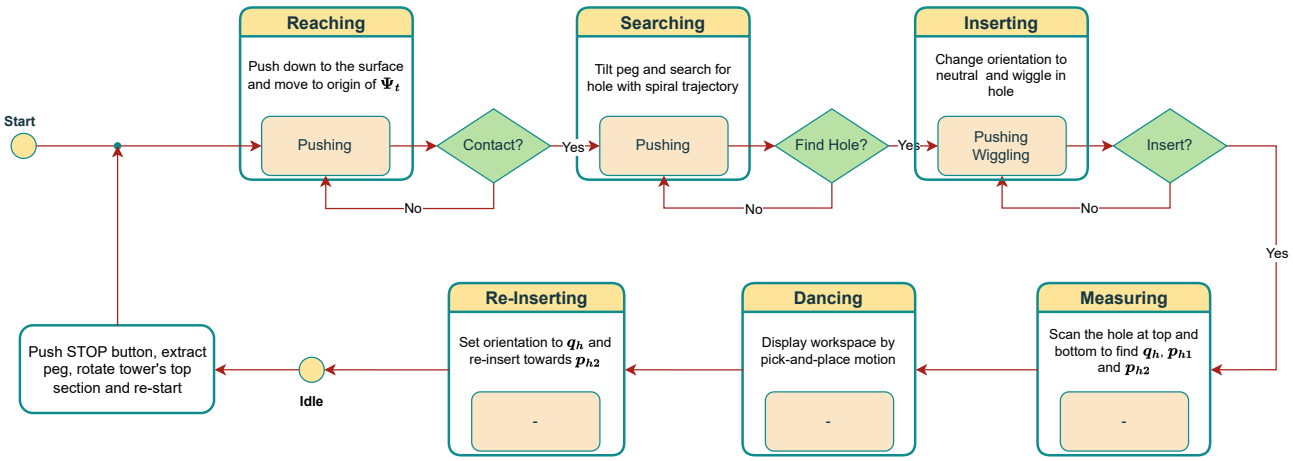

Figure 6: Flowchart of the peg-in-hole demonstration with the T-Flex.

Section 2.2.1 will briefly introduce the hardware used, and sections 2.2.2 – 2.2.7 will define the actions of every state of the demonstration. Chapter 3 will focus on determining the application-specific parameter values for the parameters introduced in this chapter.

2.2.1 Peg and Hole Setup

The peg and hole are depicted in Fig. 7. Attached to the tip center of the peg is frame $\boldsymbol{\Psi_p}$, as shown in Fig. 8. Attached to the top center of the tower is frame $\boldsymbol{\Psi_t}$, as shown in Fig. 9. Fig. 10 shows the global reference frame $\boldsymbol{\Psi_G}$ as well as the reference frame attached to the T-Flex's end-effector $\boldsymbol{\Psi_E}$.

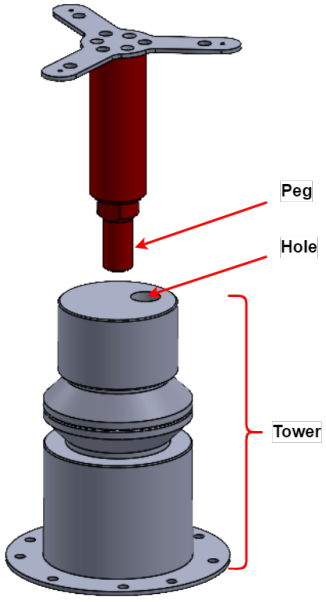

Figure 7: CAD model of peg and hole.

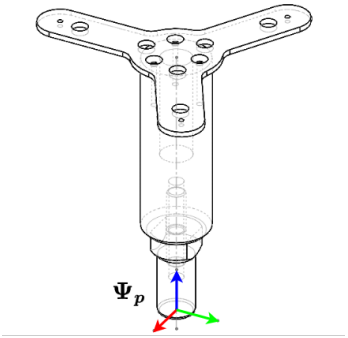

Figure 8: Location of Ψ_p on peg.

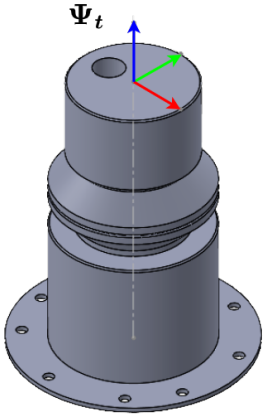

Figure 9: Location of Ψ_t on tower.

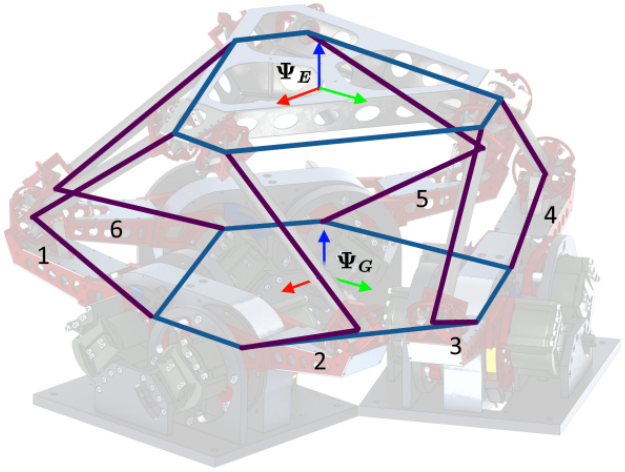

Figure 10: Frames $\boldsymbol{\Psi_E}$ and $\boldsymbol{\Psi_G}$ in the T-Flex (adapted from [26]).

The pose of $\boldsymbol{\Psi_p}$ in the global frame $\boldsymbol{\Psi_G}$ is expressed by $\boldsymbol{\Upsilon_p} = \begin{bmatrix} \boldsymbol{p_p}^T & \boldsymbol{q_p}^T \end{bmatrix}^T$, where $\boldsymbol{p_p}$ is a set of linear coordinates (x-, y- and z-position) of the origin and $\boldsymbol{q_p}$ is a unit quaternion representing the orientation. The pose of $\boldsymbol{\Psi_t}$ in $\boldsymbol{\Psi_G}$ is expressed by $\boldsymbol{\Upsilon_t}$.

Fig. 11 shows how the tower and the peg are positioned in the T-Flex: the tower is placed in the center of the T-Flex, and the peg is attached to the end-effector. The top and bottom sections of the tower are clamped together using a quick-release clamp. The clamp can be released to rotate the hole about the longitudinal axis of the tower. Further details of the peg and the hole will be covered in chapter 3.

2.2.2 Reaching

When the actuators of the T-Flex are off, the peg naturally rests on the surface of the tower as is shown in Fig. 11. When the T-Flex turns on and enters the reaching state, the peg is commanded to move to the center of the tower and continually push down in the estimated z-direction of the tower. In this step, $\boldsymbol{\Psi_t}$ is assumed to align with $\boldsymbol{\Psi_G}$. Three seconds after entering the reaching state the state changes to searching. Before the state transition, a measurement of the z-height of the tip is stored as the estimated height of the surface of the tower ($\hat{p}_{t,z}$).

This reaching state differs from that of Park et al. in that the peg is commanded to a predefined position at the center of the tower, whereas Park's implementation uses input of an external camera system to estimate the location of the hole and directly reaches for the hole. In this work, the hole is localized in the searchin phase through a trajectory-based search. In the approach by Park et al., the z-velocity of the peg is monitored to detect contact with the hole surface. However, in the T- Flex setup, the peg touches the surface of the tower during the reaching state. Therefore, the z-velocity of the peg is zero during the entire reaching state. Therefore, the state transitions after three seconds, as observations show that the system reaches equilibrium within this time interval.

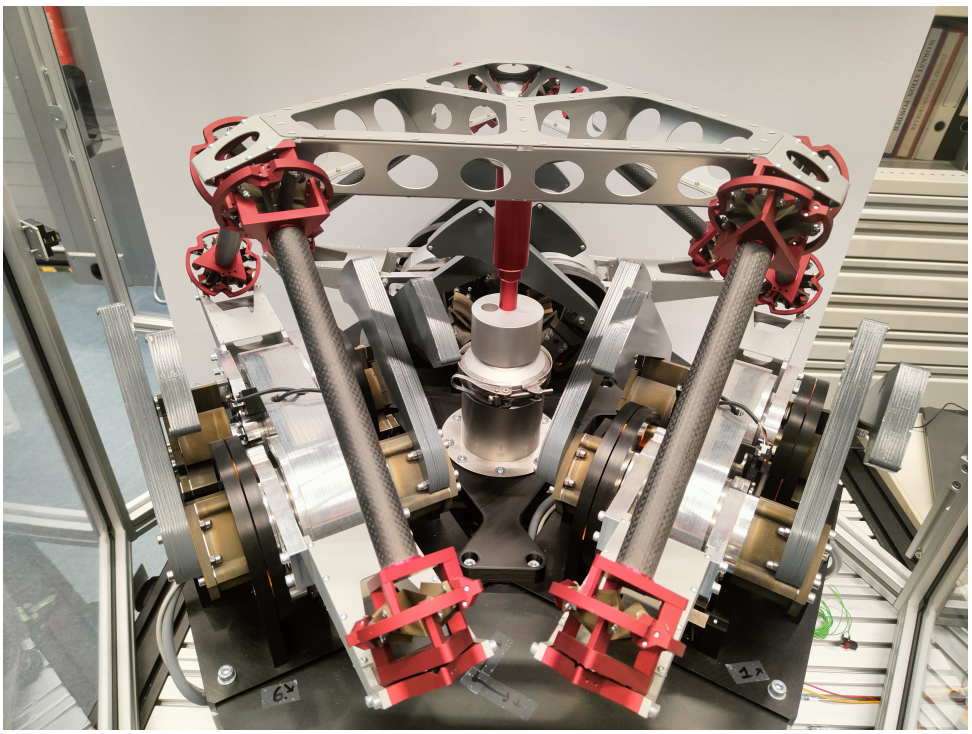

Figure 11: Setup of the peg and tower in the T-Flex.

2.2.3 Searching

During the searching state, the peg is continually pushed downward along the estimated z-direction of the tower. During this state, the z-direction of the tower is estimated to be perpendicular to the z-direction of $\boldsymbol{\Psi_G}$.

Since the hole location can be rotated around the longitudinal axis of the tower, it is known beforehand that the hole must be located at a distance r from the origin of $\boldsymbol{\Psi_t}$ ($O_{\boldsymbol{t}}$). The xy-coordinates of $O_{\boldsymbol{t}}$ and $O_{\boldsymbol{G}}$ do not coincide perfectly. Therefore, the xy-coordinates of $O_{\boldsymbol{t}}$ are estimated beforehand ($\begin{bmatrix}\hat{\boldsymbol{p}}_{\boldsymbol{t},x} & \hat{\boldsymbol{p}}_{\boldsymbol{t},y}\end{bmatrix}^T$). The spiral trajectory is generated around the estimate of this offset. The estimate includes an inherent degree of uncertainty. This means that the center of the hole is situated somewhere between a minimum radius (r_{s^-}) and a maximum radius (r_{s^+}) from $\begin{bmatrix}\hat{\boldsymbol{p}}_{\boldsymbol{t},x} & \hat{\boldsymbol{p}}_{\boldsymbol{t},y}\end{bmatrix}^T$.

To start the searching procedure, the peg is moved in the x-direction by a distance r_{s^-}, and tilted about the x-axis by an angle α_{tilt}. The tilting of the peg with respect to the surface results in a single contact point between the peg and the surface as shown in Fig. 13. In the method of Park et al. the peg is not explicitly tilted. The tilt of the peg has been added because the single point of contact helps the peg to self-align with the hole when the point of contact moves over the hole [13].

Next, the peg follows a spiralling trajectory that draws a spiral from r_{s^-} to r_{s^+}. An example of such a trajectory can be seen in Fig. 12. The incremental distance between every rotation of the spiral is given by Δr. If Δr is chosen sufficiently small, the tip of the peg will eventually fully enter the hole due to the downward force and the compliant behavior of the controller.

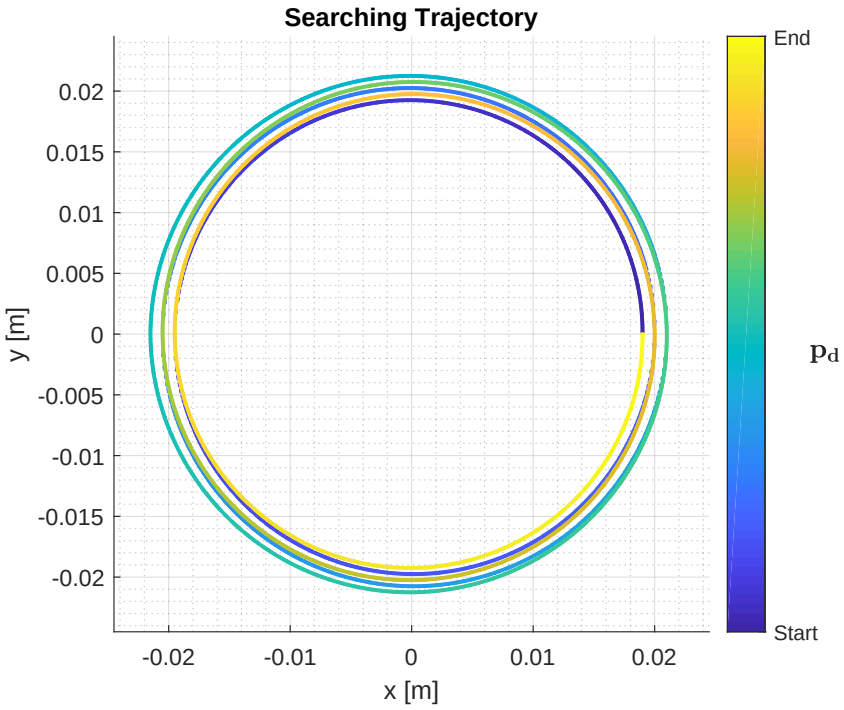

Figure 12: Spiral trajectory generated between r_{s^-} and r_{s^+}.

Fig. 14 depicts the searching trajectory. To generate the searching trajectory, a constant scalar velocity for the peg is selected: v_s. This velocity - in combination with the (current) radius of the spiral - dictates the angular rate ω_s of the spiral trajectory. For every timestep, the new radius r_i and its angle with the z-axis θ_i is calculated. Vector $\boldsymbol{e_s}$ is a unit vector specifying the direction of r_i. From v_s, the reference ($\boldsymbol{\Upsilon_d} = \begin{bmatrix}\boldsymbol{p_d^T} & \boldsymbol{q_d^T}\end{bmatrix}^T$) can be updated for every timestep (with sample time T) as follows:

$$
\begin{aligned}
\omega_{s,i} &= \frac{v_s}{r_{i-1}} \\
\theta_i &= \theta_{i-1} + \omega_{s,i} T \\
r_i &= r_{i-1} + \frac{(\theta_i - \theta_{i-1})\Delta r}{2\pi} \\
\boldsymbol{e_s} &= \begin{bmatrix}\cos(\theta_i) & \sin(\theta_i) & 0\end{bmatrix} \\
\boldsymbol{p_d} &= r_i \boldsymbol{e_s} \\
\boldsymbol{q_d} &= \begin{bmatrix}\cos\left(\frac{\alpha_{tilt}}{2}\right) & \sin\left(\frac{\alpha_{tilt}}{2}\right)\boldsymbol{e_s}\end{bmatrix}
\end{aligned}
\tag{9}
$$

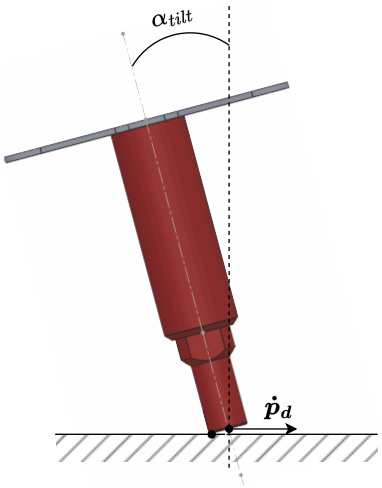

Figure 13: Pose of peg when scanning surface.

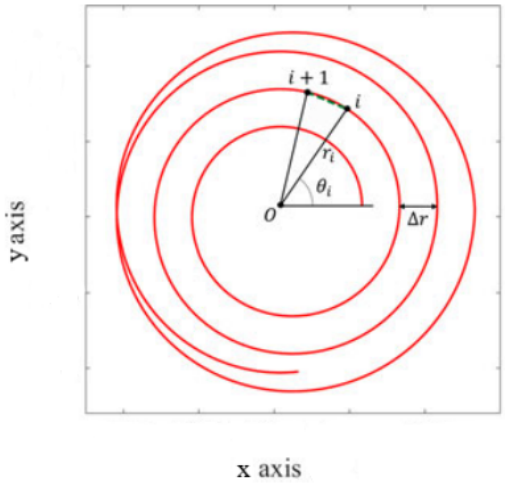

Figure 14: Illustration of searching trajectory, adapted from [13].

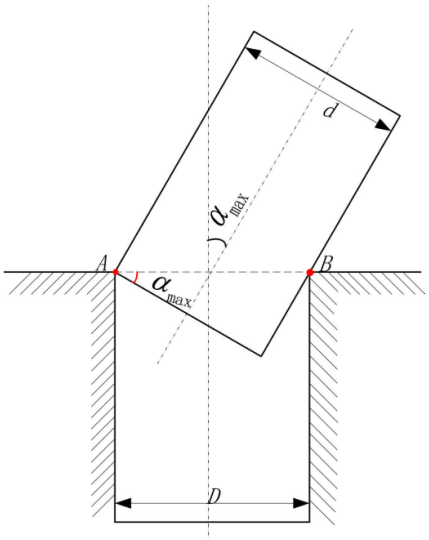

Figure 15: Maximum peg tilt α_{max} [15].

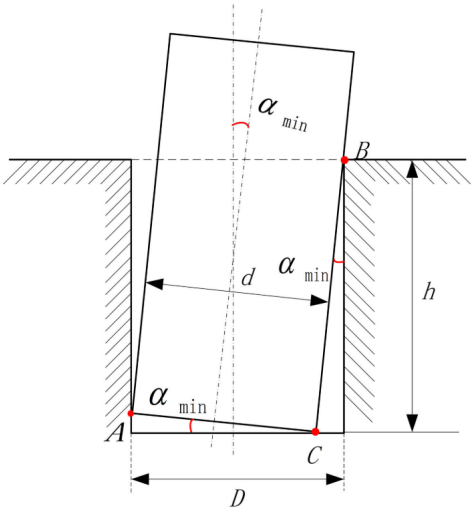

Figure 16: Minimum peg tilt α_{min} [15].

α_{tilt} is chosen such that the top of the peg can fully enter the hole when the center of the peg moves over the center of the hole. If α_{tilt} is too big, the peg will not enter the hole. The maximum tilt angle (α_{max}) that allows the peg to enter the hole can be calculated as follows [15]:

$$\alpha_{max} = \arccos\left(\frac{d}{D}\right) \tag{10}$$

where d is the diameter of the peg and D is the diameter of the hole.

During the searching state, the tip velocity of the peg in the z-direction ($\dot{p}_{p,z}$) is continuously monitored. When the peg slips into the hole, a sharp peak in $\dot{p}_{p,z}$ can be seen. When the peak is detected, the state transitions to inserting.

This state transition differs from [13], where the peg velocity is monitored during the searching state and the transition occurs when the peg velocity is below a threshold for 0.3 s. Because the searching state in [13] starts from the estimated hole position, the peg might already be caught in the hole. Consequently, observing the z-velocity as presented in this work is not applicable. In this work, the peg starts the searching state from the center of the tower surface, and thus the z-velocity of the peg is a reliable indicator to detect insertion in the hole.

Initial tests showed that the peak in z-velocity is more distinct and reliable for detecting insertion than the reduction in velocity when the peg sticks in the hole. This difference can be explained by comparing the two searching trajectories. In the approach by Park et al., the searching trajectory is centered around the hole, and the peg is more likely to stick in the hole for an extended period. In the searching trajectory used in this work, the peg passes the hole as part of the spiral trajectory that centered around the middle of the tower. As a result the peg is pulled out of the hole sooner than in [13].

2.2.4 Inserting

The maximum possible angle between the peg and the hole that allows for full insertion is defined by α_{min}, as illustrated in Fig. 16. Angle α_{min} is defined in the following relation [15]:

$$D = d\cos(\alpha_{min}) + h\tan(\alpha_{min}) \tag{11}$$

where h is the depth of the hole.

Upon entering the inserting state, the peg is partially inserted in the hole under the angle α_{tilt}. Since $\alpha_{tilt} > \alpha_{min}$, the peg is jammed in the hole under the constant downward force. To have a better alignment between the peg and the hole, the reference orientation $\boldsymbol{q_d}$ is changed to match the orientation of $\boldsymbol{\Psi_G}$. When the change of reference orientation is complete, $\boldsymbol{p_p}$ is measured and set as the reference position $\boldsymbol{p_d}$. This results in decreased interaction forces between the peg and the hole.

The possibility exists that when $\boldsymbol{q_d} \neq \boldsymbol{q_G}$, the peg does not drop in the hole promptly. This can have two causes: the orientation of tower and global frame do not match ($\boldsymbol{q_t} \neq \boldsymbol{q_G}$) and/or the orientation of the peg and T-Flex's end-effector are unequal ($\boldsymbol{q_p} \neq \boldsymbol{q_E}$) as illustrated in Fig. 17. To overcome the misalignment that is unknown a priori, the peg is commanded to exert a wiggling motion around the neutral orientation. Due to the downward force and the wiggling motion, the peg is fully inserted in the hole. The only difference with [13] in this regard is that the additional screwing motion is not generated. The peg is reliably inserted without this additional motion, and is therefore left out.

During the inserting state, $p_{p,z}$ is continuously monitored. The state transitions to the measuring state when $p_{p,z}$ is below the estimated height of the tower minus an insertion depth d_{insert} ($\hat{p}_{p,z} < \hat{p}_{t,z} - d_{insert}$). In their method, Park et al. monitor the z-velocity during insertion and mark the task complete when the z-velocity is below a threshold for 0.3 s. In contrast, this work monitors the insertion depth directly. Since the tower height is known from the measurement in the reaching state, this provides a direct measure for the insertion depth, opposed to relying on a velocity-based observation.

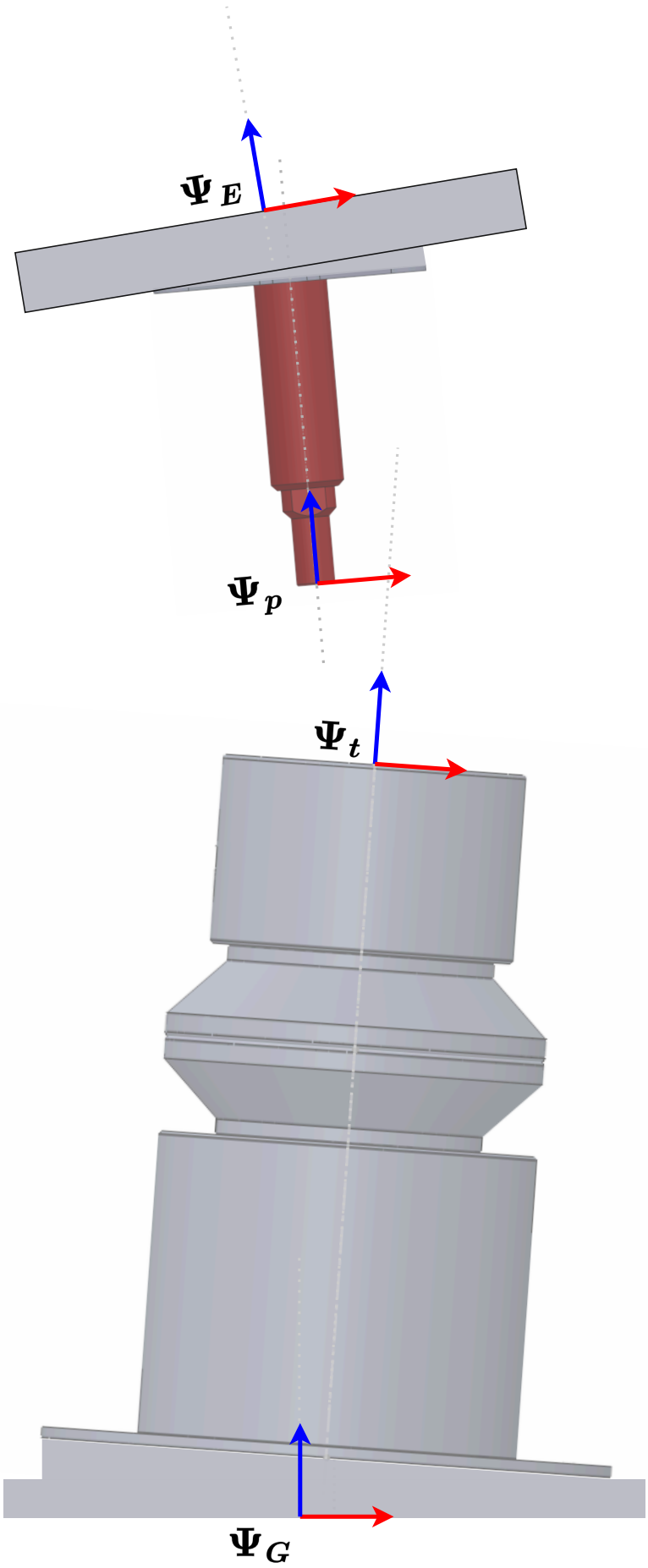

Figure 17: Demonstrative representation of misalignments in frames Ψ_E, Ψ_p, Ψ_t and Ψ_G.

2.2.5 Measuring

In the measuring state, the peg scans the hole at two heights. During these scans, three measurements are taken inside the hole. One measurement is done to determine the $\boldsymbol{q_p}$ that matches the orientation of the hole ($\boldsymbol{q_h}$). The other two measurements estimate two points ($\boldsymbol{p_{h1}}$ and $\boldsymbol{p_{h2}}$) that are central to the hole. These two points define a line along which the peg can be re-inserted. By measuring this way, there is no need to exactly determine the pose of $\boldsymbol{\Psi_p}$ with respect to $\boldsymbol{\Psi_E}$ ($\boldsymbol{\Psi_p^E}$) and of $\boldsymbol{\Psi_t^G}$. Fig. 18 illustrates $\boldsymbol{q_h}$, $\boldsymbol{p_{h1}}$ and $\boldsymbol{p_{h2}}$.

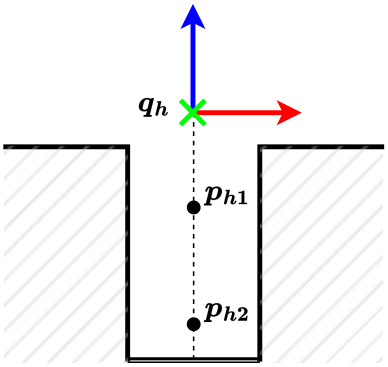

Figure 18: Schematic of hole with $\boldsymbol{q_h}$, $\boldsymbol{p_{h1}}$ and $\boldsymbol{p_{h2}}$.

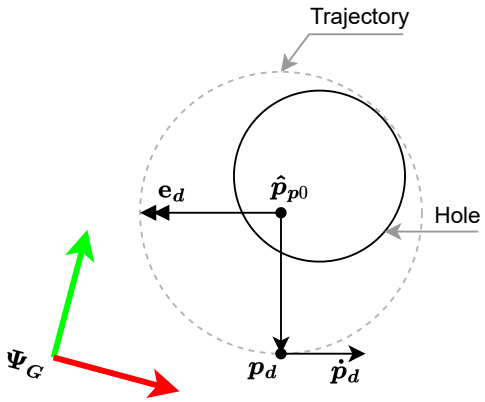

Figure 19: Top-view of scanning trajectory (trajectory is expanded to make for a clearer picture).

Upon entering the measuring state, the current peg pose $\hat{\boldsymbol{\Upsilon}}_{p0}$ is measured and passed as the reference. The scanning trajectories are generated around $\hat{\boldsymbol{\Upsilon}}_{p0}$. The set of measured orientations will be denoted with $\boldsymbol{Q_h}$, and the set of measured points for $\boldsymbol{p_{h1}}$ and $\boldsymbol{p_{h2}}$ will be denoted with $\boldsymbol{P_{h1}}$ and $\boldsymbol{P_{h2}}$ respectively.

The first measurement aims to determine $\boldsymbol{q_h}$ and $\boldsymbol{p_{h2}}$ and is conducted at the insertion height. The peg is commanded to scan the hole. During the scan, the peg is tilted in the hole so that the peg is always in contact with the hole as depicted in Fig. 20, and the tip is pointing radially outward. Fig. 19 shows how the reference for the scan is generated: by drawing a circle around $\hat{\boldsymbol{p}}_{p0}$ and tilting the peg around the axis $\mathbf{e_d}$ that is parallel to the vector spanned from $\hat{\boldsymbol{p}}_{p0}$ to $\boldsymbol{p}_d$.

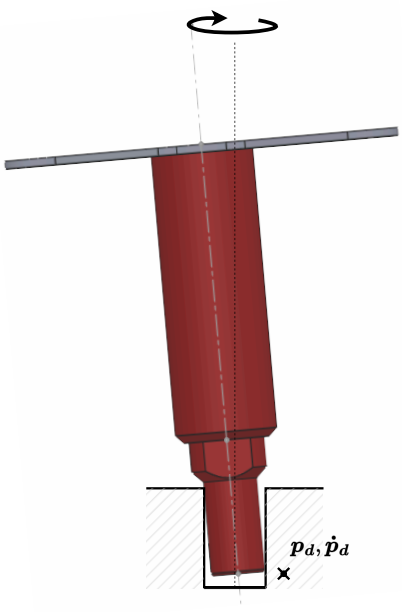

Figure 20: Interaction between peg and hole during first measurement.

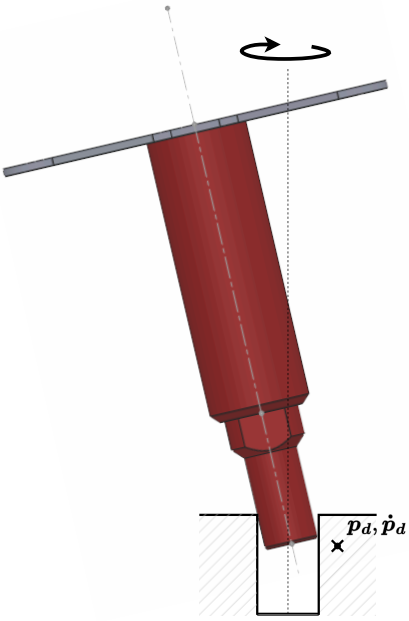

Figure 21: Interaction between peg and hole during second measurement.

The maximum angle between the peg and the hole after insertion is given by α_{min}. Because it is unknown beforehand where the center of the hole is with respect to $\hat{\boldsymbol{p}}_{\boldsymbol{p},0}$, the trajectory must draw a circle with a minimum radius r_{m^-} to make sure $\boldsymbol{p_d}$ is always pointing radially outward from the center of the hole as in Fig. 19. The trajectory $\boldsymbol{p_d}$ must be pointing radially outward to prevent the controller's linear and angular spring actions from counteracting each other. To ensure this, r_{m^-} must be twice the distance from $\hat{\boldsymbol{p}}_{\boldsymbol{p},0}$ to the center of the hole. The maximum distance from $\hat{\boldsymbol{p}}_{\boldsymbol{p},0}$ to the center of the hole can be found by inspecting the following figure:

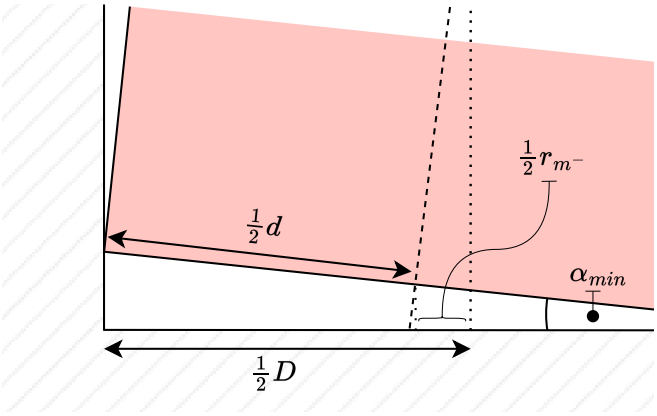

Figure 22: Representation of peg in the bottom of the hole, indicating distance r_{m^-}.

Following Fig. 22 the minimum radius of the scanning trajectory is given by the following equation:

$$r_{m^-} = D - d\cos(\alpha_{min}) \tag{12}$$

The position reference can now be calculated by drawing the circle with radius r_{m^-} around $\hat{\boldsymbol{p}}_{\boldsymbol{p0}}$ as follows:

$$\boldsymbol{p_d} = \hat{\boldsymbol{p}}_{\boldsymbol{p0}} + \begin{bmatrix} r_{m^-}\cos(\omega_s t + \pi) \\ r_{m^-}\sin(\omega_s t + \pi) \\ 0 \end{bmatrix} \tag{13}$$

where ω_s is the rotational frequency of the scanning trajectory and t is the time.

In the measurements of $\boldsymbol{p_{h1}}$ and $\boldsymbol{p_{h2}}$, it was observed that the measurement points are distributed nonuniformly around the center of the hole. This can be explained by looking at Fig. 19. Because the measurement trajectory is centered around $\hat{\boldsymbol{p}}_{\boldsymbol{p},0}$ (and not centered around the middle of the hole), the peg tends to stay near the side of $\hat{\boldsymbol{p}}_{\boldsymbol{p},0}$ disproportionally long during the scan of the hole. Therefore, taking the average value of the set $\boldsymbol{P_{h2}}$ will give an estimate for $\boldsymbol{p_{h2}}$ that is biased towards $\hat{\boldsymbol{p}}_{\boldsymbol{p},0}$. To mitigate this, the maximum values recorded in x- and y- direction are recorded, and $\boldsymbol{p_{h2}}$ is estimated by averaging these maxima:

$$\hat{\boldsymbol{p}}_{\boldsymbol{h2}} = \frac{\min\left(\boldsymbol{P_{h2}}\right) + \max\left(\boldsymbol{P_{h2}}\right)}{2} \tag{14}$$

To keep the tip point pointing radially outward and touching the top of the hole as in Fig. 20, the peg can be rotated by a unit quaternion $\boldsymbol{q_{s1}}$. A unit quaternion is defined by a scalar and a vector part: $\boldsymbol{q} = \begin{bmatrix} q_0 & \bar{\boldsymbol{q}} \end{bmatrix}$ and has a norm equal to 1. The unit quaternion is related to the angle-axis representation of an orientation ($\begin{bmatrix} \varphi & \mathbf{e} \end{bmatrix}$) as follows: $\boldsymbol{q} = \begin{bmatrix} q_0 & \bar{\boldsymbol{q}} \end{bmatrix} = \begin{bmatrix} \cos\left(\frac{1}{2}\varphi\right) & \sin\left(\frac{1}{2}\varphi\right)\mathbf{e} \end{bmatrix}$.

Rotation $\boldsymbol{q_{s1}}$ is a rotation relative to $\hat{\boldsymbol{q}}_{\boldsymbol{p}0}$. The angle of this rotation must be at least $2\alpha_{min}$ to ensure the contact between the peg and the hole is as in Fig. 20. The axis of rotation of $\boldsymbol{q_{s1}}$ must be perpendicular to the vector spanned by $(\boldsymbol{p_d} - \hat{\boldsymbol{p}}_{\boldsymbol{p0}})$, and is indicated with $\mathbf{e_d}$ in Fig. 19. To calculate the resulting $\boldsymbol{q_d}$ the quaternion product of $\boldsymbol{q_{s1}}$ with $\hat{\boldsymbol{q}}_{\boldsymbol{p}0}$ is calculated. The quaternion product between two quaternions $\boldsymbol{q_a}$ and $\boldsymbol{q_b}$ is given by [27, Chapter 4.1]:

$$\boldsymbol{q_a} \circ \boldsymbol{q_b} = (q_{a,0}q_{b,0} - \boldsymbol{q_a}^T\boldsymbol{q_b} \quad , \quad q_{a,0}\bar{\boldsymbol{q}}_{\boldsymbol{b}} + q_{b,0}\bar{\boldsymbol{q}}_{\boldsymbol{a}} + \bar{\boldsymbol{q}}_{\boldsymbol{a}} \times \bar{\boldsymbol{q}}_{\boldsymbol{b}}) \tag{15}$$

Following equation (15), $\boldsymbol{q_d}$ can be calculated by:

$$\boldsymbol{q_d} = \hat{\boldsymbol{q}}_{\boldsymbol{p}0} \circ \boldsymbol{q_{s1}} \quad (16) \qquad \text{with:} \quad \begin{aligned} \bar{\boldsymbol{q}}_{\boldsymbol{s1}} &= \sin(\alpha_{min})\mathbf{e_d} \\ q_{s1,0} &= \sqrt{1-|\bar{\boldsymbol{q}}_{\boldsymbol{s1}}|^2} \end{aligned} \quad (17) \qquad \text{with:} \quad \mathbf{e}_{\boldsymbol{d}}^T = \begin{bmatrix} \cos\left(\omega_s t + \frac{1}{2}\pi\right) \\ \sin\left(\omega_s t + \frac{1}{2}\pi\right) \\ 0 \end{bmatrix} \quad (18)$$

where $\mathbf{e_d}$ is the axis of rotation of $\boldsymbol{q_{s1}}$ as illustrated in Fig. 19.

Due to the nonuniform distribution of measurement points, the quaternion average - covered in a later section - of set $\boldsymbol{Q_h}$ will also result in a biased estimate for $\boldsymbol{q_h}$. Therefore, a similar min/max approach is developed for determining $\boldsymbol{q_h}$, which will be explained using an example.

Fig. 23 shows a set of generated orientations. The magenta arrow can be compared to $\boldsymbol{q_h}$. The translucent magenta lines represent the orientations of the peg as it would perform the scan of the hole. The red, green and blue arrows correspond to the peg frame $\boldsymbol{\Psi_p}$. The translucent red, green and blue lines represent $\boldsymbol{\Psi_p}$ during the hole measurement.

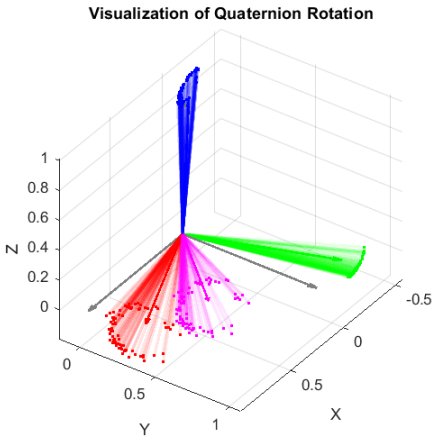

Figure 23: Generated data displaying orientations of $\boldsymbol{\Psi_p}$ as a hole is scanned.

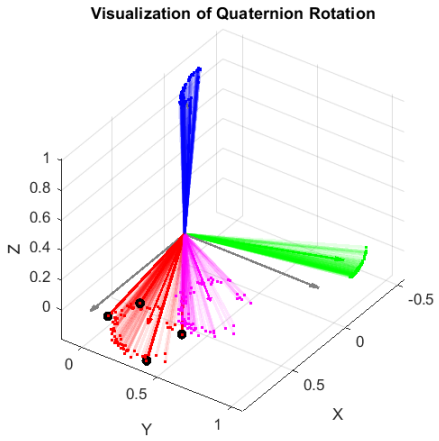

Figure 24: Maximum orientations in basis vector $\mathbf{e_x}$

The min/max approach operates by monitoring the basis vectors of $\boldsymbol{\Psi_p}$. The orientations that result in maxima in the x-, y- and z-directions for each basis vector are stored in the set $\boldsymbol{Q_{h^+}}$, and the quaternion average of $\boldsymbol{Q_{h^+}}$ will be the estimate for $\boldsymbol{q_h}$. The black dots in Fig. 24, 25 and 26 represent the stored maxima of the basis vectors of $\boldsymbol{\Psi_p}$.

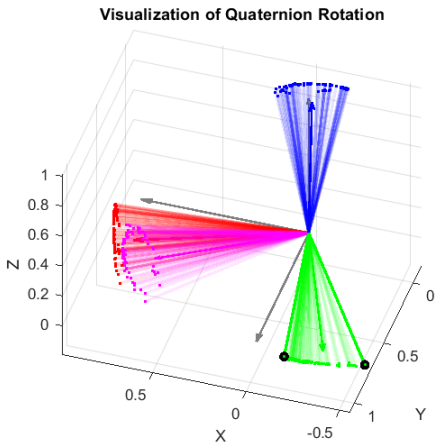

Figure 25: Maximum orientations in basis vector $\mathbf{e_y}$

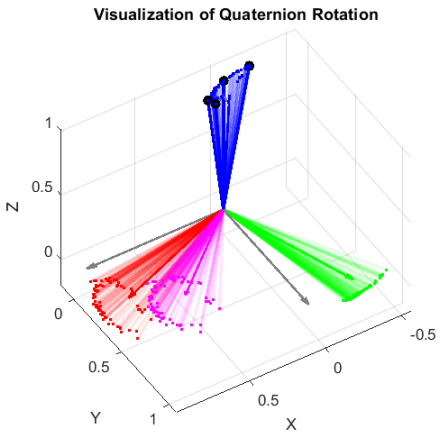

Figure 26: Maximum orientations in basis vector $\mathbf{e_z}$

As a result, 18 quaternions are stored in $\boldsymbol{Q_{h^+}}$: the quaternions corresponding to the minimum and maximum values in the x-, y-, and z-directions for each of the three basis vectors. When the peg makes the circular motion, the basis vectors of $\boldsymbol{\Psi_p}$ draw ellipses. An ellipse has at most 4, and at least 2 unique points for the minima and maxima in x-, y- and z-direction in $\mathbb{R}^3$. For example, the ellipse of $\mathbf{e_x}$ in Fig. 24 has a relatively low eccentricity and shows 4 unique points. The ellipse of $\mathbf{e_y}$ in Fig. 25 has a high eccentricity, which results in 2 unique points in combination with its orientation in $\mathbb{R}^3$.

To calculate the the basis vectors ($\begin{bmatrix}\mathbf{e}_{\boldsymbol{x},q_i} & \mathbf{e}_{\boldsymbol{y},q_i} & \mathbf{e}_{\boldsymbol{z},q_i}\end{bmatrix}$) of an orientation $\boldsymbol{Q_{h_i}}$ in $\boldsymbol{\Psi_G}$, the rotation matrix corresponding to $\boldsymbol{Q_{h_i}}$ ($\boldsymbol{R_{q_i}}$) can be multiplied with one of the unit axes ($\begin{bmatrix}\mathbf{e_x} & \mathbf{e_y} & \mathbf{e_z}\end{bmatrix}$):

$$\mathbf{e}_{\boldsymbol{x},q_i} = \boldsymbol{R_{q_i}}\mathbf{e_x} \quad , \quad \mathbf{e}_{\boldsymbol{y},q_i} = \boldsymbol{R_{q_i}}\mathbf{e_y} \quad , \quad \mathbf{e}_{\boldsymbol{z},q_i} = \boldsymbol{R_{q_i}}\mathbf{e_z} \tag{19}$$

The rotation matrix $\boldsymbol{R}$ corresponding to a unit quaternion $\boldsymbol{q}$ is given by [27, Chapter 4.1]:

$$\boldsymbol{R(q)} = \boldsymbol{\Lambda}\bar{\boldsymbol{\Lambda}}^T \tag{20}$$

where:

$$\boldsymbol{\Lambda} = \begin{bmatrix}-\bar{\boldsymbol{q}} & q_0\boldsymbol{I} + \tilde{\boldsymbol{q}}\end{bmatrix} \tag{21}$$

$$\bar{\boldsymbol{\Lambda}} = \begin{bmatrix}-\bar{\boldsymbol{q}} & q_0\boldsymbol{I} - \tilde{\boldsymbol{q}}\end{bmatrix} \tag{22}$$

where $\tilde{\boldsymbol{q}} \in \mathbb{R}^{3\times3}$ represents the skew-symmetric matrix associated with the vector part of $\boldsymbol{q}$.

The average quaternion $\langle \boldsymbol{q} \rangle$ of a set of n quaternions $\boldsymbol{Q} \in \mathbb{R}^{n\times4}$ can be found by solving the following optimization problem [28]:

$$\langle \boldsymbol{q} \rangle = \arg\max_{\boldsymbol{q}\in\mathbb{S}^3} \boldsymbol{q}^T A \boldsymbol{q} \tag{23}$$

where:

$$A = \boldsymbol{Q}^T\boldsymbol{Q} \tag{24}$$

where $\mathbb{S}^3$ denotes the unit 3-sphere. The solution of the maximization problem in equation (23) is given by the eigenvector of A that corresponds to the maximum eigenvalue of A [28].

Fig. 27 shows how the average quaternions of $\boldsymbol{Q_{h^+}}$ and $\boldsymbol{Q_h}$ compare. The yellow arrows indicate the estimate for $\boldsymbol{q_h}$ based on averaging the complete set of measurement points $\boldsymbol{Q_h}$, whereas the black arrows indicate the estimate for $\boldsymbol{q_h}$ based on averaging the set of maxima $\boldsymbol{Q_{h^+}}$. It can be seen that the estimate of $\boldsymbol{q_h}$ based on $\boldsymbol{Q_{h^+}}$ gives the better estimate.

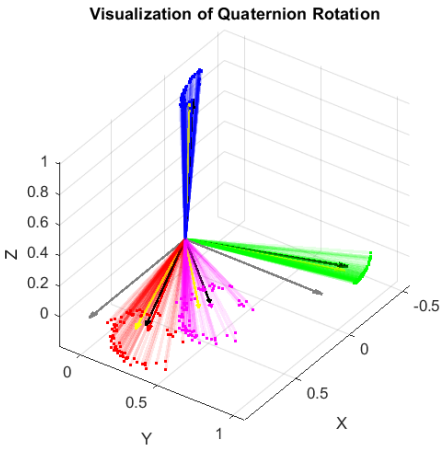

Figure 27: Estimated central orientation in black, compared to the average of the measured set in yellow.

When the scan for $\boldsymbol{p_{h2}}$ and $\boldsymbol{q_h}$ is finished, the orientation of the peg is changed to $\hat{\boldsymbol{q}}_{\boldsymbol{h}}$ and the peg is partially extracted from the hole. The same scanning motion is performed but now the circle of the trajectory is centered around the x and y of $\hat{\boldsymbol{p}}_{\boldsymbol{h2}}$ and the orientation around $\hat{\boldsymbol{q}}_{\boldsymbol{h}}$. The scan results in the set of measurements $\boldsymbol{P_{h1}}$. $\hat{\boldsymbol{p}}_{\boldsymbol{h1}}$ is obtained equivalent to $\hat{\boldsymbol{p}}_{\boldsymbol{h2}}$ in equation (14).

2.2.6 Dancing

For the demonstration of the workspace, a common industrial motion trajectory is selected: the pick-and-place movement. Fig. 28 depicts the dancing trajectory. During the dancing motion $\boldsymbol{q_d}$ is constantly matching $\boldsymbol{q_G}$, and therefore the dancing motion displays a part of the translational workspace of the T-Flex only.

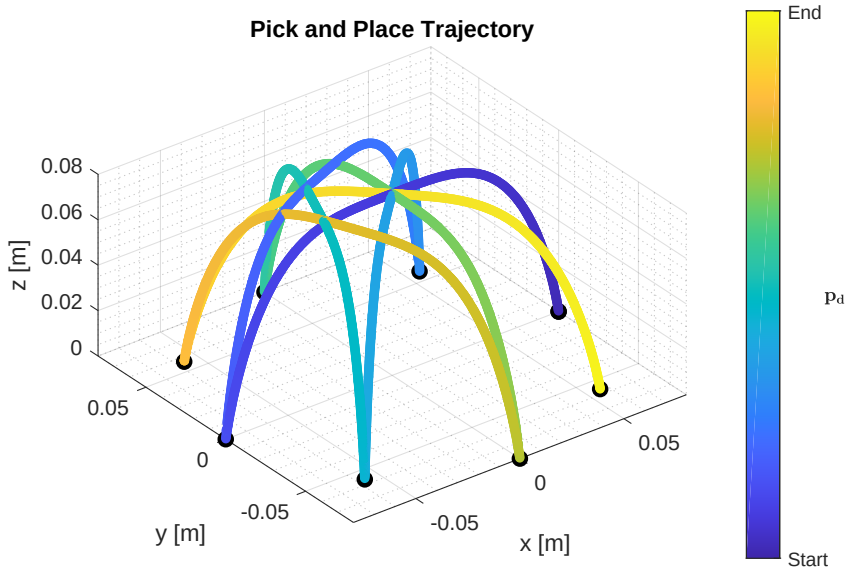

Figure 28: Pick and Place trajectory.

To have a smooth trajectory with limited jerk and acceleration of the manipulator, a 7th order polynomial is selected to generate the point-to-point motions. The trajectory between two points in the xy-plane ($\begin{bmatrix} x1 & y1 \end{bmatrix}^T$ and $\begin{bmatrix} x2 & y2 \end{bmatrix}^T$) is generated as follows [29]:

$$\begin{bmatrix} x_d \\ y_d \end{bmatrix} = \begin{bmatrix} x1 \\ y1 \end{bmatrix} + \left(\begin{bmatrix} x2 \\ y2 \end{bmatrix} - \begin{bmatrix} x1 \\ y1 \end{bmatrix} \right) s(\tau) \quad (25) \qquad \text{where}$$

$$s(\tau) = -20\tau^7 + 70\tau^6 - 84\tau^5 + 35\tau^4 \quad (26)$$

$$\tau = \frac{(t - T1)}{(T2 - T1)} \quad (27)$$

where t is the actual time, and $T1$ and $T2$ denote the starting and ending time of the trajectory respectively.

In the same time that the peg moves from $\begin{bmatrix} x1 & y1 \end{bmatrix}^T$ to $\begin{bmatrix} x2 & y2 \end{bmatrix}^T$, the peg must move up and down again in the z-direction. Therefore the the reference in z-direction is generated as follows:

$$z_d = \begin{cases} z_1 + (z_2 - z_1)s(\tau_+), & \text{if} \quad t < T2 - \frac{1}{2}(T2 - T1) \\ z_2 + (z_1 - z_2)s(\tau_-), & \text{if} \quad t > T2 - \frac{1}{2}(T2 - T1) \end{cases} \quad (28)$$

where

$$\tau_+ = \frac{(t - T1)}{\frac{1}{2}(T2 - T1)} \quad (29) \qquad \tau_- = \frac{(t - T1 - \frac{1}{2}(T2 - T1))}{\frac{1}{2}(T2 - T1)} \quad (30)$$

where z_1 is the lowest height of the trajectory, and z_2 is the highest point of the trajectory. The desired points for the trajectory and the trajectory time will be discussed in chapter 3.

2.2.7 Re-Inserting

To re-insert the peg into the hole, $\hat{\boldsymbol{p}}_{\boldsymbol{h1}}$, $\hat{\boldsymbol{p}}_{\boldsymbol{h2}}$ and $\hat{\boldsymbol{q}}_{\boldsymbol{h}}$ are used. During the insertion, the peg is continuously kept at the orientation $\hat{\boldsymbol{q}}_{\boldsymbol{h}}$. The peg is inserted along the line that is spanned by $\hat{\boldsymbol{p}}_{\boldsymbol{h2}}$ and $\hat{\boldsymbol{p}}_{\boldsymbol{h1}}$. The desired reference position for every height h can be calculated as follows:

$$\boldsymbol{p_d} = \hat{\boldsymbol{p}}_{\boldsymbol{h2}} + \frac{h - \hat{p}_{h2,z}}{\hat{p}_{h1,z} - \hat{p}_{h2,z}} \left(\hat{\boldsymbol{p}}_{\boldsymbol{h1}} - \hat{\boldsymbol{p}}_{\boldsymbol{h2}}\right) \tag{31}$$

By varying h from a height above $\hat{p}_{t,z}$ to $\hat{p}_{h2,z}$, the peg can enter the hole without touching the walls.

2.3 Control Structure

2.3.1 Dynamic model of the T-Flex

In developing the control for the peg-in-hole demonstration, the work done by Seinhorst in [26] is extensively used. Seinhorst developed an adaptive feedforward control (AFFC) algorithm based on an implicit model for equations of motion (EOMs) of the T-Flex. The EOMs derived by Seinhorst are based on the exactly constrained 6-RUS configuration for the T-Flex. In this configuration, every arm of the T-Flex contains a rotational shoulder joint, a universal elbow joint, and a spherical wrist joint. The current configuration of the T-Flex is 6-RSS. As a result, every lower arm of the T-Flex contains an internal DOF. In [1] it is shown that actuator torques do not induce significant forces in the underconstrained DOFs, resulting in small excitations only. Consequently, parasitic motion in the internal DOFs does not result in significant error motions at either the actuators or the end-effector. Therefore, the model developed by Seinhorst can is here used for the 6-RSS configuration.

In the dynamic model for the T-Flex, the rigid body equations of motion are extended to include actuator-induced cogging and hysteresis effects, as well as joint reaction forces due to elastic deformations of the flexure joints. The dynamic equations for the T-Flex as derived by Seinhorst are given by:

$$J_{xa}(\boldsymbol{x})^T \Big(M(\boldsymbol{x})\ddot{\boldsymbol{x}} + \boldsymbol{h}(\boldsymbol{x}, \dot{\boldsymbol{x}}) - \boldsymbol{f}(\boldsymbol{x}) - \boldsymbol{g}(\boldsymbol{x}) \Big) - \boldsymbol{\chi}(\boldsymbol{\theta}, \boldsymbol{z}) = \boldsymbol{\tau}_m + \boldsymbol{\tau}_{ext} \tag{32}$$

where

$$\chi_i(\theta_i, z_i) = c_i z_i + \sum_{j=1}^{9} a_{ij} \cos(j\omega\theta) + b_{ij} \sin(j\omega\theta) \tag{33}$$

with

$$\dot{z}_i = \frac{\dot{\theta}_i}{\sigma} \Big(1 - \text{sign}(\dot{\theta}) z \Big) \tag{34}$$

In equation (32), $\boldsymbol{x} \in \mathbb{R}^{37\times 1}$ represents the generalized coordinates ($\dot{\boldsymbol{x}}$ and $\ddot{\boldsymbol{x}}$ its derivatives with respect to time), $M(\boldsymbol{x}) \in \mathbb{R}^{37\times 37}$ is the inertia matrix, $\boldsymbol{h}(\boldsymbol{x}, \dot{\boldsymbol{x}})$ contains the centrifugal and Coriolis terms, $\boldsymbol{f}(\boldsymbol{x})$ the gravitational forces and $\boldsymbol{g}(\boldsymbol{x})$ contains the joint reaction forces. The Jacobian matrix $J_{xa}(\boldsymbol{x}) \in \mathbb{R}^{37\times 6}$ maps the velocity of the generalized coordinates $\dot{\boldsymbol{x}}$ to actuator velocities $\dot{\boldsymbol{\theta}}$. The vector $\boldsymbol{\tau}_m \in \mathbb{R}^{6\times 1}$ represents the actuator torques, and $\boldsymbol{\tau}_{ext}$ are the torques induced on the actuators resulting from external forces applied to the end-effector.

Vector $\boldsymbol{\chi}(\boldsymbol{\theta}, \boldsymbol{z}) \in \mathbb{R}^{6\times 1}$ represents the cogging and hysteresis torques of the actuators, with $\boldsymbol{\theta}$ being the actuator angles and $\boldsymbol{z}$ is an additional state used in the Dahl hysteresis model of the actuator which behaves following equation (34).

The implicit constraints of the kinematic model derived by Seinhorst are combined in the set of equations:

$$\mathcal{D}(\boldsymbol{x}) = \mathcal{D}(\boldsymbol{\theta}, \boldsymbol{d}) = \boldsymbol{0} \tag{35}$$

where $\boldsymbol{d}$ are the dependent coordinates. Every timestep, $\boldsymbol{\theta}$ is updated by the encoder measurements. The vector of dependent coordinates $\boldsymbol{d}$ is updated after every measurement of $\boldsymbol{\theta}$ by a single step of the Newton-Raphson (NR) procedure as follows [27, Chapter 2.3.5]:

$$\Delta \boldsymbol{d}_i = -\left[\mathcal{D}_d(\boldsymbol{\theta}_i, \boldsymbol{d}_{i-1})\right]^{-1} \mathcal{D}(\boldsymbol{\theta}_i, \boldsymbol{d}_{i-1}) \tag{36}$$

s.t.

$$\boldsymbol{x}_i = \begin{bmatrix} \boldsymbol{\theta}_i \\ \boldsymbol{d}_i \end{bmatrix} = \begin{bmatrix} \boldsymbol{\theta}_i \\ \boldsymbol{d}_{i-1} + \Delta \boldsymbol{d}_i \end{bmatrix} \tag{37}$$

where $\mathcal{D}_d$ contains the partial derivatives of $\mathcal{D}$ with respect to $\boldsymbol{d}$.

With the generalized coordinates calculated, the generalized velocities are obtained as follows:

$$\dot{\boldsymbol{x}} = J_{xa}(\boldsymbol{x})\dot{\boldsymbol{\theta}} \qquad \text{where} \qquad J_{xa}(\boldsymbol{x}) = \begin{bmatrix} \boldsymbol{I} \\ -\left[\mathcal{D}_d(\boldsymbol{x})\right]^{-1}\mathcal{D}_\theta(\boldsymbol{x}) \end{bmatrix} \tag{38}$$

where $J_{xa}(\boldsymbol{x}) \in \mathbb{R}^{37\times 6}$ is a Jacobian matrix, $\mathcal{D}_\theta$ contains the partial derivatives of $\mathcal{D}$ with respect to $\boldsymbol{\theta}$ and $\boldsymbol{I}$ is a 6-by-6 identity matrix.

Finally, the generalized accelerations are calculated as follows:

$$\ddot{\boldsymbol{x}} = J_{xa}(\boldsymbol{x})\ddot{\boldsymbol{\theta}} + \gamma(\boldsymbol{x}, \dot{\boldsymbol{x}}) \qquad \text{where} \qquad \gamma(\boldsymbol{x}, \dot{\boldsymbol{x}}) = \begin{bmatrix} \boldsymbol{0} \\ -\left[\mathcal{D}_d(\boldsymbol{x})\right]^{-1}\sum_{j,k}\frac{^2\mathcal{D}}{x_j x_k}\dot{x}_j\dot{x}_k \end{bmatrix} \tag{39}$$

The solution to the kinematics problem can then be substituted into the parametric functions Seinhorst derived for the components of equation (32) to calculate the corresponding dynamics of the T-Flex. The model parameters can be trained by running Seinhorst's AFFC algorithm with a trajectory that covers the relevant workspace, velocities and accelerations for the desired task. Because the peg is mounted to the T-Flex's end-effector, the parameters had to be re-trained after mounting the peg.

The actuator angles $\boldsymbol{\theta}$, and the end-effector coordinates $\boldsymbol{\Upsilon_E}$ (defining the pose of $\boldsymbol{\Psi_E}$ in Fig. 10) are both part of the set of generalized coordinates, and are given by:

$$\boldsymbol{\theta} = \boldsymbol{x}_{(1:6)} \tag{40}$$

$$\boldsymbol{\Upsilon_E} = \boldsymbol{x}_{(31:37)} \tag{41}$$

The controller - which will be covered in the nex section - requires two additional Jacobian matrices: $J_{ea}(\boldsymbol{x})$, which maps actuator velocities to end-effector velocities, and $J_{xe}(\boldsymbol{x})$, which maps end-effector velocities to generalized velocities. These matrices are defined by the following equations:

$$\dot{\boldsymbol{x}} = J_{xe}(\boldsymbol{x})\begin{bmatrix}\dot{\boldsymbol{p}}_{\boldsymbol{E}} \\ \dot{\boldsymbol{q}}_{\boldsymbol{E}}\end{bmatrix} \tag{42}$$

$$\begin{bmatrix}\dot{\boldsymbol{p}}_{\boldsymbol{E}} \\ \dot{\boldsymbol{q}}_{\boldsymbol{E}}\end{bmatrix} = J_{ea}(\boldsymbol{x})\dot{\boldsymbol{\theta}} \tag{43}$$

where $J_{xe}(\boldsymbol{x}) \in \mathbb{R}^{37\times 6}$ and $J_{ea}(\boldsymbol{x}) \in \mathbb{R}^{6\times 6}$. Matrices $J_{ea}(\boldsymbol{x})$ and $J_{xe}(\boldsymbol{x})$ can be calculated after solving the kinematics. Appendix E covers the derivation of these matrices.

2.3.2 Controller

Controller Overview

The controller implemented on the T-Flex is derived from the controller presented in [13]. Several adaptations have been made to make it more suitable for the T-Flex and the problem at hand. In the following section, the controller for the T-Flex, as well as the similarities and differences with the controller of [13], will be discussed.

Similarly to [13], the controller for the T-Flex is designed to compensate for a part of the internal manipulator dynamics. Alike [13], the gravitational forces are compensated. However, internal friction is not compensated since this is virtually absent. On the other hand, the joint reaction forces and motor cogging/hysteresis are compensated because they can be calculated with the model presented in [26] (see section 2.3.1). Including these compensational terms will improve both tracking and steady-state performance.

The gyroscopic terms are not compensated for since this allows for proof of the system's passivity when given a stationary setpoint as elaborated in Appendix B. Moreover, the gyroscopic terms are typically low due to low velocities. Including compensation for the gyroscopic forces can improve tracking, but will not influence the steady-state performance of the system.

Furthermore, the controller creates a virtual spring-damper at the tip of the peg (see Fig. 29). The control action resulting from the virtual spring is similar to the proportional action in [13].

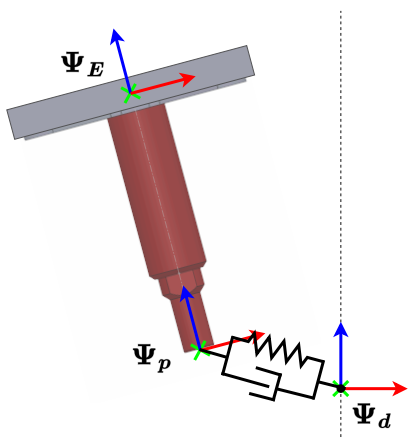

(a) Virtual Cartesian spring-damper acting on Ψ_p.

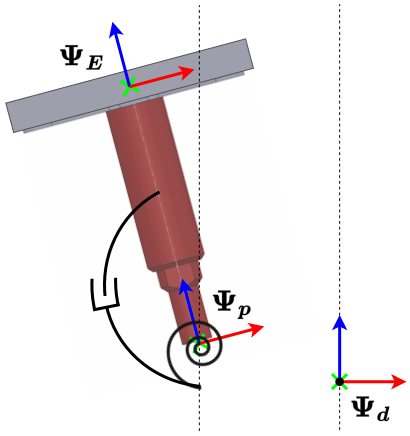

(b) Virtual rotational spring-damper acting on Ψ_p.

Figure 29: Virtual spring-damper system acting on Ψ_p, split into two images for clarity.

While the virtual spring action follows a similar approach to that of Park et al., the implementation of damping differs on two points. First of all, Park et al. apply damping in the joint space (see equation (2)), whereas the damping on the T-Flex is implemented in the cartesian task space. Because Park et al. work with an 8-DOF manipulator, cartesian damping on the end-effector would leave the internal motion in the nullspace undamped. Consequently, the damping must be introduced in the joint space to damp all motions. Since the T-Flex is considered a 6-DOF manipulator, the damping can be introduced in the task space while damping all motions.

Furthermore, Park et al. use absolute damping (see equation (2)), whereas the controller on the T-Flex is designed to provide relative damping. Since both the virtual spring and damper of the T-Flex act on relative errors, the virtual spring and damper can be tuned using a mass-spring-damper approach as discussed in section 3.3. Additionally, relative damping contributes to better reference tracking during the dancing motion.

It must be noted that a relative damping action will generate a force on the peg when it is blocked in its path. Specifically, when the peg is caught in the hole during the searching phase, this damping force acts to extract it. In practice, this does not lead to problems with locating the hole because the contact can be observed before the contribution of the damping force is large enough to extract the peg from the hole.

Finally, in contrast with [13], a pose-dependent feed-forward term regarding the desired accelerations is added. This term is added to have better dynamic performance during the dancing motion.

Mathematical Formulation

The spring, damper, and additional force control input are combined in the vector $\begin{bmatrix} \boldsymbol{f}_m^T & \boldsymbol{m}_m^T \end{bmatrix}^T$. This geometric wrench, which is expressed in the global frame, acts on the peg tip, and is calculated as follows:

$$\begin{bmatrix} \boldsymbol{f}_m \\ \boldsymbol{m}_m \end{bmatrix} = K \begin{bmatrix} \boldsymbol{\Omega}(\boldsymbol{p_d} - \boldsymbol{p_p}) \\ \frac{1}{2}\boldsymbol{E_r}(\boldsymbol{R}^*\boldsymbol{R_d}, \boldsymbol{R_p}) \end{bmatrix} + \begin{bmatrix} \boldsymbol{f}^* \\ \boldsymbol{0} \end{bmatrix} + D \begin{bmatrix} \dot{\boldsymbol{p}}_{\boldsymbol{d}} - \dot{\boldsymbol{p}}_{\boldsymbol{p}} \\ \boldsymbol{\omega_d} - \boldsymbol{\omega_p} \end{bmatrix} \tag{44}$$

where K and D are the full spring and damping matrices. Determining K and D will be covered in section 3, just like the generation of the additional forces $\boldsymbol{f}^*$ and moments due to varying $\boldsymbol{R}^*$. Matrix $\boldsymbol{\Omega}$ is the task-specification matrix as used by Park et al, defined as in equation (4). This matrix varies per insertion step, as will be discussed in section 3. Vector $\boldsymbol{E_r}$ is the rotational error vector as used by Park et al, defined as in equation (8). However, here the vector is multiplied with $\frac{1}{2}$ because of the geometric inconsistency as discussed in Appendix C.

Tensors $\boldsymbol{p_p}$ and $\boldsymbol{R_p}$ can be calculated using $\begin{bmatrix} \boldsymbol{p}_{\boldsymbol{E}}^T & \boldsymbol{q}_{\boldsymbol{E}}^T \end{bmatrix}^T$ (which is part of the output of the Newton-Raphson procedure), under the assumption that $\boldsymbol{\Psi_p}$ and $\boldsymbol{\Psi_E}$ have matching orientations:

$$\boldsymbol{R_p} = \boldsymbol{R_E}(\boldsymbol{q_E}) \tag{45}$$

$$\boldsymbol{p_p} = \boldsymbol{p_E} + \boldsymbol{R_E}\boldsymbol{d}_{\text{peg}} \tag{46}$$

where $\boldsymbol{d_{peg}}$ specifies the origin of $\boldsymbol{\Psi_p}$ expressed in $\boldsymbol{\Psi_E}$. As indicated in Fig. 29, the origin of $\boldsymbol{\Psi_p}$ is projected along the z-direction of $\boldsymbol{\Psi_E}$, such that $\boldsymbol{d}_{\text{peg}} = \begin{bmatrix} 0 & 0 & -\ell_{\text{peg}} \end{bmatrix}$.

The peg-tip velocity $\dot{\boldsymbol{p}}_{\boldsymbol{p}}$ can be obtained by taking the time derivative of equation (46):

$$\dot{\boldsymbol{p}}_{\boldsymbol{p}} = \dot{\boldsymbol{p}}_{\boldsymbol{E}} + \dot{\boldsymbol{R}}_{\boldsymbol{E}}\boldsymbol{d}_{\text{peg}} + \boldsymbol{R}_{\boldsymbol{E}}\dot{\boldsymbol{d}}_{\text{peg}} \quad \Rightarrow \quad \dot{\boldsymbol{p}}_{\boldsymbol{p}} = \dot{\boldsymbol{p}}_{\boldsymbol{E}} + \tilde{\boldsymbol{\omega}}_{\boldsymbol{E}}\boldsymbol{R}_{\boldsymbol{E}}\boldsymbol{d}_{\text{peg}} + 0 \tag{47}$$

where $\tilde{\boldsymbol{\omega}}_{\boldsymbol{E}}$ is the skew-symmetric matrix associated with the angular end-effector rate $\boldsymbol{\omega}_{\boldsymbol{E}}$. The end-effector velocity $\dot{\boldsymbol{p}}_{\boldsymbol{E}}$ can be obtained by equation (43). Obtaining $\boldsymbol{\omega}_{\boldsymbol{E}}$ will be discussed later (see equation (51)).

To be able to map the control wrench $\begin{bmatrix}\boldsymbol{f}_m^T & \boldsymbol{m}_m^T\end{bmatrix}^T$ that acts on $\boldsymbol{\Psi}_{\boldsymbol{p}}$ to the corresponding torques in the actuator space, $\begin{bmatrix}\boldsymbol{f}_m^T & \boldsymbol{m}_m^T\end{bmatrix}^T$ must first be mapped from $\boldsymbol{\Psi}_{\boldsymbol{p}}$ to $\boldsymbol{\Psi}_{\boldsymbol{E}}$. The wrench imposed on the end-effector by $\begin{bmatrix}\boldsymbol{f}_m^T & \boldsymbol{m}_m^T\end{bmatrix}^T$ will be denoted by $\begin{bmatrix}\boldsymbol{f}_c^T & \boldsymbol{m}_c^T\end{bmatrix}^T$. The following equations present the calculation of $\begin{bmatrix}\boldsymbol{f}_c^T & \boldsymbol{m}_c^T\end{bmatrix}^T$. An explanation of its components will be provided below:

$$\begin{bmatrix}\boldsymbol{f}_c \\ \boldsymbol{m}_c\end{bmatrix} = \begin{bmatrix}\boldsymbol{R}_{\boldsymbol{E}} & \boldsymbol{O} \\ \boldsymbol{O} & \boldsymbol{R}_{\boldsymbol{E}}\end{bmatrix} J_{Ep} \begin{bmatrix}\boldsymbol{R}_{\boldsymbol{E}}^T & \boldsymbol{O} \\ \boldsymbol{O} & \boldsymbol{R}_{\boldsymbol{E}}^T\end{bmatrix} \begin{bmatrix}\boldsymbol{f}_m \\ \boldsymbol{m}_m\end{bmatrix} \tag{48}$$

with J_{Ep} defined as:

$$J_{Ep} = \begin{bmatrix}\boldsymbol{I} & \boldsymbol{O} \\ \tilde{\boldsymbol{d}}_{\text{peg}} & \boldsymbol{I}\end{bmatrix} \tag{49}$$

Equation (48) can be interpreted as follows: $\boldsymbol{R}_{\boldsymbol{E}}^T$ (which equals $\boldsymbol{R}_{\boldsymbol{p}}^T$) transforms the globally expressed wrench $\begin{bmatrix}\boldsymbol{f}_m^T & \boldsymbol{m}_m^T\end{bmatrix}^T$ to a wrench expressed in $\boldsymbol{\Psi}_{\boldsymbol{p}}$. The Jacobian matrix J_{Ep} maps the local wrench in $\boldsymbol{\Psi}_{\boldsymbol{p}}$ to a local wrench in $\boldsymbol{\Psi}_{\boldsymbol{E}}$. Finally, $\boldsymbol{R}_{\boldsymbol{E}}$ transforms the locally expressed wrench in $\boldsymbol{\Psi}_{\boldsymbol{E}}$ back to the globally expressed wrench $\begin{bmatrix}\boldsymbol{f}_c^T & \boldsymbol{m}_c^T\end{bmatrix}^T$.

When $\begin{bmatrix}\boldsymbol{f}_c^T & \boldsymbol{m}_c^T\end{bmatrix}^T$ is combined with the terms for the compensation of the internal dynamics and the accelerative feed-forward term, the control for the T-Flex is expressed by:

$$\boldsymbol{\tau}_m = J_{ea,\omega}(\boldsymbol{x})^T \begin{bmatrix}\boldsymbol{f}_c \\ \boldsymbol{m}_c\end{bmatrix} + J_{ea}(\boldsymbol{x})^T \left(J_{xe}(\boldsymbol{x})^T M(\boldsymbol{x}) J_{xe}(\boldsymbol{x}) \begin{bmatrix}\ddot{\boldsymbol{p}}_{d,\boldsymbol{E}} \\ \ddot{\boldsymbol{q}}_{d,\boldsymbol{E}}\end{bmatrix} - J_{xe}(\boldsymbol{x})^T \left(\boldsymbol{f}(\boldsymbol{x}) + \boldsymbol{g}(\boldsymbol{x})\right) \right) - \boldsymbol{\chi}(\boldsymbol{\theta}, \boldsymbol{z}) \tag{50}$$

with the Jacobian $J_{ea,\omega}$ defined by:

$$\begin{bmatrix}\dot{\boldsymbol{p}}_{\boldsymbol{E}} \\ \boldsymbol{\omega}_{\boldsymbol{E}}\end{bmatrix} = J_{ea,\omega}(\boldsymbol{x})\dot{\boldsymbol{\theta}} \tag{51}$$

and the Jacobian J_{ea} defined by:

$$\begin{bmatrix}\dot{\boldsymbol{p}}_{\boldsymbol{E}} \\ \dot{\boldsymbol{q}}_{\boldsymbol{E}}\end{bmatrix} = J_{ea}(\boldsymbol{x})\dot{\boldsymbol{\theta}} \tag{52}$$

where $\boldsymbol{f}(\boldsymbol{x})$, $\boldsymbol{g}(\boldsymbol{x})$ and $\boldsymbol{\chi}(\boldsymbol{\theta}, \boldsymbol{z})$ are the compensational terms for the gravity, elastic joint reaction forces and the cogging plus hysteresis forces respectively. The Jacobian matrix J_{xe}^T maps generalized end-effector forces to generalized forces (see equation (42)), and $\begin{bmatrix}\ddot{\boldsymbol{p}}_{\boldsymbol{d},\boldsymbol{E}}^T & \ddot{\boldsymbol{q}}_{\boldsymbol{d},\boldsymbol{E}}^T\end{bmatrix}^T$ is part of the post-dependent feed-forward term, specifying the desired accelerations of the end-effector. Special attention must be paid to J_{ea} and $J_{ea,\omega}$, as will elaborated on next.

As previously discussed, $\begin{bmatrix}\boldsymbol{f}_{\boldsymbol{c}}^T & \boldsymbol{m}_{\boldsymbol{c}}^T\end{bmatrix}^T$ is a geometric wrench imposed on $\boldsymbol{\Psi}_{\boldsymbol{E}}$. This geometric wrench is dual to the linear and angular velocity of $\boldsymbol{\Psi}_{\boldsymbol{E}}$, and can be mapped to the actuator space using $J_{ea,\omega}$ (see equation (51)). Jacobian matrix J_{ea} (see equation (52)) differs from $J_{ea,\omega}$ in that it maps actuator velocity to *generalized end-effector velocity* instead of *cartesian and angular velocity*. Consequently, J_{ea}^T maps *generalized end-effector forces* to actuator torques, and $J_{ea,\omega}^T$ maps the *geometric end-effector wrench* to actuator torques. Appendix D covers the derivation of J_{ea}, whereas the derivation $J_{ea,\omega}$ is discuscussed in Appendix E.

Since $\boldsymbol{\Psi}_{\boldsymbol{p}}$ and $\boldsymbol{\Psi}_{\boldsymbol{E}}$ have a fixed relative orientation, $\ddot{\boldsymbol{q}}_{\boldsymbol{d},\boldsymbol{E}} = \ddot{\boldsymbol{q}}_{\boldsymbol{d}}$. The desired cartesian accelerations $\ddot{\boldsymbol{p}}_{\boldsymbol{d},\boldsymbol{E}}$ is derived from the reference signal in the following steps:

$$\boldsymbol{p}_{\boldsymbol{d},\boldsymbol{E}} = \boldsymbol{p}_{\boldsymbol{d}} - \boldsymbol{R}_{\boldsymbol{d}}\boldsymbol{d}_{\text{peg}} \tag{53}$$

$$\dot{\boldsymbol{p}}_{\boldsymbol{d},\boldsymbol{E}} = \dot{\boldsymbol{p}}_{\boldsymbol{d}} - \tilde{\boldsymbol{\omega}}_{\boldsymbol{d}}\boldsymbol{R}_{\boldsymbol{d}}\boldsymbol{d}_{\text{peg}} \tag{54}$$

$$\ddot{\boldsymbol{p}}_{\boldsymbol{d},\boldsymbol{E}} = \ddot{\boldsymbol{p}}_{\boldsymbol{d}} - \dot{\tilde{\boldsymbol{\omega}}}_{\boldsymbol{d}}\boldsymbol{R}_{\boldsymbol{d}}\boldsymbol{d}_{\text{peg}} - \tilde{\boldsymbol{\omega}}_{\boldsymbol{d}}\tilde{\boldsymbol{\omega}}_{\boldsymbol{d}}\boldsymbol{R}_{\boldsymbol{d}}\boldsymbol{d}_{\text{peg}} \tag{55}$$

where $\tilde{\boldsymbol{\omega}}_{\boldsymbol{d}}$ is the skew-symmetric matrix associated with the angular rate of the trajectory, and $\dot{\tilde{\boldsymbol{\omega}}}_{\boldsymbol{d}}$ its derivative with respect to time.

The angular rate and angular acceleration of the trajectory can be obtained from the reference signal as follows [27, Chapter 4.1]:

$$\boldsymbol{\omega_d} = 2\Lambda \begin{bmatrix} \dot{q}_{d,0} \\ \dot{\bar{\boldsymbol{q}}}_{\boldsymbol{d}} \end{bmatrix} \tag{56}$$

$$\dot{\boldsymbol{\omega}}_{\boldsymbol{d}} = 2\Lambda \begin{bmatrix} \ddot{q}_{d,0} \\ \ddot{\bar{\boldsymbol{q}}}_{\boldsymbol{d}} \end{bmatrix} \tag{57}$$

where matrix Λ is defined as in equation (21).

The control framework defined in equation (50) can be visually represented in a block diagram as shown in Fig. 30. Fig. 30 also shows a notch filter and a second order low-pass filter, which will be discussed in the following sections.

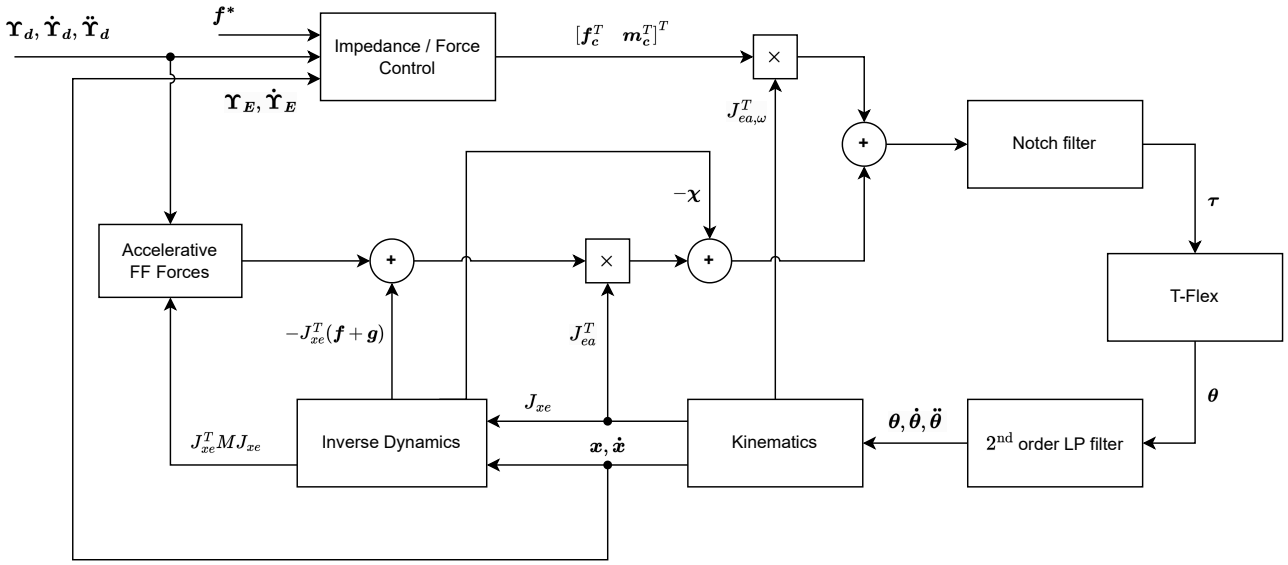

Figure 30: Block diagram of control structure.

2.3.3 Filtering

2.3.3.1 LP Filter

For the NR-scheme to solve for the kinematics of the generalized coordinates $\boldsymbol{x}$, estimates of $\boldsymbol{\theta}$, $\dot{\boldsymbol{\theta}}$ and $\ddot{\boldsymbol{\theta}}$ are required. A second order low-pass (LP) filter is implemented. This filter attenuates high frequency noise in $\boldsymbol{\theta}$, and provides the estimates for $\dot{\boldsymbol{\theta}}$ and $\ddot{\boldsymbol{\theta}}$. The estimates for $\dot{\boldsymbol{\theta}}$ and $\ddot{\boldsymbol{\theta}}$ are also filtered by the same filter as $\boldsymbol{\theta}$. Another important function of the LP filter is to create high frequency rol-off in the feedback control. The implemented controller acts as a PD controller. Without the roll-off provided by the LP filter, the system suffers from amplified high-frequency noise, and increased gain in the frequency region of the parasitic eigenfrequency.

The transfer function of a second order LP filter is given by:

$$\mathcal{H}_{\mathrm{LP}}(s) = \frac{\omega_n^2}{s^2 + 2\zeta\omega_n s + \omega_n^2} \tag{58}$$

where ω_n is the filter's natural frequency, and ζ is the damping ratio.

To obtain estimates for the $\dot{\boldsymbol{\theta}}$ and $\ddot{\boldsymbol{\theta}}$ the filter can be structured as follows:

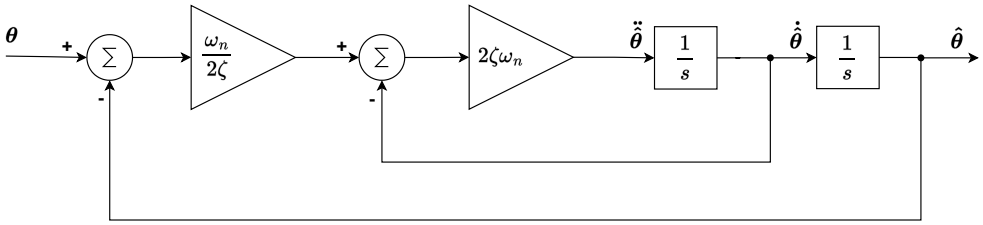

Figure 31: LP filter to obtain $\hat{\boldsymbol{\theta}}$, $\dot{\hat{\boldsymbol{\theta}}}$ and $\ddot{\hat{\boldsymbol{\theta}}}$

where in the implementation in Simulink, the analog integrator blocks are replaced by discrete-time integrators.

The gain crossover frequency ω_c of the LP filter is given by [30]:

$$\omega_c = \omega_n \sqrt{\sqrt{4\zeta^4 + 1} - 2\zeta^2} \tag{59}$$

The filter coefficients will be discussed in section 3.

2.3.3.2 Notch Filter

During the implementation of the controller, it was noticed that even for low stiffnesses (in the order of 300 $\mathrm{N\,m^{-1}}$ for the Cartesian stiffness) oscillations would occur at the critical parasitic eigenfrequency. This is the result of the PD control action applied to the tip. Some of the flexible modes are stabilized and others can be destabilized due to non-minimum phase behavior [27, Chapter 7.2.1]. Even for low feedback gains the vibrational modes can destabilize, because the rate feedback is non-collocated and the damping in the vibrational modes is small.

To suppress the parasitic oscillations, a notch filter is introduced. The notch filter can be applied on several positions in the system; on the feedback signal $\boldsymbol{\theta}$, on the input of the NR-scheme, on the torque signal, or on $\begin{bmatrix}\boldsymbol{f}_m^T & \boldsymbol{m}_m^T\end{bmatrix}^T$. To have minimum interference with the estimation of $\boldsymbol{\theta}$ and the NR-scheme, the notch filter is applied on the torque signal. This way, the filter will have a minimum interference with solving the system's kinematics and inverse dynamics, while still mitigating the parasitic oscillations.

The notch filter implemented is a second-order digital notch filter. The digital transfer function of the notch filter is given by [31]:

$$\mathcal{H}_N(z) = K_n \frac{(z - e^{i\phi_N})(z - e^{-i\phi_N})}{(z - ae^{i\phi_N})(z - ae^{-i\phi_N})} \;\Rightarrow\; K_n \frac{z^2 - 2z\cos(\phi_N) + 1}{z^2 - 2a\cos(\phi_N) + a^2} \tag{60}$$

with:

$$\phi_N = \frac{f_N}{f_s} 2\pi \tag{61}$$

where f_N is the desired notch frequency in Hz, and f_s is the sampling frequency in Hz. a is the radius at which the poles of the filter are placed, and should be placed on the interval $[0, 1]$. A value of a close to 1 yields a sharp notch, while a value of a close to 0 yields a wide notch.

K_n is a scaling factor to normalize the magnitude response at a desired frequency. For the re-insertion, the DC response of the filter is most important. Therefore K_n is determined such that the filter has unit magnitude at 0 Hz ($z = 1$):

$$K_n = \frac{1 - 2a\cos(\phi_N) + a^2}{2 - 2\cos(\phi_N)} \tag{62}$$

The filter is implemented in the direct form 2:

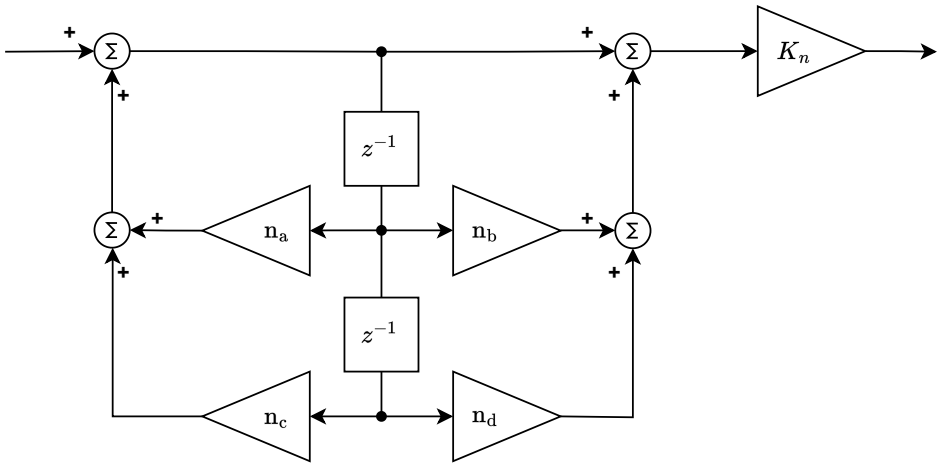

Figure 32: Implementation of $\mathcal{H}_N(z)$ in direct 2 form.

with the filter coefficients:

$$\begin{aligned} \mathrm{n_a} &= 2a\cos(\phi_N) \\ \mathrm{n_b} &= -2\cos(\phi_N) \\ \mathrm{n_c} &= -a^2 \\ \mathrm{n_d} &= 1 \end{aligned} \tag{63}$$

3 Implementation & System-Specific Adaptations

3.1 Control Setup Hardware and Software

The control scheme is implemented in Simulink Real-Time 2018 and is executed on a Speadgoat baseline target pc. The Speadgoat pc has bidirectional EtherCAT communication with the Kollmorgon AKD-P00306 motor drives. The motor drives run in current control mode and form the interface with the Tecnotion QTR-A-133-60-N motors and Heidenhain's LIC 4119 encoders. For more details about the hardware of the T-Flex, please consult [1].

3.2 Filter coefficients

3.2.1 LP Filter Coefficients

The cutoff frequency ω_c of the LP filter has influence on the maximum controller bandwidth. The cutoff frequency of the LP filter is taken to be at least 5 times the bandwidth of the controller, which is slightly more conservative than the rule of thumb of 3 times the controller bandwidth. As will be shown in section 3.3, the controller will be tuned such that the system behaves as a mass-spring-damper system, where the spring and damping forces are provided by the controller. When the stiff controller is implemented, the virtual system is tuned to a natural frequency (f_n) of 9 Hz. To have some extra margin, the 9 Hz is increased to 10 Hz and ω_c is given by:

$$\omega_c = 5 \cdot 2\pi \cdot f_n = 314 \,\mathrm{rad\,s^{-1}} \tag{64}$$

Equation (59) can be rewritten to obtain the filter's natural frequency ω_n:

$$\omega_n = \omega_c(\sqrt{4\zeta^4 + 1} - 2\zeta^2)^{-\frac{1}{2}} \tag{65}$$

The damping ratio is chosen to be $\frac{1}{2}\sqrt{2}$ to have a maximally flat magnitude response. By filling in the numbers, the following filter coefficients are found:

$$\frac{\omega_n}{2\zeta} = 345.16 \tag{66}$$

$$2\zeta\omega_n = 690.32 \tag{67}$$

3.2.2 Notch Filter Coefficients

In [1] it is shown that the first parasitic eigenfrequency of the T-Flex is pose dependent. With the peg installed, the first parasitic eigenfrequency is found to be 63.5 Hz at the center of the workspace. Since it is known that the center of the hole is located somewhere in a radius of 3 cm from the workspace center, the first parasitic eigenfrequency is also evaluated at this radius. At a radius of 3 cm, the first parasitic eigenfrequency is found to be 59.1 Hz. Therefore, the notch frequency ϕ_N is taken to be the average of $(59.1 + 63.5)/2 = 61.3$ Hz. The width of the rejection band is determined by the radius a of the filter poles in the z-plane. Based on empirical tuning, $a = 0.9$ was found to effectively reduce oscillations. The error due to the oscillations is reduced to 2 μm peak-to-peak. Decreasing the pole radius a further does not contribute substantially to the reduction in oscillation magnitude to justify the increased phase lag.

$$\begin{aligned} \mathrm{n_a} &= 1.6677 \\ \mathrm{n_b} &= -1.853 \\ \mathrm{n_c} &= -0.81 \\ \mathrm{n_d} &= 1 \end{aligned} \tag{68}$$

3.3 Control Stiffness and Damping Matrices

3.3.1 Effective Mass at Peg Tip

By determining the natural frequency of the real effective end-effector mass with the virtual spring-damper acting on it, the system's closed-loop bandwidth can be estimated. To evaluate the natural frequency of the closed-loop system, the effective mass at the tip $M_p(\boldsymbol{x})$ is required. A first step in obtaining $M_p(\boldsymbol{x})$ is to obtain the effective mass at the end-effector $M_E(\boldsymbol{x})$. The matrix $M_E(\boldsymbol{x})$ can be derived from the fact that the system's kinetic energy E_{kin} must be equal in both the configuration space and the task space. The kinetic energy of the system is expressed in the configuration space as follows:

$$E_{\text{kin}} = \frac{1}{2}\dot{\boldsymbol{x}}^T M(\boldsymbol{x})\dot{\boldsymbol{x}} \tag{69}$$

where $\dot{\boldsymbol{x}}$ are the velocities of the generalized coordinates, and $M(\boldsymbol{x})$ is the system's mass matrix. Equation (69) can be rewritten to the task space as follows:

$$E_{\text{kin}} = \frac{1}{2}\left[\begin{bmatrix}\dot{\boldsymbol{p}}_{\boldsymbol{E}}\\ \boldsymbol{\omega}_{\boldsymbol{E}}\end{bmatrix}^T J_{xe,\omega}(\boldsymbol{x})^T\right] M(\boldsymbol{x})\left[J_{xe,\omega}(\boldsymbol{x})\begin{bmatrix}\dot{\boldsymbol{p}}_{\boldsymbol{E}}\\ \boldsymbol{\omega}_{\boldsymbol{E}}\end{bmatrix}\right] \tag{70}$$

$$\text{consequently, } M_E \text{ is defined as:} \qquad M_E(\boldsymbol{x}) = J_{xe,\omega}(\boldsymbol{x})^T M(\boldsymbol{x}) J_{xe,\omega}(\boldsymbol{x}) \tag{71}$$

where the Jacobian matrix $J_{xe,\omega}$ maps the end-effectors linear and angular velocities to the generalized velocities. Jacobian matrix $J_{xe,\omega}$ is derived in Appendix D.

To find $M_p(\boldsymbol{x})$ from $M_E(\boldsymbol{x})$, the Jacobian matrix mapping $\begin{bmatrix}\dot{\boldsymbol{p}}_{\boldsymbol{p}}^T & \boldsymbol{\omega}_{\boldsymbol{p}}^T\end{bmatrix}^T$ to $\begin{bmatrix}\dot{\boldsymbol{p}}_{\boldsymbol{E}}^T & \boldsymbol{\omega}_{\boldsymbol{E}}^T\end{bmatrix}^T$ is required. Equation (48) already shows how the forces on the peg tip can be mapped to the end-effector. Following equation (48), $\begin{bmatrix}\dot{\boldsymbol{p}}_{\boldsymbol{p}}^T & \boldsymbol{\omega}_{\boldsymbol{p}}^T\end{bmatrix}^T$ transforms to $\begin{bmatrix}\dot{\boldsymbol{p}}_{\boldsymbol{E}}^T & \boldsymbol{\omega}_{\boldsymbol{E}}^T\end{bmatrix}^T$ as follows:

$$\begin{bmatrix}\dot{\boldsymbol{p}}_{\boldsymbol{E}}\\ \boldsymbol{\omega}_{\boldsymbol{E}}\end{bmatrix} = \begin{bmatrix}\boldsymbol{R}_{\boldsymbol{E}} & \boldsymbol{O}\\ \boldsymbol{O} & \boldsymbol{R}_{\boldsymbol{E}}\end{bmatrix} J_{Ep}^{-T}\begin{bmatrix}\boldsymbol{R}_{\boldsymbol{E}}^T & \boldsymbol{O}\\ \boldsymbol{O} & \boldsymbol{R}_{\boldsymbol{E}}^T\end{bmatrix}\begin{bmatrix}\dot{\boldsymbol{p}}_{\boldsymbol{p}}\\ \boldsymbol{\omega}_{\boldsymbol{p}}\end{bmatrix} \tag{72}$$

In neutral position, $\boldsymbol{R}_{\boldsymbol{E}} = \boldsymbol{I}$, and thus equation (72) simplifies to:

$$\begin{bmatrix}\dot{\boldsymbol{p}}_{\boldsymbol{E}}\\ \boldsymbol{\omega}_{\boldsymbol{E}}\end{bmatrix} = J_{Ep}^{-T}\begin{bmatrix}\dot{\boldsymbol{p}}_{\boldsymbol{p}}\\ \boldsymbol{\omega}_{\boldsymbol{p}}\end{bmatrix} \tag{73}$$

The effective mass at the peg tip can now be found by combining the results of equation (70), (71) and (73):

$$E_{\text{kin}} = \frac{1}{2}\left[\begin{bmatrix}\dot{\boldsymbol{p}}_{\boldsymbol{p}}\\ \boldsymbol{\omega}_{\boldsymbol{p}}\end{bmatrix}^T J_{Ep}^{-1}\right] M_E(\boldsymbol{x})\left[J_{Ep}^{-T}\begin{bmatrix}\dot{\boldsymbol{p}}_{\boldsymbol{p}}\\ \boldsymbol{\omega}_{\boldsymbol{p}}\end{bmatrix}\right] \qquad \Rightarrow \qquad M_p(\boldsymbol{x}) = \left[J_{Ep}^{-1} M_E(\boldsymbol{x}) J_{Ep}^{-T}\right] \tag{74}$$

The stiffness and damping matrices of the controller will be based on the values for $M_p(\boldsymbol{x})$ in its central position in the workspace, denoted simply by M_p. When filling in the numbers for equation (74), M_p is found to be:

$$M_p = \begin{bmatrix} 6.3982 & -0.0037 & -0.0517 & -0.0055 & 1.4797 & -0.0004\\ -0.0037 & 6.4074 & -0.0112 & -1.4945 & -0.0046 & -0.0031\\ -0.0517 & -0.0112 & 7.0082 & 0.0039 & -0.0086 & 0.0100\\ -0.0055 & -1.4945 & 0.0039 & 0.5417 & 0.0013 & -0.0053\\ 1.4797 & -0.0046 & -0.0086 & 0.0013 & 0.5311 & -0.0080\\ -0.0004 & -0.0031 & 0.0100 & -0.0053 & -0.0080 & 0.5966 \end{bmatrix} \tag{75}$$

3.3.2 Calculating the Stiffness Matrix

During the implementation of the controller, it was observed that a diagonal stiffness matrix leads to large variations in the natural frequencies of the system. This can be explained by the strong coupling in M_p: linearly independent restoring forces will induce accelerations in unintended directions due to the coupling of the inertias. Therefore, it is decided to base the stiffness on the desired eigenfrequencies of the system. To do so, a solution to the inverse eigenvalue problem must be obtained. The inverse eigenvalue problem consists of finding the stiffness matrix K based on M_p and the desired eigenfrequencies.

Constructing K involves several constraints on the shape of the matrix that follow from eigenvalue analysis: K should be symmetric and real to yield real eigenvalues and eigenvectors [32, Chapter 8]. Furthermore, by specifying K to be positive definite, the eigenvalues will be positive [32, Chapter 10].

For an undamped system, the homogeneous equation of motion is of the standard form:

$$M_d\ddot{\boldsymbol{x}} + K\boldsymbol{x} = \mathbf{0} \tag{76}$$

To find an expression for K that meets the requirements, a transformation can be applied to the homogeneous equation so that [33]:

$$\boldsymbol{x} = M_d^{-\frac{1}{2}}\boldsymbol{z} \tag{77}$$

such that:

$$\begin{aligned} M_d M_d^{-\frac{1}{2}}\ddot{\boldsymbol{z}} + K M_d^{-\frac{1}{2}}\boldsymbol{z} &= \mathbf{0} \\ M_d^{-\frac{1}{2}} M_d M_d^{-\frac{1}{2}}\ddot{\boldsymbol{z}} + M_d^{-\frac{1}{2}} K M_d^{-\frac{1}{2}}\boldsymbol{z} &= \mathbf{0} \\ \ddot{\boldsymbol{z}} + M_d^{-\frac{1}{2}} K M_d^{-\frac{1}{2}}\boldsymbol{z} &= \mathbf{0} \end{aligned} \tag{78}$$

By applying a coordinate transformation, the eigenvalues of the system do not change. Therefore, the eigenvalues of the system in equation (78) are equal to equation (76). The result of equation (78) is another standard form, with the solution to the homogeneous equation:

$$M_d^{-\frac{1}{2}} K M_d^{-\frac{1}{2}} = \Omega_n^2 \tag{79}$$

where Ω_n^2 is a diagonal matrix with the squared eigenvalues of the system. This equation can be rewritten to find an expression for K:

$$K = M_d^{\frac{1}{2}} \Omega_n^2 M_d^{\frac{1}{2}} \tag{80}$$

By selecting positive and real eigenvalues for Ω_n^2, the product of the matrices will yield a matrix K that is positive definite as required. By selecting 6 distinct eigenvalues (that can be centered around a desired frequency), the system will have 6 orthogonal natural modes. Further determining values used for K will be discussed in section 4.

3.3.3 Calculating the Damping Matrix

The damping matrix of the system is defined by the relation:

$$V^T D V = 2\zeta\Omega_n \tag{81}$$

where ζ is the damping ratio and V is the scaled modal matrix of the system such that:

$$V^T M_p V = \boldsymbol{I} \tag{82}$$

and

$$V^T K V = \Omega_n^2 \tag{83}$$

The damping matrix is then calculated as:

$$D = V^{-T} 2\zeta\Omega_n V^{-1} \tag{84}$$

ζ is taken to be 0.8 to have balanced trade-off between rise time and overshoot.

3.4 Peg and Hole Design

3.4.1 Dimensions and Tolerancing

The peg and hole must be clearly visible as they form the primary components of the demonstration. The length of the peg and height of the tower are selected such that the insertion process is clearly visible for spectators.

The nominal diameter of the peg tip is selected to be 2 cm to strike a balance between spectator visibility and increased mass on the end-effector. The hole is finished with a H7 tolerance ($20.000 - 20.021$ mm). This tolerance can be obtained using a reamer, which makes producing the part cheaper compared to tolerancing it with the CNC machine. An air channel is machined to the bottom of the hole to allow air to escape during peg insertion, preventing the generation of significant damping forces. Fig. 33 shows a technical drawing of the top section of the tower.

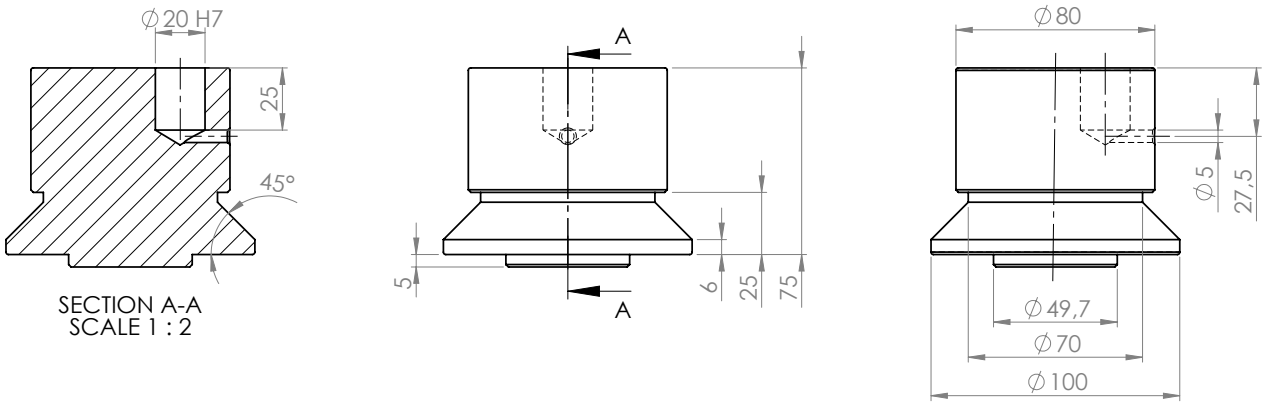

Figure 33: Technical drawing of the tower's top section

To determine the tolerance of the peg tip, the peg tip's steady-state tracking error reconstructed from the actuator positions is used. During preliminary testing (covered in more detail in section 4.3) the tracking error in the xy-plane was found to be $\approx 30\,\mu m$ at maximum, and the error in the z-direction $\approx 100\,\mu m$. To investigate the influence of the error in the z-direction on the error in the xy-plane ($\Delta_{xy}(e_z)$), the error can be projected on the xy-plane as follows:

$$\Delta_{xy}(e_z) = e_z \sin(\theta_{\boldsymbol{t}}) \tag{85}$$

where $\theta_{\boldsymbol{t}}$ is the angle between $\boldsymbol{\Psi_t}$ and $\boldsymbol{\Psi_G}$ and e_z the error in z-direction. To obtain a maximum for $\Delta_{xy}(e_z)$, $\theta_{\boldsymbol{t}}$ is assumed to be 1° at maximum. In practice, it is measured to be less than 1°. When the numbers are filled in into equation (85), e_z does contribute to an error in the xy-plane with $2\,\mu m$ at maximum. This gives a total of $\approx 32\,\mu m$ error in the xy-plane in the task space of the T-Flex.

The T-Flex is currently situated on a cart with supports that can be mounted on the floor. This means that floor vibrations can enter the system and will contribute to the tracking error. In the laboratory environment, these vibrations have a magnitude of approximately $10\,\mu m$. Because the demonstration might be given at places with floor vibrations that are larger, the total desired clearance between the peg and hole is increased to a minimum $50\,\mu m$ ($0.05\,mm$). Therefore, this peg tip is toleranced at $19,94 \pm 0,01 mm$. The total clearance interval is therefore given by $0.05 - 0.09\,mm$.

Because the tracking error of the system depends on the inverse dynamics model, the performance of the system might deteriorate if something in the system changes without an update of the dynamic model's parameters. This can happen if the peg, or another component of the T-Flex, is re-mounted or if the cart is not leveled properly. Therefore, a second peg tip is designed with a smaller nominal diameter and less tight tolerancing to reduce costs. The second tip is toleranced at $19,80 \pm 0,05 mm$, providing a clearance interval of $0.15 - 0.27\,mm$.

The peg tips have an internal M10 thread that can be used to exchange on the peg. Furthermore, the peg tips have a flat side on their top, so that a $22\,mm$ open-end wrench can be used to tighten them. Fig. 34 shows a part of the technical drawings of both pegs, indicating the tolerances.

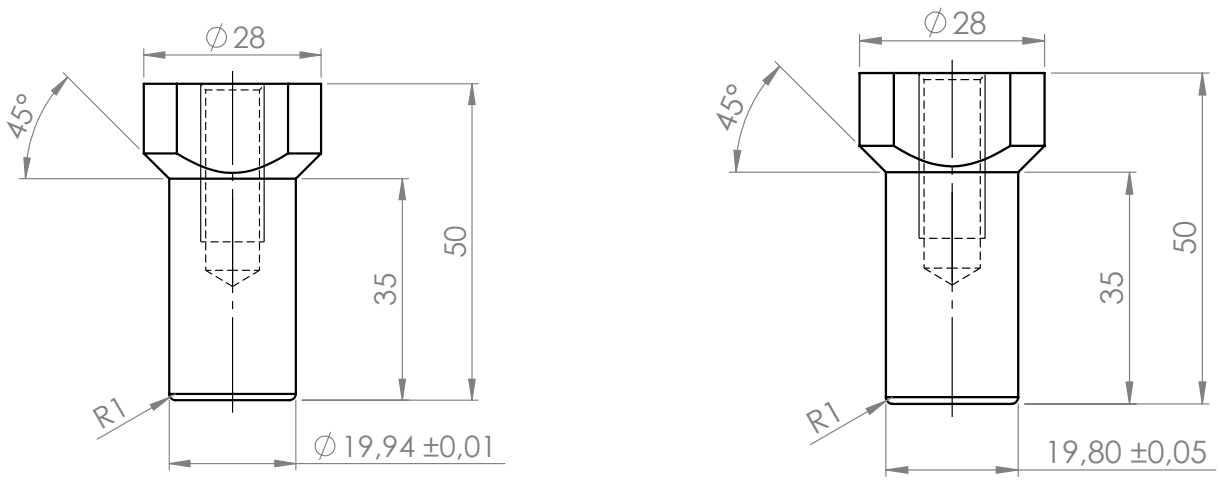

(a) Drawing of peg tip with low clearance.

(b) Drawing of peg tip with large clearance.

Figure 34: Cutout of techincal drawings of both peg tips.

3.4.2 Materials

Peg
The peg is manufactured of aluminium. Aluminum is selected because it can be machined relatively easy, and it keeps the weight of the peg down. The aluminium is anodized red. The red anodization matches the red anodization in the T-Flex's joints and aims to draw the eye of the spectator to the peg. Moreover, anodizing hardens the surface and consequently decreases wear caused by the friction between the peg and the hole.

As mentioned before, the peg tip is connected to the peg's body through a section of stainless steel M10 thread. This is done to ease the swapping of peg tips. The peg's body is hollow to reduce weight further. The peg is connected to the T-Flex through a 3 mm stainless steel plate.

Tower
The tower is also manufactured out of aluminium, and is anodized silver to increase the contrast with the peg. The center of the hole is positioned at a 2 cm radius from the center. The top part of the tower can be rotated with respect to the bottom part to alter the location of the hole. The top is clamped to the bottom part by a DN-100 quick-release clamp, which is typically used to fasten the lid on a reaction vessel.

3.5 Trajectory & Control Parameters

3.5.1 Generation of Additional Forces and Moments

The vector $\boldsymbol{f^*}$ is the force control input used to generate additional forces. In the reaching, searching and inserting states, $\boldsymbol{f^*}$ is nonzero. In these three states, $\boldsymbol{f^*}$ generates a continuous downward force. In these states the exact orientation of the tower is not known yet, and therefore it is assumed that $\boldsymbol{q_t} = \boldsymbol{q_G}$. To generate a downward force, $\boldsymbol{f^*}$ is defined as $\boldsymbol{f}_\mathrm{d}$ similar to the approach in [13]:

$$\boldsymbol{f}_\mathrm{d} = \hat{\boldsymbol{R}}_{\boldsymbol{h}} \begin{bmatrix} 0 \\ 0 \\ -f_\mathrm{d} \end{bmatrix} \tag{86}$$

Since the hole's orientation $\boldsymbol{q_h}$ (which is assumed to match $\boldsymbol{q_t}$) is estimated to align with the global frame, $\hat{\boldsymbol{R}}_{\boldsymbol{h}} = \boldsymbol{I}$ and equation (86) simplifies to:

$$\boldsymbol{f}_\mathrm{d} = \begin{bmatrix} 0 \\ 0 \\ -f_\mathrm{d} \end{bmatrix} \tag{87}$$

The matrix $\boldsymbol{R}^*$ is used in the control framework to generate an additional deviation of the desired orientation $\boldsymbol{R_d}$ (see equations (7) and (44)). When $\boldsymbol{R}^* = \boldsymbol{I}$, the reference $\boldsymbol{R_d}$ is not altered. Except for the inserting state, $\boldsymbol{R}^*$ is always set equal to $\boldsymbol{I}$. In the inserting state, $\boldsymbol{R}^*$ is used to generate the wiggling motion that helps inserting the peg as in Fig. 3c. Due to the wiggling, the friction is overcome and the peg is inserted. $\boldsymbol{R}^*$ during the insertion state is defined as $\boldsymbol{R}_{\text{ins}}$:

$$\boldsymbol{R}_{\text{ins}} = \boldsymbol{R}(\boldsymbol{q}_{\text{ins}}) \quad (88) \quad \text{with:} \quad \begin{aligned} \bar{\boldsymbol{q}}_{\text{ins}} &= \sin(\alpha_{\text{ins}})\mathbf{e_d} \\ q_{\text{ins},0} &= \sqrt{1-|\bar{\boldsymbol{q}}_{\text{ins}}|^2} \end{aligned} \quad (89) \quad \text{with:} \quad \mathbf{e}_{\boldsymbol{d}}^T = \begin{bmatrix} \cos(\omega_{\text{ins}} t) \\ \sin(\omega_{\text{ins}} t) \\ 0 \end{bmatrix} \quad (90)$$

where the angle of rotation α_{ins} is taken to be 1° ($\frac{1}{180}\pi$ rad), and the wiggling frequency of 1 Hz ($\omega_{\text{ins}} = 2\pi\,\text{rad}\,\text{s}^{-1}$). The angle α_{ins} is taken to be $1\,^\circ$ because the error angle between $\boldsymbol{\Psi_t}$ and $\boldsymbol{\Psi_G}$ is established to be less than this, and thus this angle will produce an effective wiggling motion in the hole.

3.5.2 Dancing motion

The dancing motion displays the translational workspace of the T-Flex. In the work of Plettenburgh [6] it is established that a sphere with a radius of 93.8 mm can fit inside the translational workspace when placed at the center of the workspace. To fit the pick-and-place movement inside this sphere, the trajectory is plotted inside the sphere. The trajectory height h_{dance} and radius r_{dance} are increased to the point where the trajectory just fits in the sphere. Trajectory height h_{dance} is eventually set to 8 cm, and $r_{\text{dance}} = 8$ cm. The trajectory is plotted in the sphere in the following figure:

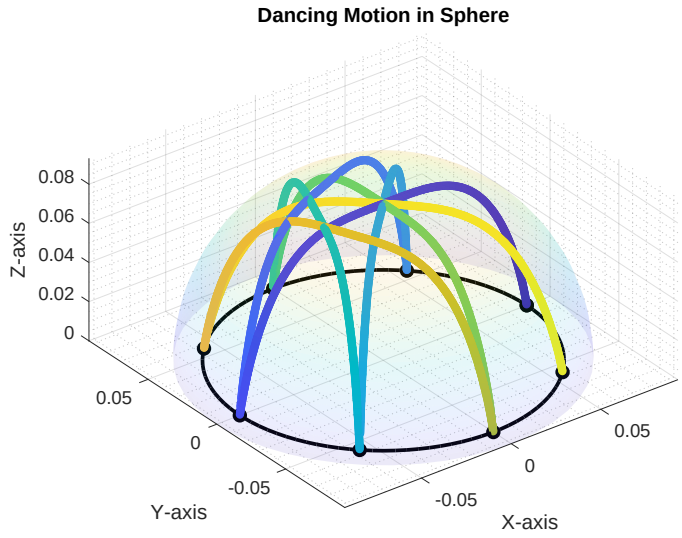

Figure 35: Dancing motion fits within translational workspace.

The maximum motor current is presently limited to 1 A, resulting in a maximum actuator torque of 5.57 N m. In a simulation, the trajectory time is decreased while monitoring the corresponding actuator torques. Eventually, the trajectory time for every pick-place movement is set to 0.6 s, which is expected to require a maximum actuator torque of 5.15 N m. In section 4 the trajectory and the corresponding accelerations and torques will be evaluated.

3.5.3 Parameters per State

To create an overview of all parameter values used in the demonstration, the following table presents the relevant trajectory and controller parameters per state. As mentioned, the controller's stiffness and damping matrices are changed during the demonstration. In section 4 the values for the stiff and the soft controller will be derived.

The parameters per state are:

Parameter	**Reaching**	**Searching**	**Inserting**	**Measuring**	**Dancing**	**Re-Inserting**
K	soft	soft	soft	soft	stiff	stiff
D	soft	soft	soft	soft	stiff	stiff
$\boldsymbol{\Omega}$	diag(1,1,0)	diag(1,1,0)	diag(1,1,0)	$\boldsymbol{I}$	$\boldsymbol{I}$	$\boldsymbol{I}$
$\boldsymbol{f}^*$	$\boldsymbol{f}_\mathrm{d}$	$\boldsymbol{f}_\mathrm{d}$	$\boldsymbol{f}_\mathrm{d}$	0	0	0
$\boldsymbol{R}^*$	$\boldsymbol{I}$	$\boldsymbol{I}$	$\boldsymbol{R}_\mathrm{ins}$	$\boldsymbol{I}$	$\boldsymbol{I}$	$\boldsymbol{I}$
Δ_r	-	1 mm	-	-	-	-
r_{s^-}	-	19 mm	-	-	-	-
r_{s^+}	-	21 mm	-	-	-	-
v_s	-	$0.05\,\mathrm{m\,s^{-1}}$	-	-	-	-
α_{max}	-	4°	-	-	-	-
α_{tilt}	-	3°	-	-	-	-
$\dot{p}_{p,z}$	-	$0.02\,\mathrm{m\,s^{-1}}$	-	-	-	-
d_{insert}	-	-	2.3 cm	-	-	-
α_ins	-	-	1°	-	-	-
r_{m^-}	-	-	-	1 mm	-	-
α_{min}	-	-	-	2°	-	-
h_dance	-	-	-	-	8 cm	-
r_dance	-	-	-	-	8 cm	-
$T2 - T1$	-	-	-	-	0.6 s	-

Table 1: Relevant trajectory and control parameters per state.

4 Experimental Tuning & Validation

4.1 Tuning of Stiffness & Damping Matrices

Soft Controller
During the reaching, searching, inserting and measuring states a controller with a relatively low stiffness is implemented. However, initial testing showed that during the measuring phase, the peg did not properly scan the walls of the hole when the stiffness was too low. Instead of smoothly rotating and contacting the hole's inner surface, the peg would become stuck at one or two points, preventing a full scan of the hole's interior. A corrupted scan during this process will also result in a poor estimate of the hole's pose.

This issue can be attributed to the static friction forces between the peg and the hole. To overcome the static friction, the actuator stiffness is increased. By gradually increasing the stiffness, it was found that a stiffness matrix with the natural frequencies of the virtual system centered around 2 Hz yields a smooth scan of the hole.

The stiffness of the soft controller can now be calculated by filling in equation (80):

$$K_{\text{soft}} = M_p^{\frac{1}{2}} \Omega_n^2 M_p^{\frac{1}{2}} \qquad \text{where} \qquad \Omega_n = (2 \cdot 2\pi)\boldsymbol{I} + \frac{1}{10}\text{diag}(-3, -2, -2, 1, 2, 3) \tag{91}$$

where matrix M_p specifies the effective mass at the peg tip, as specified in equation (75). The diagonal matrix is added in Ω_n to create 6 unique eigenvalues with orthogonal natural modes, as discussed in section 3.3.2.

To estimate the interaction forces between the peg and the hole, errors were monitored during the scanning, inserting, and measuring phases. The results showed that the spring forces did not exceed 6 N and 2 N m, which is within safe limits, ensuring no damage is caused to the setup [13]. Due to the low velocities during these phases, the contribution of accelerative and damping forces to the overall interaction force was minimal. Consequently, these forces were disregarded in the estimation.

Once the stiffness matrix is determined, the system's modal matrix V can be calculated. The system's modal matrix, containing the system's natural modes, is found by solving the eigenvalue problem defined by M_p and K_{soft}. After normalizing the modal matrix to satisfy equation (82), values found for V and Ω_n can be substituted into equation (84) to compute the damping matrix for the soft controller, D_{soft}.

Stiff Controller
Since the controller lacks integral action, the steady-state error depends entirely on the model for the compensation of the static forces and the stiffness of the controller. The compensational forces are calculated with the model developed by Seinhorst. How well this model compensates for static forces in the T-Flex depends on the model parameters. To obtain maximum accuracy, the model parameters should be trained with the peg installed. Moreover, the training trajectory must be sufficiently exciting, covering the relevant workspace, velocities and accelerations for the considered motion.

To establish the maximum controller stiffness, the stiffness is increased gradually, which effectively raises the system's natural frequencies. The stiffness matrix K_{soft} can be scaled by a scalar c, and the corresponding damping matrix D_{soft} with $\sqrt{c}$. The scalar c scales the system's natural frequencies proportionally to the square root of c. Upon increasing c, the oscillations at the critical frequencies are monitored. Eventually, the oscillations begin to grow for the scalar value of $c_{\max} = 40\frac{1}{2}$. To build in a safety margin, the stiffness is reduced by 50 % so that $c = 0.5c_{\max}$. This effectively reduces the magnitude response by ≈ 6 dB. The stiffness and damping matrices for the stiff controller are given by:

$$K_{\text{stiff}} = 0.5c_{\max}K_{\text{soft}} \tag{92}$$

$$D_{\text{stiff}} = \sqrt{0.5c_{\max}}D_{\text{soft}} \tag{93}$$

With this stiffness, natural frequencies for the virtual mass-spring-damper are roughly centered around 9 Hz.

4.2 Tuning of Downward Force

As mentioned in Section 4.1, a minimum stiffness is required for accurate measurement of the hole. This stiffness (K_{soft}) is therefore maintained throughout the reaching, searching, inserting, and measuring phases.

During the reaching, searching and inserting states, the peg exerts a constant downward force. The balance between the downward force and the controller stiffness largely determines how well the peg slides into the top of the hole: too little downward force and the peg easily slips over the hole, too much downward force and the peg can not follow the trajectory accurately. Furthermore, excessive downward force can potentially damage the peg and the hole and is thus to be avoided.

To find a suitable downward force for the insertion, f_d in equation (86) is increased by steps of 0.5 N, starting at 1 N. For a value of $f_d = 4.5\,\text{N}$, the peg is found to slip into the hole consistently.

Increasing the downward force results in higher friction forces between the peg and the scanning surface and consequently a larger tracking error. To check if the resulting error is acceptable, the reference trajectory is compared to the position of the peg tip as reconstructed from the actuator angles. Upon plotting, it can be seen that the error does not exceed 0.5 mm when the peg follows the spiral trajectory. The result is plotted in the following figure:

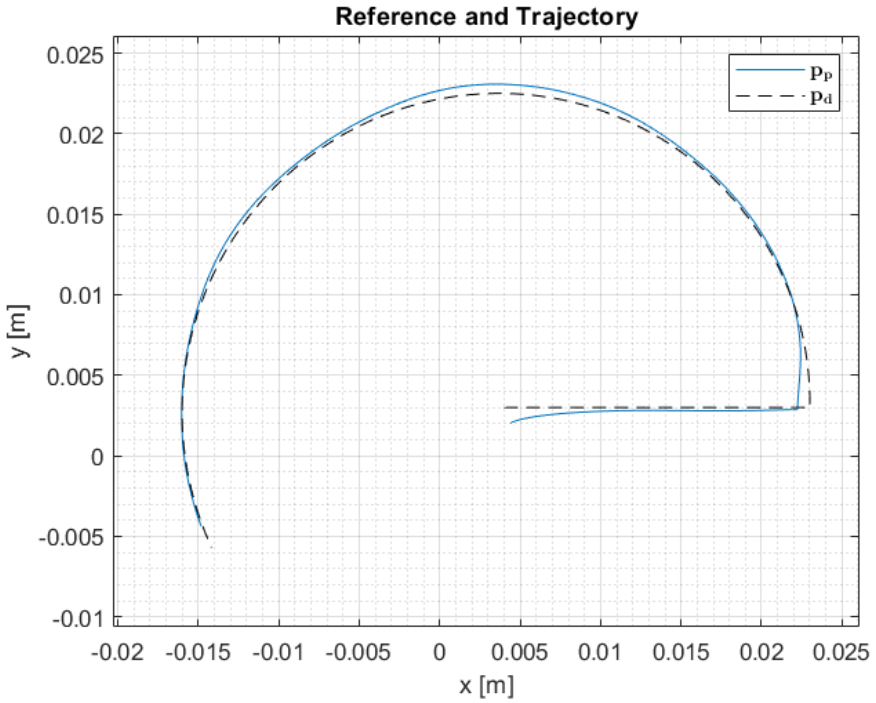

Figure 36: Comparison of reconstructed peg position ($\boldsymbol{p_p}$) with reference $\boldsymbol{p_d}$ during spiral scanning motion.

Fig. 36 shows that a relatively large tracking error occurs when the trajectory shifts from moving radially outward to following the spiral path, leading to some overshoot at the top of the figure. A smoother transition between the outward and spiral movements could potentially reduce this tracking error during the scanning motion.

4.3 Measurements for Peg & Hole Clearance

The minimum tracking error of the system is influenced by both the controller stiffness and the accuracy of the inverse dynamics model. The accuracy of the inverse dynamics model depends on the parameter set that is found for the model. To maximize the accuracy of the estimated parameter set, it must be trained using a sufficiently exciting trajectory with the peg installed, as it would be in the final setup. Obtaining maximum stiffness is discussed in section 4.1.

The minimum tolerances between the peg and the hole follow from the attainable accuracy of the system. To determine the desired tolerances on the peg and the hole, the steady-state tracking errors reconstructed from the actuator angles are investigated. Because these steady-state errors can vary slightly with the position of the peg in the workspace, the steady-state error is investigated at the center of the workspace and at four points at a distance of $r = 3\,\text{cm}$ from the workspace center. The errors were measured at a radius of 3 cm from the center of the task space, since the center of the hole will be positioned somewhere between this radius and the center of the workspace.

The steady-state tracking errors reconstructed from the actuator angles are measured at the following positions: $\begin{bmatrix} r & 0 & 0 \end{bmatrix}^T$, $\begin{bmatrix} 0 & r & 0 \end{bmatrix}^T$, $\begin{bmatrix} -r & 0 & 0 \end{bmatrix}^T$ and $\begin{bmatrix} 0 & -r & 0 \end{bmatrix}^T$. Fig. 37 shows the measured steady-state error for setpoint $\begin{bmatrix} r & 0 & 0 \end{bmatrix}^T$. Upon analyzing the measurements of all four positions, it is found that the error in z-direction is always the largest, with a maximum of $\approx 100\,\mu\text{m}$ RMS. The RMS error in the xy-plane does not exceed $\approx 30\,\mu\text{m}$.

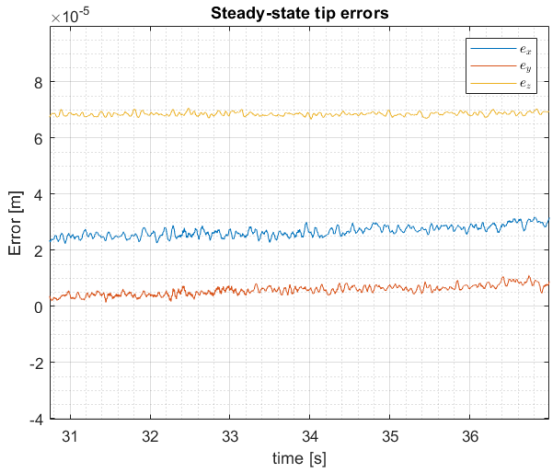

Figure 37: Steady-state tip errors for $\begin{bmatrix} r & 0 & 0 \end{bmatrix}^T$.

4.3.1 Validating Insertion Recognition

In the searching state, the partial insertion of the peg into the hole is recognized by monitoring the tip's z-velocity, reconstructed from the encoder readings. To ensure that the software correctly detects partial insertion at different hole positions, the top section of the tower was rotated around its longitudinal axis with increments of 1/4 rad. The robot successfully detected the partial insertion at all 8 positions tested. Fig. 43 illustrates the approximate locations during these verification experiments. The colors of the dots are not relevant for this context and will be addressed in a later section.

Fig. 38 shows the tip velocities that correspond to the trajectory plotted in Fig. 36. Between 19 and 20 s, the peg is moved outward along the x-axis. From 20 to 22.1 s, the peg is searching for the hole, and at 22.1 s the hole is recognized. As mentioned in section 4.2, the tracking error during searching could be further improved by having a smoother transition at 20 s.

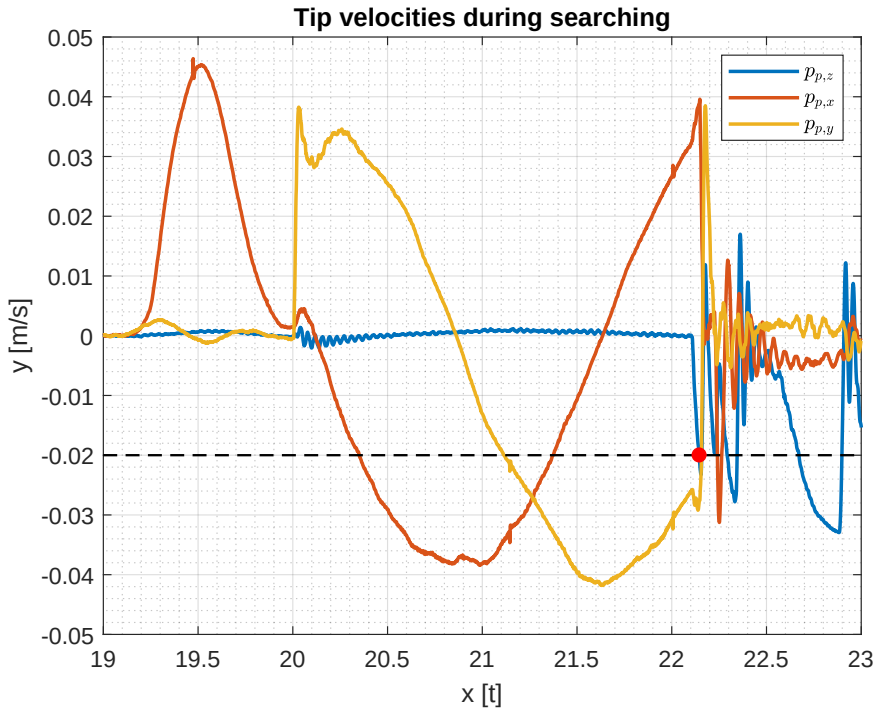

Figure 38: Reconstructed tip-velocities during searching. Dashed black line is the threshold of $-0.02\,\mathrm{m\,s^{-1}}$, and the red dot indicates the recognition of partial insertion. A sharp peak in z-velocity is observed when the peg slips into the hole.

4.3.2 Validating Hole Measurement

To see if the measurement of the hole yields a reproducible estimate of the hole position, the measurement procedure is performed 5 times without moving the hole. The measurements are performed with the low-clearance peg tip installed.

The measurement data of one of these measurements is plotted in the following figures:

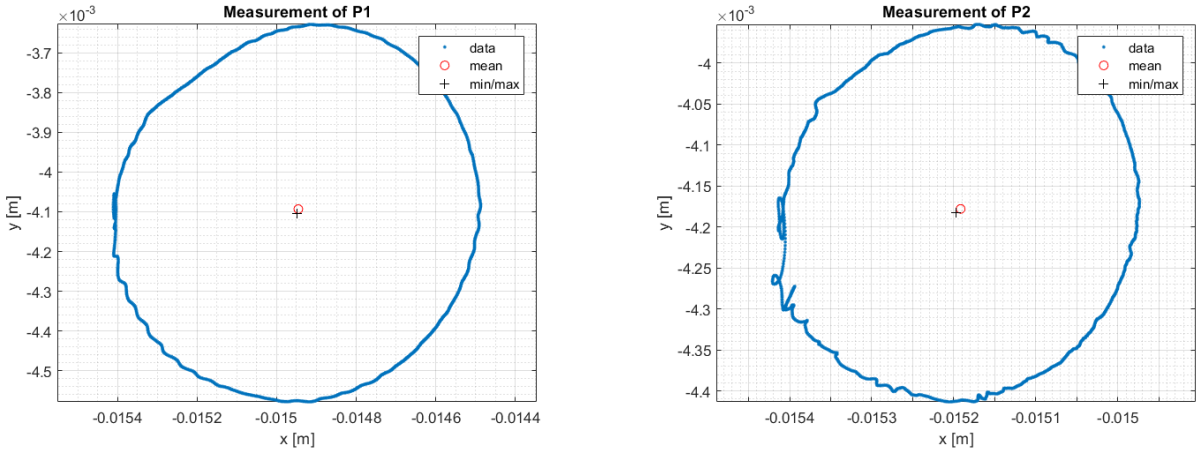

(a) Measurement of $\boldsymbol{p_{h1}}$.

(b) Measurement of $\boldsymbol{p_{h2}}$.

Figure 39: Plot of estimated peg tip position during measurement of $\boldsymbol{p_{h1}}$ and $\boldsymbol{p_{h2}}$.

The results of the measurements are represented in the tables below:

Measurement No.	x (mm)	y (mm)	z (mm)
1	-7.481	-14.596	66.936
2	-7.481	-14.593	66.945
3	-7.481	-14.592	66.933
4	-7.481	-14.594	66.925
5	-7.477	-14.596	66.930
$\boldsymbol{\Delta}_{max}$	4 µm	3 µm	20 µm

Table 2: Measurement Data for $\boldsymbol{p_{h1}}$

Measurement No.	x (mm)	y (mm)	z (mm)
1	-7.669	-14.655	50.461
2	-7.668	-14.655	50.462
3	-7.670	-14.654	50.461
4	-7.669	-14.654	50.461
5	-7.667	-14.655	50.461
$\boldsymbol{\Delta}_{max}$	3 µm	1 µm	1 µm

Table 3: Measurement Data for $\boldsymbol{p_{h2}}$

As can be seen in the tables, the measurements generate reproducible estimates for the points inside the hole.

For the measurement of $\boldsymbol{p_{h2}}$ it can be seen that the diameter of the trajectory is roughly 0.45 mm. This estimated diameter will be denoted with $\hat{d}_{\mathrm{d}}$. The value of 0.45 mm must be incorrect, because the clearance between the large peg and the hole is at most 0.09 mm as discussed in section 3.4. Since $\hat{d}_{\mathrm{d}}$ is larger than the clearance of the peg and the hole, the length of the peg ℓ_{peg} must be overestimated. However, this does not lead to problems for re-inserting as will be discussed later. First the error in ℓ_{peg} will be calculated.

If $\boldsymbol{\Psi_t}$ and $\boldsymbol{\Psi_G}$ align perfectly, the errors in the estimated peg position $\hat{\boldsymbol{p}}_{\boldsymbol{p}}$ should cancel out when estimating $\boldsymbol{p}_{h2}$. But when $\boldsymbol{\Psi_t}$ and $\boldsymbol{\Psi_G}$ have a relative rotation $\theta_t \neq 0$, the error in $\hat{\boldsymbol{p}}_{\boldsymbol{p}}$ will generate a bias in $\boldsymbol{p}_{h2}$ as shown in Fig. 40a:

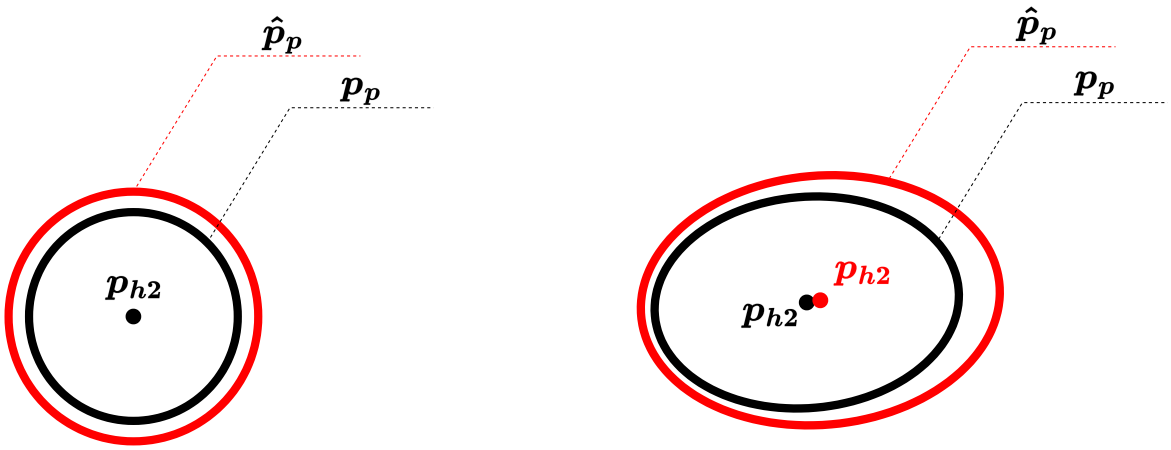

(a) Top view of hole measurement with Ψ_t and Ψ_G aligned.

(b) Top view of hole measurement with Ψ_t and Ψ_G misaligned by θ_t.

Figure 40: Contribution of error in ℓ_{peg} to error in estimation of p_{h2}.

To find the error in peg length $\Delta\ell_{\text{peg}}$, the difference between the diameter that is measured during the scan $\hat{d}_{\text{d}}$ can be compared to the diameter that can be calculated from the tolerances d_{d}. The maximum diameter for d_d that follows from the tolerances can be calculated with the equation that is previously introduced for r_{m^-} in equation (12):

$$d_d = r_{m^-} = D - d\cos(\alpha_{min}) \tag{94}$$

where D is the hole's diameter and d is the peg's diameter. Angle α_{min} can be calculated from equation (11), by filling in the insertion depth of $h = 2.3\,\text{cm}$ and the minimum and maximum values for D and d. Angle $\alpha_{min} \approx 2.1\,\text{mrad}$ at minimum and $\alpha_{min} \approx 3.8\,\text{mrad}$ at maximum. With these values known, equation (94) can be evaluated to find that $d_d \approx 0.05\,\text{mm}$ at minimum and $d_d \approx 0.09\,\text{mm}$ at maximum.

To find the contribution of $\Delta\ell_{\text{peg}}$ to the measured scan diameter $\hat{d}_d$, the following figure shows how the extension of the peg length contributes to a larger radius projected on the xy-plane when the angle between Ψ_G and Ψ_t is θ_t:

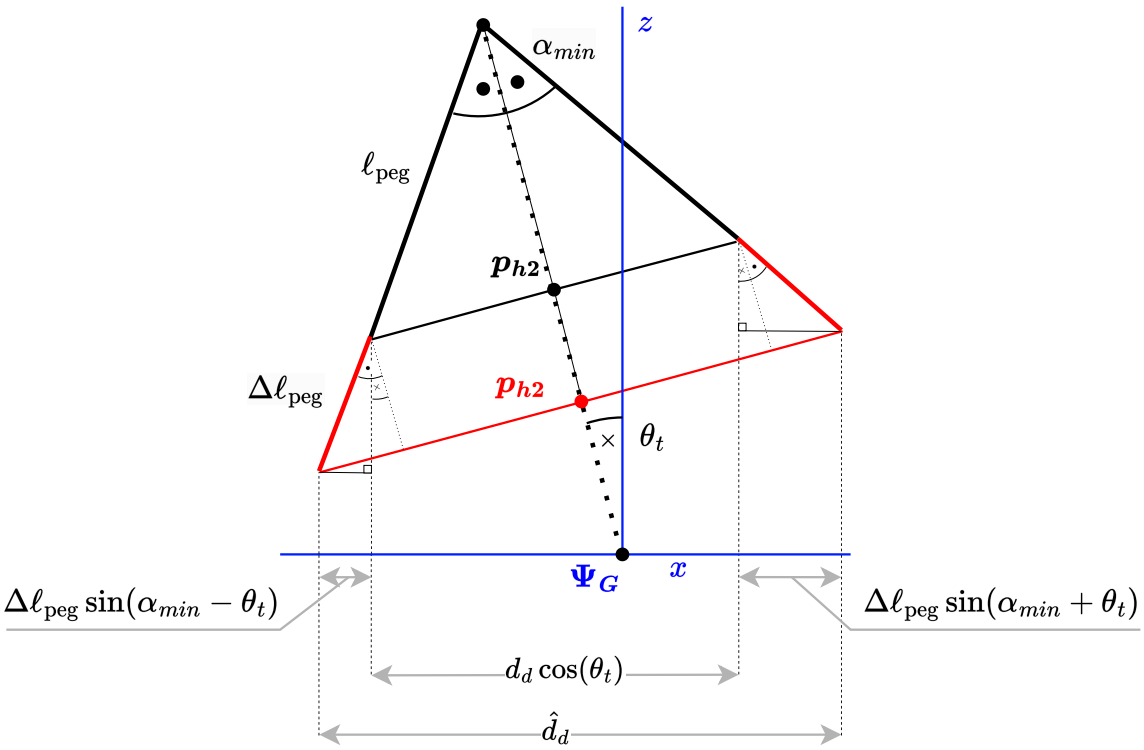

Figure 41: Contribution of $\Delta\ell_{\text{peg}}$ to diameter of hole scan.

From Fig. 41 it can be seen how $\Delta\ell_{\text{peg}}$ is related to $\hat{d}_d$, d_d, α_{min} and θ_t:

$$\left(\hat{d}_d - d_d\cos(\theta_t)\right) = \Delta\ell_{\text{peg}}\left(\sin(\alpha_{min}+\theta_t) + \sin(\alpha_{min}-\theta_t)\right) \tag{95}$$

During the measurement, the orientation of the hole measured, denoted by $\boldsymbol{q_h}$. The angle between $\boldsymbol{q_h}$ and $\boldsymbol{q_G}$ is taken as the estimate for θ_t, and is found to equal 0.0088 rad (or 0.5°). The error in estimated peg lentgth, $\Delta\ell_{\text{peg}}$, can then be found by rewriting equation (95):

$$\Delta\ell_{\text{peg}} = \frac{\left(\hat{d}_d - d_d\cos(\theta_t)\right)}{\left(\sin(\alpha_{min}+\theta_t) + \sin(\alpha_{min}-\theta_t)\right)} \tag{96}$$

Because the angles α_{min} and θ_t are small, this equation can be simplified to:

$$\Delta\ell_{\text{peg}} = \frac{1}{2}\frac{\left(\hat{d}_d - d_d\right)}{\alpha_{min}} \tag{97}$$

where $\hat{d}_d$ is obtained by the measurement, d_d follows from the peg and hole's geometries and θ_t is estimated based on the measurement. When the minimum and maximum values for d_d and α_{min} are filled in, it is found that $\Delta\ell_{\text{peg}}$ has a value ranging from 5.2 – 8.6 cm.

Although the peg is estimated to be longer by $\Delta\ell_{\text{peg}}$, this does not cause any issues during re-insertion. The estimated contact location of p_{h2} lies below the actual point p_{h2}, but since both points are located along the centerline of the hole, the alignment is maintained. Because the peg is re-inserted along the line spanned by the estimates for $\boldsymbol{p_{h1}}$ and $\boldsymbol{p_{h2}}$, the peg will enter the hole along its centerline. This will be illustrated in the following figure. As a result, the re-insertion process proceeds without any complications from the length estimation error.

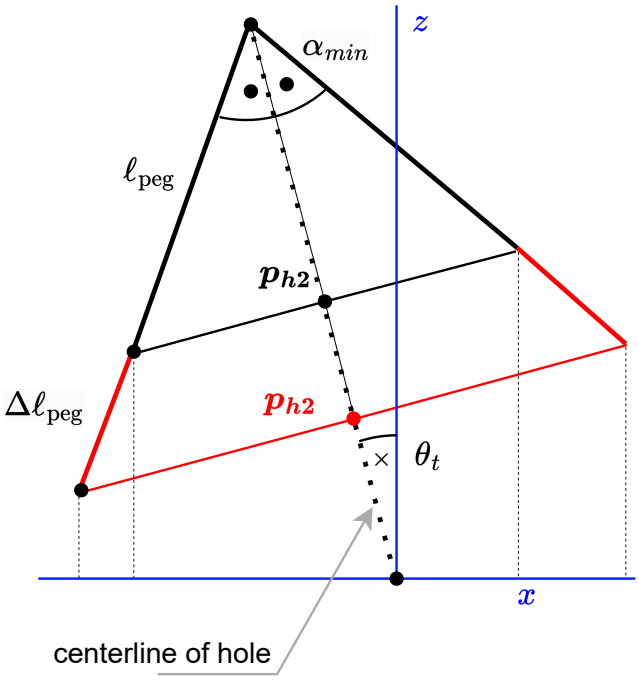

Figure 42: Estimate of $\boldsymbol{p_{h2}}$ projected along centerline of the hole.

4.3.3 Validating Re-Insertion

To validate whether the peg can be re-inserted into the hole without making contact, the demonstration procedure was performed at eight different positions. The top section of the tower was rotated around its longitudinal axis in increments of $\frac{1}{4}$rad. The testing points are shown in the following figure, where green dots indicate contactless re-insertion and red dots indicate insertion with some contact. It was observed that the peg was successfully re-inserted in all tested cases, but not always without touching the hole.

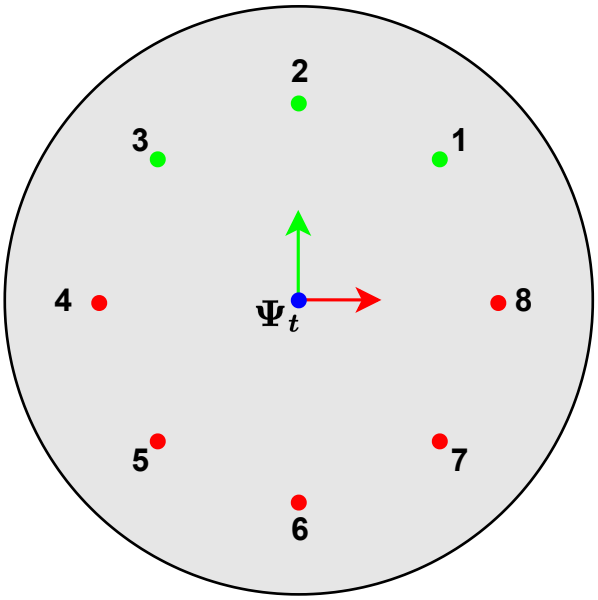

Figure 43: Top view of tower, with appproximate hole locations for validating re-insertion step.

To determine whether the peg is re-inserted into the hole without making contact, the translational error signals are analyzed. If the peg touches the hole, a sharp spike can be observed. The following figures show the tracking errors while re-inserting at position 1 and at position 5:

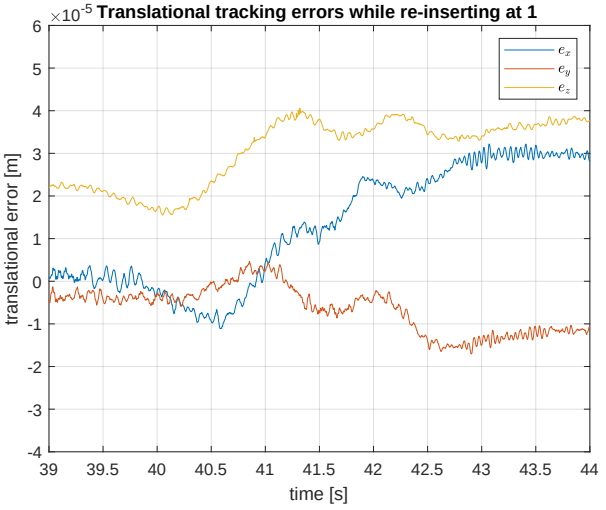

(a) Translational tracking errors while re-inserting at location 1 without touching.

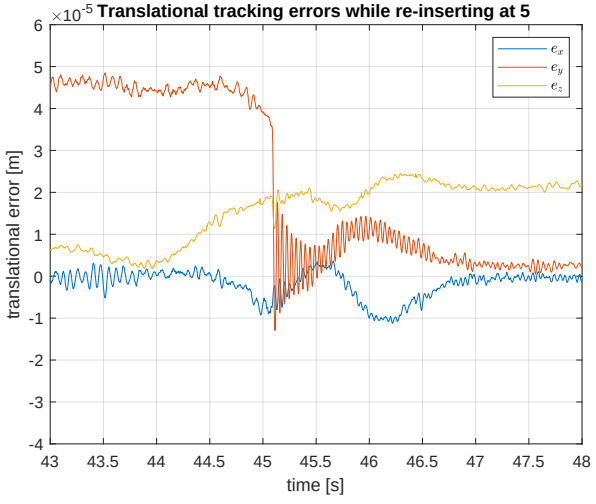

(b) Translational tracking errors while re-inserting at location 5 with touching.

Figure 44: Comparison of re-insertion with and without touching the hole.

At positions 4 – 8, the peg makes contact with the hole during re-insertion. The tracking error signals at positions 4 and 6–8 exhibit behavior similar to the signal shown in Fig. 44b, characterized by a sudden jump in the error signal when the peg contacts the hole, reducing the tracking error in the x- and y-directions. The reduction in tracking error upon contact suggests that the method used to estimate $\boldsymbol{p_{h1}}$, $\boldsymbol{p_{h2}}$, and $\boldsymbol{q_d}$ for re-inserting the peg provides accurate estimates for the hole's centerline and orientation. Therefore, touching the hole during re-insertion is mainly attributed to the control system's tracking error.

To assess the steady-state tracking errors as reconstructed from the actuator angles, the experiment of section 4.3 is repeated with the final setup. The steady-state tracking errors reconstructed from the actuator angles are measured at the following positions: $\begin{bmatrix} r & 0 & 0 \end{bmatrix}^T$, $\begin{bmatrix} 0 & r & 0 \end{bmatrix}^T$, $\begin{bmatrix} -r & 0 & 0 \end{bmatrix}^T$ and $\begin{bmatrix} 0 & -r & 0 \end{bmatrix}^T$, where $r = 3\,\text{cm}$. For every position, the RMS error in the xy-plane is calculated.

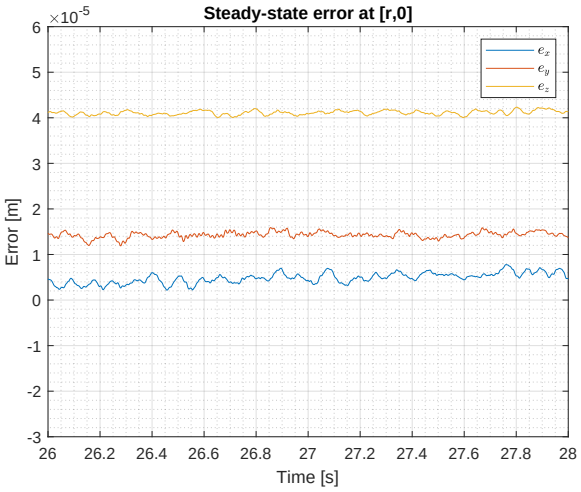

(a) Steady-state error at $\begin{bmatrix} r & 0 & 0 \end{bmatrix}^T$, xy-error $\approx 15\,\mu\text{m}$.

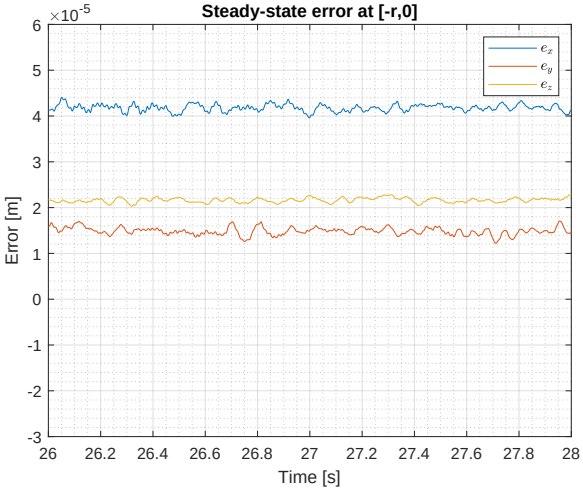

(b) Steady-state error at $\begin{bmatrix} -r & 0 & 0 \end{bmatrix}^T$, xy-error $\approx 45\,\mu\text{m}$.

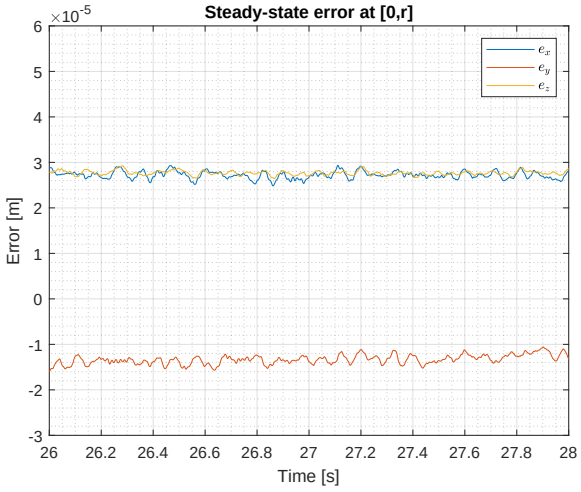

(c) Steady-state error at $\begin{bmatrix} 0 & r & 0 \end{bmatrix}^T$, xy-error $\approx 30\,\mu\text{m}$.

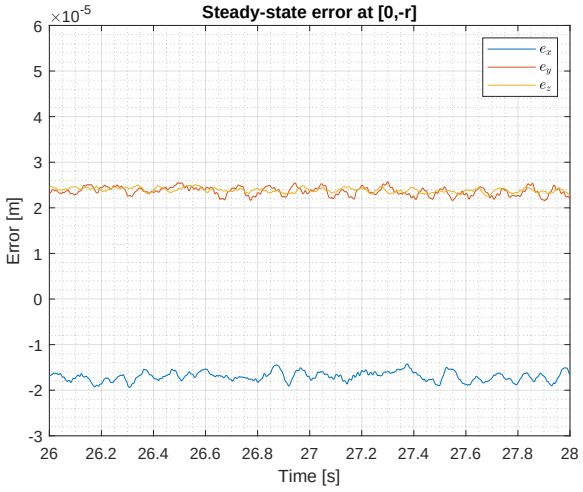

(d) Steady-state error at $\begin{bmatrix} 0 & -r & 0 \end{bmatrix}^T$, xy-error $\approx 30\,\mu\text{m}$.

Figure 45: Steady-state tracking errors reconstructed from actuator angles at points 8, 2, 4 and 6 of Fig. 43.

The maximum steady-state tracking error is found to be 45 µm, which is significantly larger than the 30 µm recorded in the preliminary experiment discussed in section 4.3. Figure 44b shows that the tracking error increases further during the re-insertion motion, indicating that contact with the hole is - in some cases - inevitable with the current controller. The system could benefit from introducing an integrator in the stiff modus to reduce the tracking error, as will be discussed further in the recommendations.

To obtain an estimate of the additional force on the end-effector required to achieve zero steady-state tracking error, the errors measured in Fig. 45 are multiplied with the stiffness matrix K_{stiff}. The norm of the additional forces required for zero steady-state tracking error, based on the measurements in Fig. 45, ranges from 0.6 N to 1 N.

4.3.4 Validating Maximum Motor Torque during Dancing

To ensure that the controller does not demand torque beyond the presently implemented torque limits of the actuators, the motor torques were measured during the execution of the dancing motion. The results are presented in the following figure:

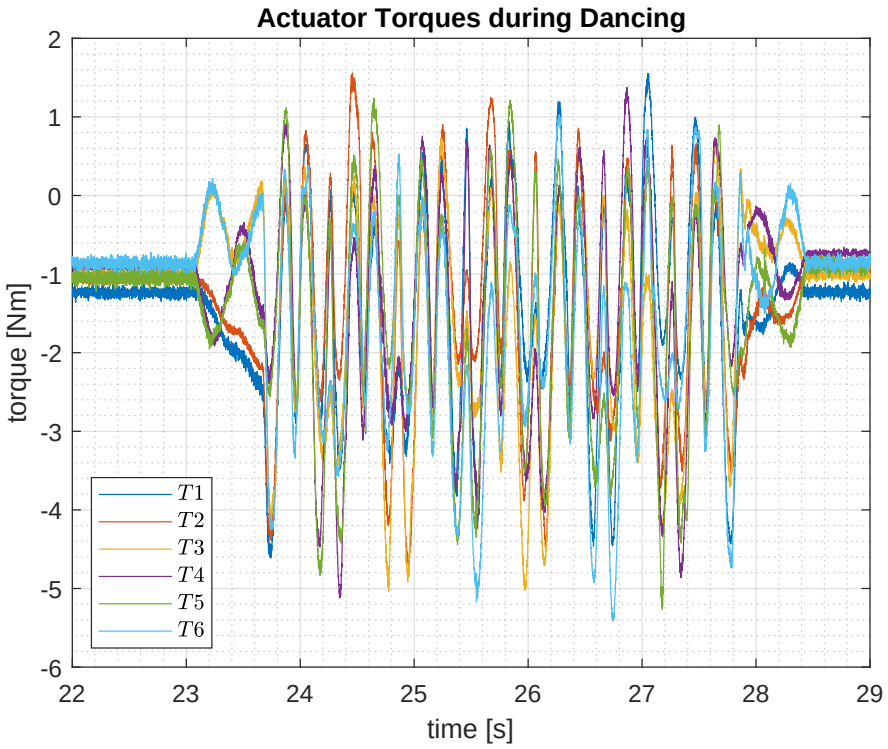

Figure 46: Actuator torques measured during dancing motion.

A maximum torque magnitude of 5.4 N m is measured, which is within the presently implemented torque limit of 5.57 N m. For dancing motion, the velocities in x-, y- and z-direction vary between $5\,\mathrm{m\,s^{-1}}$ and $-5\,\mathrm{m\,s^{-1}}$. The highest accelerations occur in the z-directions, at $\pm 6\,\mathrm{m\,s^{-2}}$. The accelerations in the x- and y-directions range between $3.5\,\mathrm{m\,s^{-2}}$ and $-3.5\,\mathrm{m\,s^{-2}}$.

5 Conclusions

The primary goal of this thesis was to create a peg-in-hole demonstration suitable for showcasing the T-Flex's capabilities. The compliance-based peg-in-hole strategy presented by Park et al. in [13] was selected as the basis for the task and is successfully adapted for implementation on the T-Flex. The hole is consistently located, measured and re-entered, with an appealing demonstration of the translational workspace in between.

The peg and hole have been designed based on the attainable accuracy of the system. Two versions of the peg tip were manufactured, which can be conveniently exchanged by an open-end spanner. The tip with the tight tolerance offers a clearance interval with the hole of $0.05 - 0.09\,\text{mm}$, and can be used in combination with a well-trained parameter set. The peg with the smaller radius offers $0.15 - 0.27\,\text{mm}$ clearance, suitable for situations when the parameter set is expected to be suboptimal, for example after moving the cart the T-Flex is situated on.

To demonstrate that the peg motion is not pre-programmed, the top section of the tower can rotate. A quick-release clamp is used to make rotating the hole convenient.

To locate the hole, a searching trajectory is developed that is based on the geometric properties of the setup. The approach is based on the assumption that the peg can slip into the top of the hole under the tilting angle α_{tilt} of the searching trajectory.

A measurement procedure was developed to scan the inside of the hole. The data collected during the scan is processed in an algorithm to determine the peg orientation central to the hole, and to determine a centerline along which to re-insert the peg. The maximum deviation observed across all measurements is $4\,\mu\text{m}$ in the x-direction, $3\,\mu\text{m}$ in the y-direction, and $20\,\mu\text{m}$ in the z-direction for $\boldsymbol{p_{h1}}$, with similarly small deviations for $\boldsymbol{p_{h2}}$. These values indicate a high reproducibility of the measurement procedure.

In between insertion and re-insertion of the peg, the translational workspace of the T-Flex is displayed by means of a pick-and-place trajectory. The trajectory time is reduced so that the maximum torque ocurring during the motion is $5.4\,\text{N m}$, for which the T-Flex exhibits a maximum z-acceleration of $6\,\text{m s}^{-2}$, and $3.5\,\text{m s}^{-2}$ in the xy-plane. Further increasing the accelerations is restricted by the limit on the motor current, which is presently set to $1\,\text{A}$ (resulting in maximum torque of $5.57\,\text{N m}$).

The control framework developed for the task utilizes hybrid position/force control, where position control is achieved through an impedance controller consisting of a virtual spring-damper attached to the peg tip, with static forces continuously compensated using the inverse dynamics model presented in [26]. Based on the effective mass experienced on the tip, the stiffness and damping matrices are calculated so that the system behaves approximately like a mass-spring-damper with a pre-defined natural frequency. The stiffness of the system is increased to limit steady-state errors resulting from dynamic motion. This results in an eigenfrequency of the virtual system of 9 Hz for the stiff configuration.

As a result of the non-collocated tip-feedback, the critical parasitic frequency is excited. To suppress the resulting oscillations, a notch filter is implemented. The notch frequency is placed on the average frequency of the first parasitic eigenfrequency throughout the task space, at $61.3\,\text{Hz}$.

During testing, it was observed that the attainable accuracy of the system is sensitive to the parameter set for the inverse dynamic model. With a well-trained parameter set, the controller achieves an accuracy of $45\,\mu\text{m}$ in the plane of the hole. This accuracy is lower than the $32\,\mu\text{m}$ obtained during preliminary testing, likely due to the increased mass of the end-effector caused by the addition of the peg. An additional force of $\approx 1\,\text{N}$ would be required to mitigate the steady-state tracking error.

Re-insertion testing was performed at eight positions, with the peg successfully re-entering the hole without contact at three of the tested positions. In the remaining five positions, the peg made slight contact with the hole during re-insertion.

In conclusion, this thesis presents the development of a peg-in-hole task designed to showcase the key features of the T-Flex system. The developed demonstration displays the system's reproducibility, shown by re-inserting the peg in the hole, and its force sensitivity, which allows for precise control of the peg's insertion dynamics. The dancing motion illustrates the T-Flex's accelerations through the translational workspace.

6 Recommendations

A smaller clearance between the peg and the hole, combined with re-insertion without contact, makes for a more impressive demonstration of the T-Flex's reproducibility. The required clearance between the peg and the hole is determined by the system's tracking error. In this work, the tracking error is reduced by increasing the controller stiffness. The stiffness of the controller is currently limited by critical parasitic oscillations, which cause instability when the stiffness is increased further. Presently, the notch filter that suppresses the parasitic oscillations is placed at a constant frequency, while it is known that the first parasitic frequency is position-dependent. Therefore, the oscillations could be suppressed more effectively by making the notch filter position-dependent. The first parasitic frequency could be mapped for the task space, and the notch filter can be dynamically changed accordingly, allowing increased controller stiffness.

However, using a notch filter to suppress parasitic oscillations is a form of symptom treatment. Instead of suppressing the oscillations, active damping could be used in the form of collocated rate feedback [27, Chapter 7.2.1]. In collocated rate feedback, an additional torque is generated opposing the angular rate of the actuators. In [27, Chapter 7.2.1] it is established that a closed-loop bandwidth of approximately 0.25 times the parasitic frequency of interest can be obtained. The parasitic frequencies are approximately 60 Hz, so in theory a closed-loop bandwidth of 15 Hz should be obtainable.

Furthermore, the control currently implemented is relatively sensitive to errors in the model parameters. If the low-clearance peg is installed, not levelling the car properly or moving the peg potentially requires re-training of the parameters. The peg is typically inserted in the hole, but touching the hole while inserting makes the demonstration less appealing. One solution is to install the peg tip with the larger clearance or to re-train the parameters on the spot. Another option is to investigate if better accuracy can be obtained with a different controller. For the reaching, searching, inserting and measuring the current impedance controller can still be used. For the dancing motion the stiff controller is also sufficient.

For re-insertion, an integrator could be added to the PD action of the controller. The integral action will reduce the tracking error, making the controller less sensitive to variations in the model parameter set. An anti-windup scheme can be used to prevent unbounded growth of the integral in case the peg does touch the hole. As demonstrated in this work, an additional force of approximately 1 N would suffice to eliminate the steady-state tracking error.

While further increasing the accelerations would enhance wow-factor of the demonstration, it was observed during testing that the magnetic couplings in the elbow joints begin to decouple under certain trajectories. Therefore, careful consideration should be given to the design of these trajectories to ensure that the system can handle the increased accelerations. To further increase the accelerations, the limits on the motor currents must be increased as well.

In the current demosntration, only a part of the translational workspace of the T-Flex is showcased. For completeness, a trajectory displaying a part of the rotational workspace of the T-Flex can be included.

References

[1] M. Naves, M. Nijenhuis, B. Seinhorst, W. B. Hakvoort, and D. M. Brouwer, "T-Flex: A fully flexure-based large range of motion precision hexapod," *Precision Engineering*, vol. 72, pp. 912–928, 11 2021.

[2] J. J. De Jong, "Robotic Mechanisms, slides 11-12," in *DPPM2 Lectures*, 2023.

[3] Dutch Society for Precision Engineering, "Design using flexures," https://www.dspe.nl/knowledge/dppm-cases/design-using-flexures/, 2024, accessed: August 26, 2024.

[4] M. Naves, M. Nijenhuis, W. B. Hakvoort, and D. M. Brouwer, "Flexure-based 60 degrees stroke actuator suspension for a high torque iron core motor," *Precision Engineering*, vol. 63, pp. 105–114, 5 2020.

[5] M. Naves, R. G. Aarts, and D. M. Brouwer, "Large stroke high off-axis stiffness three degree of freedom spherical flexure joint," *Precision Engineering*, vol. 56, pp. 422–431, 3 2019.

[6] M. D. Plettenburg, "Kinematic and Workspace Analysis of a Flexure Based 6RSS Parallel Maniulator," *Master's Thesis - University of Twente, Faculty of Engineering Technology*, 2019.

[7] S. J. van der Werff, "Towards a Ball Bouncing Demonstration for the T-Flex," *Master's Thesis - University of Twente, Faculty of Engineering Technology*, 2023.

[8] I. J. O'Sullivan, "Progressing a ball bouncing demonstration for the T-Flex," *Capstone Project Report - University of Twente, University College ATLAS*, 2023.

[9] A. A. Lopes and F. Almeida, "A force-impedance controlled industrial robot using an active robotic auxiliary device," *Robotics and Computer-Integrated Manufacturing*, vol. 24, pp. 299–309, 2008. [Online]. Available: www.elsevier.com/locate/rcim

[10] S. R. Chhatpar and M. S. Branicky, "Search strategies for peg-in-hole assemblies with position uncertainty," in *Proceedings 2001 IEEE/RSJ International Conference on Intelligent Robots and Systems. Expanding the Societal Role of Robotics in the the Next Millennium (Cat. No.01CH37180)*, vol. 3, 2001, pp. 1465–1470.

[11] F. Chen, F. Cannella, J. Huang, H. Sasaki, and T. Fukuda, "A Study on Error Recovery Search Strategies of Electronic Connector Mating for Robotic Fault-Tolerant Assembly," *Journal of Intelligent and Robotic Systems: Theory and Applications*, vol. 81, no. 2, pp. 257–271, feb 2016. [Online]. Available: https://link.springer.com/article/10.1007/s10846-015-0248-5

[12] Y. Jiang, Z. Huang, B. Yang, and W. Yang, "A review of robotic assembly strategies for the full operation procedure: planning, execution and evaluation," *Robotics and Computer-Integrated Manufacturing*, vol. 78, p. 102366, 12 2022.

[13] H. Park, J. Park, D. H. Lee, J. H. Park, M. H. Baeg, and J. H. Bae, "Compliance-Based Robotic Peg-in-Hole Assembly Strategy Without Force Feedback," *IEEE Transactions on Industrial Electronics*, vol. 64, no. 8, pp. 6299–6309, 2017. [Online]. Available: http://ieeexplore.ieee.org.

[14] J. A. Marvel, R. Bostelman, and J. Falco, "Multi-Robot Assembly Strategies and Metrics," *ACM Comput. Surv*, vol. 51, no. 14, 2018. [Online]. Available: https://doi.org/10.1145/3150225

[15] S. Wang, G. Chen, H. Xu, and Z. Wang, "A Robotic Peg-in-Hole Assembly Strategy Based on Variable Compliance Center," *IEEE Access*, vol. 7, pp. 167 534–167 546, 2019.

[16] M. A. Habib, M. S. Alam, and N. H. Siddique, "Optimizing Coverage Performance of Multiple Random Path-planning Robots," *Paladyn*, vol. 3, no. 1, pp. 11–22, 3 2012. [Online]. Available: https://www.degruyter.com/document/doi/10.2478/s13230-012-0012-5/html

[17] H. Qiao, M. Wang, J. Su, S. Jia, and R. Li, "The concept of "attractive region in environment" and its application in high-precision tasks with low-precision systems," *IEEE/ASME Transactions on Mechatronics*, vol. 20, no. 5, pp. 2311–2327, 2015.

[18] F. Shen, Z. Zhang, D. Xu, J. Zhang, and W. Wu, "An Automatic Assembly Control Method for Peg and Hole Based on Multidimensional Micro Forces and Torques," *International Journal of Precision Engineering and Manufacturing*, vol. 20, pp. 1333–1346, 2019. [Online]. Available: https://doi.org/10.1007/s12541-019-00131-y

[19] M. W. Abdullah, H. Roth, M. Weyrich, and J. Wahrburg, "An approach for peg-in-hole assembling using intuitive search algorithm based on human behavior and carried by sensors guided industrial robot," *IFAC-PapersOnLine*, vol. 48, no. 3, pp. 1476–1481, 2015, 15th IFAC Symposium on Information Control Problems inManufacturing. [Online]. Available: https://www.sciencedirect.com/science/article/pii/S2405896315005340

[20] F. Dietrich, D. Buchholz, F. Wobbe, F. Sowinski, A. Raatz, W. Schumacher, and F. M. Wahl, "On contact models for assembly tasks: Experimental investigation beyond the peg-in-hole problem on the example of force-torque maps," *IEEE/RSJ 2010 International Conference on Intelligent Robots and Systems, IROS 2010 - Conference Proceedings*, pp. 2313–2318, 2010.

[21] M. P. Polverini, A. M. Zanchettin, S. Castello, and P. Rocco, "Sensorless and constraint based peg-in-hole task execution with a dual-arm robot," *Proceedings - IEEE International Conference on Robotics and Automation*, vol. 2016-June, pp. 415–420, 6 2016.

[22] H. Park, J. Park, D.-H. Lee, J.-H. Park, and J.-H. Bae, "Compliant Peg-in-Hole Assembly Using Partial Spiral Force Trajectory With Tilted Peg Posture," *IEEE ROBOTICS AND AUTOMATION LETTERS*, vol. 5, no. 3, p. 4447, 2020. [Online]. Available: https://www.ieee.org/publications/rights/index.html

[23] "Lecture Notes — Introduction to Robotics Chapter 9 — Mechanical Engineering — MIT OpenCourseWare," accessed: oktober 3, 2024. [Online]. Available: https://ocw.mit.edu/courses/2-12-introduction-to-robotics-fall-2005/pages/lecture-notes/

[24] J. J. De Jong, "Hysteresis and Microslip, slide 30," in *DPPM2 Lectures*, 2023.

[25] O. Khatib and J. Burdick, "Motion and force control of robot manipulators," in *Proceedings. 1986 IEEE International Conference on Robotics and Automation*, vol. 3, 1986, pp. 1381–1386.

[26] B. Seinhorst, " Implementation of Adaptive Feedforward Control for a 6DOF Manipulator," *Master's Thesis - University of Twente, Faculty of Engineering Technology*, 2020.

[27] J. B. Jonker, R. G. K. M. Aarts, and J. P. Meijaard, "Flexible Multibody Dynamics For Design Purposes," *FMBD course reader*, November 2022.

[28] NASA Technical Reports Server, "Quaternion averaging," https://ntrs.nasa.gov/api/citations/20070017872/downloads/20070017872.pdf, 2024, accessed: August 28, 2024.

[29] J. Angeles, "Trajectory Planning: Pick-and-Place Operations," in *Fundamentals of Robotic Mechanical Systems: Theory, Methods, and Algorithms*. Cham: Springer International Publishing, 2014, pp. 255–279. [Online]. Available: https://doi.org/10.1007/978-3-319-01851-5_6

[30] H. Köroğlu, "Bode Stability Criterion and Loop-Shaping, slide 58," in *Control Systems Design for Robotics Lectures*, 2022.

[31] H. K. Hemmes, S. G. Lemay, J. W. J. Verschuur, H. Wormeester, and H. J. Zwart, "Modelling, Analysis and Control of Dynamic Systems," *Lecture Notes v3.9*, October 16 2019, chapter 28.2.4, page 329.

[32] J. Schilder and B. de Gooier, "Mechanical Vibrations," *Lecture Notes Dynamics 2*, April 15 2019.

[33] M. T. Chu and G. H. Golub, "Structured inverse eigenvalue problems," *Acta Numerica*, vol. 11, pp. 1 – 71, 2002. [Online]. Available: https://api.semanticscholar.org/CorpusID:14743977

[34] A. Keemink, "Passivity, slide 12," in *CSDR Lecture 10*, 2022.

[35] Dr. I. S. M. Khalil, "Operational Space Control," *Control System Design for Robotics*, Januray 2023, lecture 13.2.

[36] Wikipedia, "Kruisproduct," https://nl.wikipedia.org/wiki/Kruisproduct#/media/Bestand:Cross_product_vector.svg, 2024, accessed: September 21, 2024.

Appendix A - Statement Regarding Use of AI Tools

- During the preparation of this work the author used OpenAI's GPT-3.5 generative AI language model in order to restructure and enhance readibility of the content created by the author. After using this tool, the author reviewed and edited the content as needed and takes full responsibility for the content of the work.
- During the preparation of this work the author used Grammarly's free writing assistant to perform spelling checks. After using this tool, the author reviewed and edited the content as needed and takes full responsibility for the content of the work.

Appendix B - Passivity of Implemented Control

By proving the passivity of the system, stability can be guaranteed when it interacts with another passive system [34]. In the case of this peg-in-hole task, the metal cylinder that contains the hole is passive since it a passive mechanical system. Therefore, stability during the peg-in-hole task can be guaranteed by proving that the control of the T-Flex yields a passive system.

Properties of equation of motion in robotics in joint and operation space:

To prove the passivity of the controlled system, a property of the standard equation in robotics can be used. The standard equation in robotics is given by:

$$M(\boldsymbol{q})\ddot{\boldsymbol{q}} + C(\boldsymbol{q}, \dot{\boldsymbol{q}})\dot{\boldsymbol{q}} + N(\boldsymbol{q}) = \boldsymbol{\tau} \tag{B.1}$$

where $\boldsymbol{q}$ is the vector of joint coordinates, $M(\boldsymbol{q})$ is the inertia tensor, $C(\boldsymbol{q}, \dot{\boldsymbol{q}})\dot{\boldsymbol{q}}$ is the vector containing Coriolis and centrifugal forces, and $N(\boldsymbol{q})$ contains the remaining forces such as gravity and other forces acting on the system and $\boldsymbol{\tau}$ represents the joint torques.

The matrices in this equation possess the following property:

$$(\dot{M} - 2C)^T = -(\dot{M} - 2C) \qquad \Rightarrow \qquad \boldsymbol{q}^T(\dot{M} - 2C)\boldsymbol{q} = 0 \tag{B.2}$$

In other words, $(\dot{M} - 2C)$ is skew-symmetric, and pre- and post-multiplication with a vector and its transpose will result in a scalar value of zero.

If the Jacobian matrix mapping from actuator space to end-effector space is nonsingular, as is the case with the T-Flex, the dynamics of the system can uniquely be represented in the operational space. It is important to note that this assumes the T-Flex behaves as a rigid body system with stiffness in the joints, meaning it does not exhibit degrees of freedom due to the finite stiffness of the links and the finite support stiffness of the joints.

By introducing the following Jacobian matrix $J(\boldsymbol{q})$:

$$\dot{\boldsymbol{p}} = J(\boldsymbol{q})\dot{\boldsymbol{q}} \qquad , \qquad \boldsymbol{\tau} = J(\boldsymbol{q})^T \boldsymbol{F}_{ee} \tag{B.3}$$

which maps joint velocity to operational space velocity of the end-effector $\dot{\boldsymbol{p}}$, the equation of motion in the operational space can be derived from the equation of motion in the joint space. The resulting equation of motion in the operational space is given by [35]:

$$J^{-T}MJ^{-1}\ddot{\boldsymbol{p}} + (J^{-T}CJ^{-1} - J^{-T}MJ^{-1}\dot{J}J^{-1})\dot{\boldsymbol{p}} + J^{-T}N = \boldsymbol{F}_{ee} \tag{B.4}$$

To improve readability, the equation can be displayed as:

$$\tilde{M}(\boldsymbol{q})\ddot{\boldsymbol{p}} + \tilde{C}(\boldsymbol{q}, \dot{\boldsymbol{q}})\dot{\boldsymbol{p}} + \tilde{N}(\boldsymbol{q}, \dot{\boldsymbol{q}}) = \boldsymbol{F}_{ee} \tag{B.5}$$

Equation (B.5) shares the property of equation (B.1), namely that:

$$(\dot{\tilde{M}} - 2\tilde{C})^T = -(\dot{\tilde{M}} - 2\tilde{C}) \qquad \Rightarrow \qquad \boldsymbol{p}^T(\dot{\tilde{M}} - 2\tilde{C})\boldsymbol{p} = 0 \tag{B.6}$$

T-Flex equations of motion and control in operational space:

The implemented control is in the operational space of the T-Flex. Therefore, a first step in proving passivity of the system is expressing the equations of motion in the operational space. To do so, three analytical Jacobian matrices are used:

$$\begin{aligned} &\dot{\boldsymbol{x}} = J_{xa}(\boldsymbol{x})\dot{\boldsymbol{\theta}} \\ &\boldsymbol{\tau} = J_{xa}(\boldsymbol{x})^T \boldsymbol{F} \\ &J_{xa} \in \mathbb{R}^{37\times 6} \end{aligned} \tag{B.7}$$

$$\begin{aligned} &\dot{\boldsymbol{p}} = J_{ea}(\boldsymbol{x})\dot{\boldsymbol{\theta}} \\ &\boldsymbol{\tau} = J_{ea}(\boldsymbol{x})^T \boldsymbol{F}_{ee} \\ &J_{ea} \in \mathbb{R}^{6\times 6} \end{aligned} \tag{B.8}$$

$$\begin{aligned} &\dot{\boldsymbol{x}} = J_{xe}(\boldsymbol{x})\dot{\boldsymbol{p}} \\ &\boldsymbol{F}_{ee} = J_{xe}(\boldsymbol{x})^T \boldsymbol{F} \\ &J_{xe} \in \mathbb{R}^{37\times 6} \end{aligned} \tag{B.9}$$

$$J_{xa}(\boldsymbol{x}) = J_{xe}(\boldsymbol{x})J_{ea}(\boldsymbol{x}) \tag{B.10}$$

where:

- The Jacobian matrix J_{xa} maps the actuator joint velocities $\dot{\boldsymbol{\theta}}$ (dual to the acutator torques $\boldsymbol{\tau}$) to the velocities of the generalized coordinates $\dot{\boldsymbol{x}}$ (dual to the generalized forces $\boldsymbol{F}$).
- The Jacobian matrix J_{ea} maps $\dot{\boldsymbol{\theta}}$ to the end-effector's linear and angular velocities $\dot{\boldsymbol{p}}$, which are dual to the wrench applied at the end-effector.
- $\boldsymbol{F}_{ee}$ is the equivalent wrench applied at the end-effector resulting from the actuator torques $\boldsymbol{\tau}$
- The Jacobian matrix J_{xe} maps $\dot{\boldsymbol{p}}$ to $\dot{\boldsymbol{x}}$

The dynamics of the T-Flex in the actuator space are given by [26]:

$$J_{xa}(\boldsymbol{x})^T\Big(M(\boldsymbol{x})\ddot{\boldsymbol{x}} + \boldsymbol{h}(\boldsymbol{x},\dot{\boldsymbol{x}}) - \boldsymbol{f}(\boldsymbol{x}) - \boldsymbol{g}(\boldsymbol{x})\Big) - \boldsymbol{\chi} = \boldsymbol{\tau} + \boldsymbol{\tau}_{ext} \tag{B.11}$$

where $M(\boldsymbol{x})$ is the inertia matrix, $\boldsymbol{h}(\boldsymbol{x},\dot{\boldsymbol{x}})$ is a vector containing Coriolis and centrifugal forces, $\boldsymbol{f}(\boldsymbol{x})$ is the gravity vector, $\boldsymbol{g}(\boldsymbol{x})$ are the elastic joint reaction forces, $\boldsymbol{\chi}$ are the cogging forces and $\boldsymbol{\tau}_{ext}$ are the torques experienced by the actuator due to the externally applied forces. The forces resulting from hysteresis in the actuators are omitted, as hysteresis acts as a passive system on its own.

Equation (B.11) can be represented shorter as:

$$\begin{aligned} J_{xa}^T\Big(M\ddot{\boldsymbol{x}} + \boldsymbol{h} - \boldsymbol{f} - \boldsymbol{g}\Big) - \boldsymbol{\chi} &= \boldsymbol{\tau} + \boldsymbol{\tau}_{ext} \\ J_{ea}^T J_{xe}^T\Big(M\ddot{\boldsymbol{x}} + \boldsymbol{h} - \boldsymbol{f} - \boldsymbol{g}\Big) - \boldsymbol{\chi} &= \boldsymbol{\tau} + \boldsymbol{\tau}_{ext} \end{aligned} \tag{B.12}$$

The dynamics can be expressed in the operational space as follows:

$$\begin{aligned} J_{xe}^T\Big(M\ddot{\boldsymbol{x}} + \boldsymbol{h} - \boldsymbol{f} - \boldsymbol{g}\Big) - J_{ea}^{-T}\boldsymbol{\chi} &= J_{ea}^{-T}\boldsymbol{\tau} + J_{ea}^{-T}\boldsymbol{\tau}_{ext} \\ J_{xe}^T\Big(M\Big(J_{xe}\ddot{\boldsymbol{p}} + \dot{J}_{xe}\dot{\boldsymbol{p}}\Big) + \boldsymbol{h} - \boldsymbol{f} - \boldsymbol{g}\Big) - J_{ea}^{-T}\boldsymbol{\chi} &= \boldsymbol{F}_{ee} + J_{ea}^{-T}\boldsymbol{\tau}_{ext} \end{aligned} \tag{B.13}$$

The equation of motion of the T-Flex in operational space (equation (B.13)) can now be compared to the standard equations of robotics in operational space (equation (B.5)) to find which tensors are equivalent. The following is found:

$$\tilde{M}(\boldsymbol{q}) \equiv J_{xe}^T M J_{xe} \tag{B.14}$$

$$\tilde{C}(\boldsymbol{q},\dot{\boldsymbol{q}})\dot{\boldsymbol{p}} \equiv J_{xe}^T M \dot{J}_{xe}\dot{\boldsymbol{p}} + J_{xe}^T\boldsymbol{h} \tag{B.15}$$

Proof of passivity

For the analysis, the control implemented on the T-Flex can be represented as:

$$\boldsymbol{F}_{ee} = J_{xe}^T M J_{xe}\begin{bmatrix}\ddot{\boldsymbol{p}}_d \\ \ddot{\boldsymbol{q}}_{\boldsymbol{d}}\end{bmatrix} + D\begin{bmatrix}(\dot{\boldsymbol{p}}_d - \dot{\boldsymbol{p}}) \\ (\boldsymbol{\omega_d} - \boldsymbol{\omega})\end{bmatrix} + K\begin{bmatrix}(\boldsymbol{p}_d - \boldsymbol{p}) \\ \frac{1}{2}\boldsymbol{E_r}\end{bmatrix} + J_{xe}^T(-\boldsymbol{f} - \boldsymbol{g}) - J_{ea}^{-T}\boldsymbol{\chi} \tag{B.16}$$

The error vector $\boldsymbol{E_r}$, used to calculate the virtual spring moments of the controller, is nonlinear. However, $\boldsymbol{E_r}$ is continuous and shows a positive rotation-moment relationship. Therefore, the rotational part of the control is not expected to have different passivity characteristics than the translational part of the control. To simplify the notation, only the linear forces will be considered for the analysis:

$$\begin{aligned} \boldsymbol{F}_{ee} &= J_{xe}^T M J_{xe}\ddot{\boldsymbol{p}}_d + D(\dot{\boldsymbol{p}}_d - \dot{\boldsymbol{p}}) + K(\boldsymbol{p_d} - \boldsymbol{p}) + J_{xe}^T(-\boldsymbol{f} - \boldsymbol{g}) - J_{ea}^{-T}\boldsymbol{\chi} \\ \boldsymbol{F}_{ee} &= J_{xe}^T M J_{xe}\ddot{\boldsymbol{p}}_d + D\dot{\boldsymbol{e}} + K\boldsymbol{e} + J_{xe}^T(-\boldsymbol{f} - \boldsymbol{g}) - J_{ea}^{-T}\boldsymbol{\chi} \end{aligned} \tag{B.17}$$

The energy storage function of the system can be presented as the sum of the kinetic energy in the manipulator and the potential energy in the controller:

$$\begin{aligned} V(\boldsymbol{x},\boldsymbol{p},\dot{\boldsymbol{p}}) &= \frac{1}{2}\dot{\boldsymbol{p}}^T\left(J_{xe}^T(\boldsymbol{x})M(\boldsymbol{x})J_{xe}(\boldsymbol{x})\right)\dot{\boldsymbol{p}} + \frac{1}{2}\boldsymbol{e}^T K\boldsymbol{e} \\ V &= \frac{1}{2}\dot{\boldsymbol{p}}^T(J_{xe}^T M J_{xe})\dot{\boldsymbol{p}} + \frac{1}{2}\boldsymbol{e}^T K\boldsymbol{e} \end{aligned} \tag{B.18}$$

In this equation, the potential gravitational ($\boldsymbol{f}$), joint reaction ($\boldsymbol{g}$) and cogging ($\boldsymbol{\chi}$) energy are left out because they are continuously compensated by the controller.

The time derivative of the energy storage function is given by:

$$\dot{V} = \frac{1}{2}\dot{\boldsymbol{p}}^T\Big(\frac{d}{dt}(J_{xe}^T M J_{xe})\Big)\dot{\boldsymbol{p}} + \dot{\boldsymbol{p}}^T(J_{xe}^T M J_{xe})\ddot{\boldsymbol{p}} + \boldsymbol{e}^T K\dot{\boldsymbol{e}} \tag{B.19}$$

By rewriting the equation of motion (B.13), and filling in the control action of equation (B.17) the following expression can be found:

$$\begin{aligned}
J_{xe}^T M J_{xe}\ddot{\boldsymbol{p}} =& J_{xe}^T\Big(-M\dot{J}_{xe}\dot{\boldsymbol{p}} - \boldsymbol{h} + \boldsymbol{f} + \boldsymbol{g}\Big) + J_{ea}^{-T}\boldsymbol{\chi} + \boldsymbol{F}_{ee} + J_{ea}^{-T}\boldsymbol{\tau}_{ext} \\
J_{xe}^T M J_{xe}\ddot{\boldsymbol{p}} =& J_{xe}^T\Big(-M\dot{J}_{xe}\dot{\boldsymbol{p}} - \boldsymbol{h} + \boldsymbol{f} + \boldsymbol{g}\Big) + J_{ea}^{-T}\boldsymbol{\chi} + \\
& \qquad (J_{xe}^T M J_{xe}\ddot{\boldsymbol{p}}_d + D\dot{\boldsymbol{e}} + K\boldsymbol{e} + J_{xe}^T(-\boldsymbol{f} - \boldsymbol{g}) - J_{ea}^{-T}\boldsymbol{\chi}) + J_{ea}^{-T}\boldsymbol{\tau}_{ext} \\
J_{xe}^T M J_{xe}\ddot{\boldsymbol{p}} =& -J_{xe}^T M\dot{J}_{xe}\dot{\boldsymbol{p}} - J_{xe}^T\boldsymbol{h} + J_{xe}^T M J_{xe}\ddot{\boldsymbol{p}}_d + D\dot{\boldsymbol{e}} + K\boldsymbol{e} + J_{ea}^{-T}\boldsymbol{\tau}_{ext}
\end{aligned} \tag{B.20}$$

The result of this substitution can be substituted into equation (B.19) to obtain the following:

$$\dot{V} = \frac{1}{2}\dot{\boldsymbol{p}}^T\Big(\frac{d}{dt}(J_{xe}^T M J_{xe})\Big)\dot{\boldsymbol{p}} - \dot{\boldsymbol{p}}^T(J_{xe}^T\dot{J}_{xe}\dot{\boldsymbol{p}} + J_{xe}^T\boldsymbol{h}) + \dot{\boldsymbol{p}}^T\Big(J_{xe}^T M J_{xe}\ddot{\boldsymbol{p}}_d + D\dot{\boldsymbol{e}} + K\boldsymbol{e} + J_{ea}^{-T}\boldsymbol{\tau}_{ext}\Big) + \boldsymbol{e}^T K\dot{\boldsymbol{e}} \tag{B.21}$$

By combining equations (B.6), (B.14) and (B.15) the following can be concluded about the sum of the first two components of equation (B.21):

$$\frac{1}{2}\dot{\boldsymbol{p}}^T\Big(\frac{d}{dt}(J_{xe}^T M J_{xe})\Big)\dot{\boldsymbol{p}} - \dot{\boldsymbol{p}}^T(J_{xe}^T M\dot{J}_{xe}\dot{\boldsymbol{p}} + J_{xe}^T\boldsymbol{h}) \equiv \dot{\boldsymbol{p}}^T\Big(\dot{\tilde{M}} - 2\tilde{C}\Big)\dot{\boldsymbol{p}} = 0 \tag{B.22}$$

With this result, equation (B.21) can be simplified to:

$$\begin{aligned}
\dot{V} &= \dot{\boldsymbol{p}}^T\Big(J_{xe}^T M J_{xe}\ddot{\boldsymbol{p}}_d + D\dot{\boldsymbol{e}} + K\boldsymbol{e} + J_{ea}^{-T}\boldsymbol{\tau}_{ext}\Big) + \boldsymbol{e}^T K\dot{\boldsymbol{e}} \\
\dot{V} &= \dot{\boldsymbol{p}}^T\Big(J_{xe}^T M J_{xe}\ddot{\boldsymbol{p}}_d + D(\dot{\boldsymbol{p}}_{\boldsymbol{d}} - \dot{\boldsymbol{p}}) + K(\boldsymbol{p}_{\boldsymbol{d}} - \boldsymbol{p}) + J_{ea}^{-T}\boldsymbol{\tau}_{ext}\Big) + (\boldsymbol{p}_{\boldsymbol{d}} - \boldsymbol{p})^T K(\dot{\boldsymbol{p}}_{\boldsymbol{d}} - \dot{\boldsymbol{p}})
\end{aligned} \tag{B.23}$$

In case the reference is stationary: $\dot{\boldsymbol{p}}_d = 0$, equation (B.23) simplifies to:

$$\begin{aligned}
\dot{V} &= \dot{\boldsymbol{p}}^T\Big(-D\dot{\boldsymbol{p}} - K\boldsymbol{p} + J_{ea}^{-T}\boldsymbol{\tau}_{ext}\Big) + \boldsymbol{p}^T K\dot{\boldsymbol{p}} \\
\dot{V} &= -\dot{\boldsymbol{p}}^T D\dot{\boldsymbol{p}} + \dot{\boldsymbol{p}}^T J_{ea}^{-T}\boldsymbol{\tau}_{ext} \quad \leq \quad \dot{\boldsymbol{p}}^T J_{ea}^{-T}\boldsymbol{\tau}_{ext}
\end{aligned} \tag{B.24}$$

Since D is positive definite, the first term in equation (B.24) is negative definite. Consequently, the power flow into the system's power storage is smaller than the power provided to the system ($\dot{\boldsymbol{p}}^T J_{ea}^{-T}\boldsymbol{\tau}_{ext}$), and the system is thus passive during regulation.

Furthermore, it can be concluded that for a non-stationary reference temporary energy storage may occur. Practice has shown that this does not lead to problems when the peg interacts with the hole because the power input is finite due to finite time of the non-stationary references. This is in line with the expectation because the system is designed to imitate a damped mass-sping-damper. Because the reference signal is always $\mathcal{C}^2$ (twice differentiable) and stationary after a finite time, no excessive energy is generated by changes in $\boldsymbol{p}_{\boldsymbol{d}}$ and the energy generated in the system is limited.

Appendix C - Geometric Inconsistency of Rotational Error Vector $\boldsymbol{E_r}$

The error vector specifying the angular misalignment between two frames $\boldsymbol{\Psi_A}$ and $\boldsymbol{\Psi_B}$ is specified as:

$$\boldsymbol{E}_r(\boldsymbol{R_A}, \boldsymbol{R_B}) = [\boldsymbol{R}_{A(:,1)} \times \boldsymbol{R}_{B(:,1)} + \boldsymbol{R}_{A(:,2)} \times \boldsymbol{R}_{B(:,2)} + \boldsymbol{R}_{A(:,3)} \times \boldsymbol{R}_{B(:,3)}] \tag{C.1}$$

where $\boldsymbol{R}_{A(:,1)}$ specifies the first column of $\boldsymbol{R_A}$, and so on. $\boldsymbol{R_A}$ is the rotation matrix that specifies the orientation of frame $\boldsymbol{\Psi_A}$ in the global reference frame. Therefore, $\boldsymbol{R}_{A(:,1)}$ specifies the basis vector $\mathbf{e}_{\boldsymbol{x}}$ of $\boldsymbol{\Psi_A}$ ($\mathbf{e}_{\boldsymbol{x},\boldsymbol{A}}$) in $\boldsymbol{\Psi_G}$, etc.

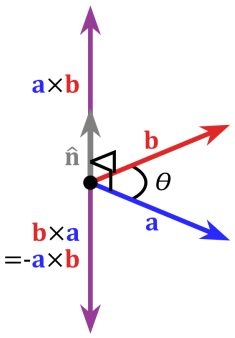

Figure C.1: Visualization of cross product [36].

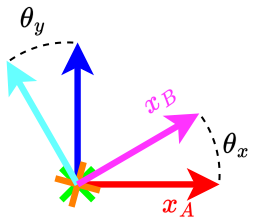

Figure C.2: Rotation of two frames relative to each other with z-axes aligned.

The cross product of two vectors $\boldsymbol{a}$ and $\boldsymbol{b}$ is specified as:

$$\boldsymbol{a} \times \boldsymbol{b} = \|\boldsymbol{a}\|\|\boldsymbol{b}\| \sin(\theta)\hat{\boldsymbol{n}} \tag{C.2}$$

where $\hat{\boldsymbol{n}}$ is the unit vector perpendicular to the plane defined by $\boldsymbol{a}$ and $\boldsymbol{b}$ (see Fig. C.1), and θ is the angle between $\boldsymbol{a}$ and $\boldsymbol{b}$.

Every column in a rotation matrix is a vector with unit length. As a result, every cross product in $\boldsymbol{E_r}$ boils down to:

$$\boldsymbol{R}_{A(:,i)} \times \boldsymbol{R}_{B(:,i)} = \sin(\theta)\hat{\boldsymbol{n}} \tag{C.3}$$

Due to this definition of $\boldsymbol{E_r}$, the norm of the error vector does not scale linearly with angle of the relative rotation θ. To illustrate this, Fig. C.2 can be inspected: $\boldsymbol{\Psi_A}$ and $\boldsymbol{\Psi_B}$ are rotated with an angle $\varphi = \theta_x = \theta_y$, resulting in $\|\boldsymbol{E_r}\| = 2\sin(\|\varphi\|)$. This relation is displayed in Fig. C.3. In fact, the relation $\|\boldsymbol{E_r}\| = 2\sin(\|\varphi\|)$ holds for any arbitrary axis of rotation. As a result, small angles φ will lead to $\|\boldsymbol{E_r}\| \approx 2\varphi$. This must be considered when multiplying $\boldsymbol{E_r}$ with the stiffness matrix. Therefore, $\boldsymbol{E_r}$ is scaled with $\frac{1}{2}$ when calculating the spring moment on the peg in equation (44).

Because the angle of rotation of $\boldsymbol{\Psi_E}$ in $\boldsymbol{\Psi_G}$ will always be relatively small in the considered application (and the error in rotation even smaller), this geometric inconsistency and the corresponding nonlinearity is not considered an issue.

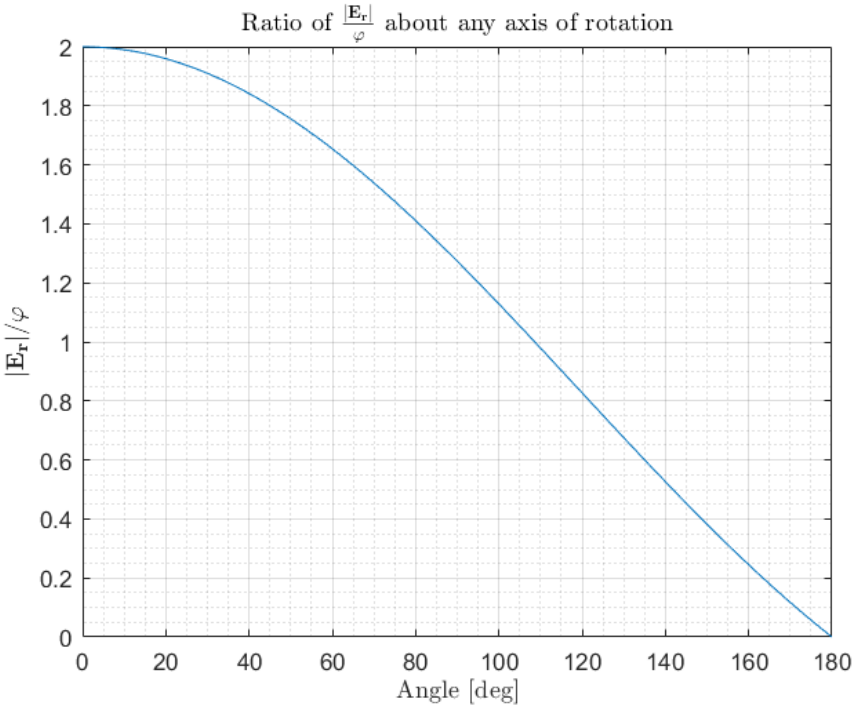

Figure C.3: Ratio of $\|\boldsymbol{E_r}\|/\varphi$.

Appendix D - Jacobian Conversion from Generalized to Translational and Angular End-Effector Velocities

The Jacobian matrix $J_{xe}(\boldsymbol{x}) \in \mathbb{R}^{37\times 6}$ maps the generalized end-effector velocities to the complete set of generalized velocities, and is defined by:

$$\dot{\boldsymbol{x}} = J_{xe}(\boldsymbol{x}) \begin{bmatrix} \dot{\boldsymbol{p}}_{\boldsymbol{E}} \\ \dot{\tilde{\boldsymbol{q}}}_{\boldsymbol{E}} \end{bmatrix} \tag{D.1}$$

where $\dot{\boldsymbol{p}}_{\boldsymbol{E}}$ is the cartesian velocity of the T-Flex's end-effector in the global frame $\boldsymbol{\Psi_G}$, and $\dot{\tilde{\boldsymbol{q}}}_{\boldsymbol{E}}$ is the time derivative of the vector part of the quaternion specifying the orientation of the end-effector in $\boldsymbol{\Psi_G}$.

The forces and moments due to the virtual spring and damper form a geometric wrench $\begin{bmatrix} \boldsymbol{f}_{\boldsymbol{c}}^T & \boldsymbol{m}_{\boldsymbol{c}}^T \end{bmatrix}^T$, as specified in equation (48) in section 2.3.2. The geometric wrench is dual to the cartesian and angular velocities of the end-effector $\begin{bmatrix} \dot{\boldsymbol{p}}_{\boldsymbol{E}}^T & \boldsymbol{\omega}_{\boldsymbol{E}}^T \end{bmatrix}^T$, and not to the generalized end-effector velocities in $\begin{bmatrix} \dot{\boldsymbol{p}}_{\boldsymbol{E}}^T & \dot{\tilde{\boldsymbol{q}}}_{\boldsymbol{E}}^T \end{bmatrix}^T$. Consequently, $J_{xe}(\boldsymbol{x})$ must be adapted to find the mapping between the geometric wrench and the generalized forces. This resulting Jacobian matrix will be denoted with $J_{ee,\omega}(\boldsymbol{x})$, and is specified by the following relation:

$$\dot{\boldsymbol{x}} = J_{ee,\omega}(\boldsymbol{x}) \begin{bmatrix} \dot{\boldsymbol{p}}_{\boldsymbol{E}} \\ \boldsymbol{\omega}_{\boldsymbol{E}} \end{bmatrix} \tag{D.2}$$

The angular rate can be transformed to the time derivative of a unit quaternion as follows [27, Chapter 4.1]:

$$\dot{\tilde{\boldsymbol{q}}} = \frac{1}{2} \left[q_0 \boldsymbol{I} - \tilde{\tilde{\boldsymbol{q}}} \right] \boldsymbol{\omega} \tag{D.3}$$

And thus equation (D.3) can be substituted into equation (D.1) to find:

$$\dot{\boldsymbol{x}} = J_{xe}(\boldsymbol{x}) \begin{bmatrix} \boldsymbol{I} & \boldsymbol{O} \\ \boldsymbol{O} & \frac{1}{2} \left[q_{E,0} \boldsymbol{I} - \tilde{\tilde{\boldsymbol{q}}}_{\boldsymbol{E}} \right] \end{bmatrix} \begin{bmatrix} \dot{\boldsymbol{p}}_{\boldsymbol{E}} \\ \boldsymbol{\omega}_{\boldsymbol{E}} \end{bmatrix} \tag{D.4}$$

Comparing this result to equation (D.2) the result is:

$$J_{xe,\omega}(\boldsymbol{x}) = J_{xe}(\boldsymbol{x}) \begin{bmatrix} \boldsymbol{I} & \boldsymbol{O} \\ \boldsymbol{O} & \frac{1}{2} \left[q_{E,0} \boldsymbol{I} - \tilde{\tilde{\boldsymbol{q}}}_{\boldsymbol{E}} \right] \end{bmatrix} \tag{D.5}$$

As discussed in Appendix E, J_{ea} is the inverse of a partition of J_{xe}. Consequently, $J_{ea,\omega}$ can be calculated as the inverse of the following partition of Jacobian $J_{xe,\omega}$:

$$J_{ea,\omega}(\boldsymbol{x}) = \left[J_{xe,\omega}(\boldsymbol{x})_{([1:6],:)} \right]^{-1} \tag{D.6}$$

where $J_{xe,\omega}(\boldsymbol{x})_{([1:6],:)}$ stands for rows 1 – 6 of Jacobian matrix $J_{xe,\omega}$.

Appendix E - Calculation of Jacobian Matrices J_{xe} and J_{ea}

Jacobian Matrix $J_{xe}(\boldsymbol{x})$

Jacobian matrix $J_{xe}(\boldsymbol{x}) \in \mathbb{R}^{37\times 6}$ maps generalized end-effector velocities to the complete set of generalized coordinates, and is defined by the equation:

$$\dot{\boldsymbol{x}} = J_{xe}(\boldsymbol{x}) \begin{bmatrix} \dot{\boldsymbol{p}}_{\boldsymbol{E}} \\ \dot{\bar{\boldsymbol{q}}}_{\boldsymbol{E}} \end{bmatrix} \tag{E.1}$$

For ease of notation, $\begin{bmatrix} \boldsymbol{p}_{\boldsymbol{E}}^T & \bar{\boldsymbol{q}}_{\boldsymbol{E}}^T \end{bmatrix}^T$ will be denoted as $\bar{\boldsymbol{E}}$ for the remainder of this appendix. The generalized end-effector coordinates are a subset of the total set of generalized coordinates, and thus $\bar{\boldsymbol{E}}$ is a subset of $\boldsymbol{x}$:

$$\bar{\boldsymbol{E}} = \begin{bmatrix} \boldsymbol{p}_{\boldsymbol{E}} \\ \bar{\boldsymbol{q}}_{\boldsymbol{E}} \end{bmatrix} = \boldsymbol{x}_{(31:33,35:37)} \tag{E.2}$$

The kinematic model of the T-Flex is developed for the 6-RUS configuration, which is exactly constrained. Therefore, the independent coordinates can be re-defined as $\bar{\boldsymbol{E}}$, and the dependent coordinates as $\boldsymbol{d} = \boldsymbol{x} \backslash \bar{\boldsymbol{E}}$; the set difference of $\boldsymbol{x}$ and $\bar{\boldsymbol{E}}$. Consequently, the implicit constraints of the kinematic model can be written as:

$$\mathcal{D}(\boldsymbol{x}) = \mathcal{D}(\bar{\boldsymbol{E}}, \boldsymbol{d}) = \boldsymbol{0} \tag{E.3}$$

Following equation (38), the rows of $J_{xe}(\boldsymbol{x})$ that correspond to $\boldsymbol{d}$ are given by:

$$J_{xe}(\boldsymbol{x})_{([1:30,34],:)} = -\left[\mathcal{D}_d(\boldsymbol{x})\right]^{-1} \mathcal{D}_{\bar{E}}(\boldsymbol{x}) \tag{E.4}$$

where $\mathcal{D}_d$ are the partial derivatives of $\mathcal{D}$ with respect to $\boldsymbol{d}$, and $\mathcal{D}_{\bar{E}}$ are the partial derivatives with respect $\bar{\boldsymbol{E}}$. The rows of $J_{xe}(\boldsymbol{x})$ corresponding to $\bar{\boldsymbol{E}}$ are just an identity matrix of 6-by-6:

$$J_{xe}(\boldsymbol{x})_{([31:33,35:37],:)} = \boldsymbol{I} \tag{E.5}$$

Jacobian Matrix $J_{ea}(\boldsymbol{x})$

Jacobian matrix $J_{ea}(\boldsymbol{x}) \in \mathbb{R}^{6\times 6}$ maps actuator velocities to generalized end-effector velocities, and is defined by the equation:

$$\begin{bmatrix} \dot{\boldsymbol{p}}_{\boldsymbol{E}} \\ \dot{\bar{\boldsymbol{q}}}_{\boldsymbol{E}} \end{bmatrix} = J_{ea}(\boldsymbol{x})\dot{\boldsymbol{\theta}} \tag{E.6}$$

Vector $\boldsymbol{\theta}$ is a subset of $\boldsymbol{x}$:

$$\boldsymbol{\theta} = \boldsymbol{x}_{(1:6)} \tag{E.7}$$

Consequently, $J_{xe}(\boldsymbol{x})$ of the section above can be partitioned as follows:

$$\dot{\boldsymbol{\theta}} = J_{xe}(\boldsymbol{x})_{([1:6],:)} \begin{bmatrix} \dot{\boldsymbol{p}}_{\boldsymbol{E}} \\ \dot{\bar{\boldsymbol{q}}}_{\boldsymbol{E}} \end{bmatrix} \tag{E.8}$$

Since $J_{xe}(\boldsymbol{x})_{([1:6],:)}$ is square and nonsingular in the task space, it can be inverted to find:

$$J_{ea}(\boldsymbol{x}) = \left[J_{xe}(\boldsymbol{x})_{([1:6],:)}\right]^{-1} \tag{E.9}$$

Appendix F - Plagiarism Report

turnitin

Similarity Report ID: oid:6294:237191368

15% Overall Similarity

Top sources found in the following databases:

- 9% Internet database
- Crossref database
- 2% Submitted Works database
- 12% Publications database
- Crossref Posted Content database

TOP SOURCES

The sources with the highest number of matches within the submission. Overlapping sources will not be displayed.

1	Hyeonjun Park, Jaeheung Park, Dong-Hyuk Lee, Jae-Han Park, Moon-H... Crossref	<1%
2	arxiv.org Internet	<1%
3	ris.utwente.nl Internet	<1%
4	export.arxiv.org Internet	<1%
5	mafiadoc.com Internet	<1%
6	hindawi.com Internet	<1%
7	"Humanoid Robotics: A Reference", Springer Science and Business Me... Crossref	<1%